ANISOTROPIC COPPER OXIDE NANORODS DECORATED WITH GOLD AND PALLADIUM NANOPARTICLES AND THEIR ENZYMATIC PROPERTIES

A thesis submitted for the fulfilment of the requirements for the degree of

MASTER OF SCIENCE

of

RHODES UNIVERSITY

by

SIMBONGILE SICWETSHA

ORCiD: 0000-0002-3703-9051

SEPTEMBER 2020

ACKNOWLEDGEMENTS

First of all, I am very grateful to God the Almighty for his grace and for giving me strength and energy to persevere throughout my MSc program.

I would like to express my sincere gratitude to my supervisor Dr Mashazi for recognizing potential in me and for accepting to mentor me from the first day I arrived at Rhodes University to do my internship. I am also very grateful for his supervision, guidance, motivation and continuous support throughout my academic journey at Rhodes University.

My sincere thanks goes to my parents (Mr Patrick Thembekile Sicwetsha and Mrs Bongiwe Nolusapho Sicwetsha) for their love, guidance, support, prayers and for preparing me for a better future. I would also like to extend my deepest gratitude to my siblings for their love, support and motivation. Enkosi ko Mpinga Mawawa Mbhala ka Nkqoshe Senzwa Sineka oNto'mntwana.

I am grateful to Henderson Scholarship and the National Research Foundation (NRF) for the financial support. I am also thankful to the Centre for Nanotechnology Innovation (CNI) and the Electron Microscope Unit for granting me access to utilize their equipment for my research work.

Last but not the least, I would like to acknowledge all the academic staff, support staff and my fellow colleagues in Lab F3 and F5. I am very grateful to Dr Omotayo Adeniyi for his advices, suggestions, and guidance. Thank you so much brother you have always been like my second supervisor.

ABSTRACT

The synthesis of spherical CuO nanoparticles (CuONPs), copper oxide nanorods (CuONRs), CuONRs decorated with gold (CuONRs@$Au_{1.0}$NPs), CuONRs decorated with palladium (CuONRs@$Pd_{1.0}$NPs) and CuONRs decorated with gold and palladium (CuONRs@$Au_{0.5}$/$Pd_{0.5}$NPs) was carried out. The successful preparation of these nanomaterials was confirmed using UV-vis, DLS (zeta potential), XRD, TEM and EDS. The nanoparticles were found to possess intrinsic peroxidase-like activity. The peroxidase-like activity of the nanoparticles was dependent on pH, temperature and enzyme substrate concentration.

The investigation of the steady-state kinetic parameters showed that the peroxidase-like activity of the nanomaterials followed the Michaelis-Menten kinetics behaviour. The spherical CuONPs showed the K_m = 1.12 mM and 1.14 mM for H_2O_2 and TMB respectively. The CuONRs showed the K_m = 40.04 mM and 2.91 mM for H_2O_2 and TMB respectively. The CuONRs@$Au_{1.0}$NPs showed the K_m = 3.05 mM and 6.49 mM for H_2O_2 and TMB respectively. The CuONRs@$Pd_{1.0}$NPs showed the K_m = 0.13 mM and 2.59 mM for H_2O_2 and TMB respectively. The CuONRs@$Au_{0.5}$/$Pd_{0.5}$NPs showed the K_m = 2.66 mM and K_m = 19.70 mM for H_2O_2 and TMB respectively.

The nanomaterials interact with hydrogen peroxide to produce hydroxyl radicals (OH·). Therefore, the production of reactive oxygen species (ROS) was investigated and detected using 1,3-diphenylisobenzofuran (DPBF) as a radical scavenger.

The prepared nanomaterials were used in biosensing for the colorimetric detection of glucose. The LOD and LOQ for spherical CuONPs was 0.73 µM and 2.42 µM, for CuONRs was 0.13 µM and 0.42 µM, CuONRs@$Au_{1.0}$NPs was 7.19 µM and 21.78 µM, for CuONRs@$Pd_{1.0}$ NPs was 19.65 µM and 59.54 µM, and for CuONRs@$Au_{0.5}$/$Pd_{0.5}$NPs was 10.46 µM and 31.71 µM.

TABLE OF CONTENTS

CHAPTER 1

CHAPTER 2

CHAPTER 3

CHAPTER 4

LIST OF ABBREVIATIONS

Abs	Absorbance
Au NPs	Gold nanoparticles
CuO NPs	Copper oxide nanoparticles
CuONRs	Copper oxide nanorods
CuONRs@Au	Copper oxide nanorods decorated with gold
CuONRs@Pd	Copper oxide nanorods decorated with palladium
CuONRs@Au/Pd	Copper oxide nanorods decorated with gold and palladium
DLS	Dynamic light scattering
DPBF	1,3-Diphenylisobenzofuran
EDS	Energy dispersive spectroscopy
GO_x	Glucose oxidase
H_2O_2	Hydrogen peroxide
HRP	Horseradish peroxidase
NPs	Nanoparticles
Pd NPs	Palladium nanoparticles
ROS	Reactive oxygen species
SEM	Scanning electron microscopy
SPR	Surface plasmon resonance
TEM	Transmission electron microscopy

TMB	3,3',5,5'-tetramethylbenzidine
UV-vis	Ultraviolet-visible
XPS	X-ray photoelectron spectroscopy
XRD	X-ray diffraction

LIST OF SYMBOLS

D	Particle size
K	Constant (0.94)
λ	X-ray wavelength radiation (1.5406 Å)
β	Full-width at half maximum of the peak (in radians)
2Θ	Bragg angle (degrees)
k	Boltzmann constant
T	Temperature
η	Dispersant viscosity
K_m	Michaelis-Menten constant
V_{max}	Maximum velocity
V_o	Initial Velocity
S	Substrate
In	lin

LIST OF FIGURES

LIST OF TABLES

CHAPTER 1

INTRODUCTION

1.1 Nanotechnology and nanoscience

Nanoscience is the field of science that encompasses the study of materials with minute dimensions in the nanometer scale (i.e. <100 nm). In the past years, the field of nanochemistry was established for the understanding of materials in the nanometer scale. Nanoscale materials are colloids, micelles, polymer molecules and phase-separated block co-polymers.[1] The Royal Society and The Royal Academy of Engineering described nanotechnologies as the modelling, fabrication/assembly, characterization and application of nanostructured systems and devices by manipulating their morphology (size and shape).[2] Norio Taniguchi , a researcher at the University of Tokyo is reported to be the first person to devise the term 'Nanotechnology' in 1974 and he used the term 'Nanotechnology' to refer to the potential of designing materials at the nanoscale.[3] Nanotechnology is also reported to be a multidisciplinary field which encompasses a diverse spectrum of scientific disciplines incorporating physics, chemistry, biology and engineering.[4] Nanotechnology offers the potential to operate at the atomic, molecular and supramolecular levels to fabricate and utilize systems, structures, materials and devices with advanced properties.[3] The advent of nanotechnology and nanoscience commenced with the production, manipulation and utilization of the nanometer-sized materials that possess extensive applications. Nanotechnology is a constantly growing field with many applications in areas such as manufacturing, energy, medical diagnosis, materials, computer chips, and health care.[5] Developments and improvements on analytical techniques such scanning probe microscopy and electron microscopy allowed for the fabrication of nanostructured materials with morphological-dependent properties to be investigated and generated.[2] The carbon nanotubes are at the forefront of the nanostructured materials to be first discovered.[2,6,7]

1.2 Nanomaterials in General

Nanomaterials are an example of products that are procured from the prevalence of nanoscience and nanotechnology. Nanomaterials are described as materials with the size ranging from 1 to 100 nm. The applications of nanomaterials are size dependent, and their sizes affect their optical properties.[8,9] The remarkable properties of nanomaterials include high surface-to-volume ratio making them environmentally unfriendly, predominantly on agricultural ecosystems due to their increased surface area.[5] The high surface to volume ratio enhances the reactivity and alters the mechanical, electrical and optical properties of the material.[4] The properties are also due to the quantum effect which correlates with the small particle size and large surface-to-volume ratio. The quantum effects control or influence the magnetic, thermal and optical properties of nanostructured materials.[3] Nanomaterials can be categorized into carbonaceous, semiconductors, metal oxides, lipids, zero-valent metals, quantum dots, nanopolymers and dendrimers.[5] The physical, chemical and biological properties of nanostructured materials and systems are significantly different from their bulk materials.[4] Silver nanoparticles can be used as bactericide, gold nanoparticles can be used for cancer treatment and titanium at nanoscale can be used for the termination of influenza viruses. The possibility to control and manipulate the size and morphology of the nanostructured materials allows for desired properties for specific applications. The nanomaterials can be constructively modified to be sturdy and durable, biocompatible, more reactive and their electrical properties can be improved. The nanoparticles, carbon nanotubes (single walled and multiwalled) and quantum dots are the classification of nanomaterials that are extensively studied.[9] The two fundamental categories of nanostructured materials are organic and inorganic nanomaterials.[10] The main categories of nanomaterials are: (a) organic nanomaterials, that contain C-H groups such as fullerenes and carbon nanotubes, (b) inorganic nanomaterials, which are subdivided

into metal oxides, metals and quantum dots, and (c) polymer-based nanomaterials such as dendrimers, micelles and liposomes.[10]

1.3 Properties of metal nanoparticles

The optical properties are the most captivating characteristics of nanoparticles. For instance, gold nanoparticles are wine red in colour, silver nanoparticles are yellow-grey in colour and platinum and palladium nanoparticles are black in colour.[8] Nanoparticles can be discovered incidentally in nature and can be manufactured or engineered intentionally. Incidental nanoparticles are obtained as repercussion of volcanic activities and elevated temperature industrial operations such as combustion, welding, grinding, to mention but a few. Incidental nanoparticles are relatively less reactive and bioactive in contrast to their manufactured analogues.[9] The main category of nanomaterials we are focusing on in this work are metal oxides and metal nanoparticles. The colour of nanoparticles has intrinsic and very interesting spectral properties. For example gold nanoparticles with ruby red colour have absorption band at 520 nm for spherical nanoparticles.[11] Silver nanoparticles are yellow in colour with the absorption at 420 nm.[12] The absorption is due to surface plasmon resonance (SPR). The surface plasmon resonance (SPR) is a circumstance or phenomenon whereby facet electrons in the metal are excited by light photons at a specific angle. The incident light photons then disseminate parallel to the metal facet. The angle of inception of surface plasmon resonance (SPR) is dependent on the refractive index of the medium near the metal facet .[13]

1.4 Synthesis of nanoparticles

The preparation of nanoparticles generally incorporates direct and synthetic pathways. There are two different approaches that can be employed in the preparation of nanoparticles, that is top down and bottom up. The Top-down approach: this is the process that results in the formation of nanoparticles from the breaking down of larger solid particles. This breakdown can be achieved by either dry or wet grinding. In dry grinding the solid material is pulverized by either compression or friction utilizing materials such as jet, hammer, shearing and ball milling. Wet grinding makes use of centrifugal and tumbling ball mills and at the same time minimises condensation of the nanoparticles to obtain dispersed nanoparticles from wet grinding.[8] The break-down of larger solid particles is also accomplished by using bulk or film, surface and mold machining by utilizing photolithography.[14] The challenge with assembling nanostructured materials using photolithographic technique is the difficulty in producing sub-100 nm nano-structured materials. This means that photolithography cannot be used for the fabrication of nanostructured materials with the size below 100 nm.[15]

The Bottom-up approach: is a more complex assembly of gaseous or liquid phases based on molecular condensations. The gaseous phase process makes use of the chemical vapour deposition and physical vapour deposition methods. Nanoparticles within the range of 10 – 100 nm can be fabricated using the gaseous method by carefully controlling the reaction.[8] The assembly of atoms or molecules into nanoparticles may be controlled via chemical reactions to form different size nanostructured materials.[3,14] The self-assembly of atoms and molecules may be engineered via templating and non-templating. The templating self-assembly requires the association of biomacromolecules according to a definite sequence, pattern, structure and external force. The examples of such templates include non-ionic surfactants and block co-polymers.[16] The non-templating self-assembly involves the construction of nanostructured materials from building blocks such as atoms and/or molecules with external influence.[17]

Horikoshi[8] mentioned that the synthetic method used for the preparation of nanoparticles using either top-down or bottom-up approaches must fulfil the conditions stated below:

(i) Control of particle size, size distribution, shape, crystal structure and composition distribution.

(ii) Improvement of the purity of nanoparticles.

(iii) Control of aggregation.

(iv) Stabilization of physical properties, structures and reactants.

(v) Higher reproducibility.

(vi) Higher mass production, scale-up and lower costs.

There are different methods used for the synthesis of metal nanoparticles, for an example chemical reduction, sol-gel, laser ablation, thermal decomposition and electrochemical synthesis.

1.4.1 Chemical reduction method

The chemical reduction method is widely used for the synthesis of nanomaterials because it is efficient, simple, economical and it allows for the control of size by changing factors such as molar ratio of the reacting species (i.e. the precursor, capping and the reducing agents).[18,19] In a conventional chemical reduction method, the precursor salt solution is reduced using a suitable solvent and a particular reducing agent.[19,20] For instance, in the synthesis of gold nanoparticles, sodium borohydride is used as a reducing agent for the reduction of gold from Au^{3+} to Au^{0}. The stabilizing agent is essential to control the rate of agglomeration.[19] Typically used stabilizing agents include dendrimers, polymers, block co-polymers and surfactants.[5] The reduction process can either be anteceded or followed by the reaction between the metal ion and the stabilizing agent. The sequence in which the reduction process and the interaction between the metal ion and the stabilizing agent takes place determines and/or affects the structural properties, size and structure of the nanoparticles. This means that, if the reduction

process occurs before the interaction between the metal ion and the stabilizing agent, the structural properties will only be governed by the reduction state. If the interaction between the metal ion and the stabilizing agent occurs before the reduction process, the collective forces between the metal ion and the stabilizing agent will govern the size and the structure of the produced metal nanoparticles.[21]

The key parameters in the synthesis of nanoparticles is the concentration, reaction time, pH, and temperature.[18] The chemical reduction method also offers opportunities for scale-up whenever it is necessary to meet the requirements for mass production.[10] Two most popular methods for the synthesis of gold nanoparticles are Turkevich[22] and Brust method.[23]

1.4.2 Sol-gel method

Sol-gel method is the sedimentation method that is widely used for the preparation of metal oxide nanoparticles. The production of metal oxide nanoparticles is executed in consecutive steps, first the metal oxide solution is changed into a sol by hydrolysis which is followed by polycondensation to a gel.[8] The next step is the drying of a gel. The obtained product is either transformed into a xerogel or an aerogel depending on the used method of drying. The sol-gel method is categorized into aqueous and nonaqueous sol–gel methods.[24] This classification is dependent on the type of solvent used.

(i) Aqueous sol-gel method: this method utilizes water as a reaction medium. The water content contributes oxygen which facilitates the formation of metal oxide. The metal acetates, nitrates, sulfates, chlorides and metal alkoxides are predominantly used as the metal precursors in the aqueous sol-gel method. The use of alkoxides as precursors is predominantly due to the great affinity of alkoxides to water.[24]

(ii) Non-aqueous sol-gel method: in this method organic solvents are used as reaction medium. The organic solvents such as alcohols, ketones and aldehydes provide the oxygen which is required for the fabrication of metal oxides. Additionally, the organic solvents allow for the

tuning of particle size, surface properties, morphology and composition of the resulting metal oxide. The non-aqueous sol-gel method can be surfactant controlled and solvent controlled. The surfactant-controlled procedure involves the direct conversion of a metal precursor into a specific metal oxide at elevated temperatures. This procedure also allows for the manipulation of particle growth, shape and it circumvents aggregation. The solvent-controlled procedure comprises the interaction between the metal halides and alcohols to yield metal oxide nanostructured materials. An example of such metal oxides is SnO_2 nanoparticles, which were formulated by the introduction of tin chloride into benzyl alcohol with continuous stirring. The mixture was instantly dispersed into the solution of THF to form a sol.[24] A sol is a colloidal suspension of solid particles in a liquid. This method ensures high dispersivity of nanoparticles compared to dry methods. In a sol-gel method, the precursors (salt solution) is surrounded by the capping or stabilizing ligand.[8] The morphology and the surface properties of the nanostructured materials can be easily manipulated and controlled using the sol-gel method.[24]

1.4.3 Laser ablation method

The laser ablation synthetic procedure is a green method for the preparation of sturdy noble metal nanoparticles both in aqueous media and in organic solvents. The technique does not require the utilization of the stabilizing agents. This is a top-down approach for the synthesis of metal nanoparticles.[25] Nanoparticles are assembled throughout the liquefaction of a plasma plume which is induced by the laser ablation of a metal plate that is immersed in a liquid solution. The laser ablation synthesis method may probably be an exclusive method for the fabrication of various metal nanoparticles with divergent surface plating in divergent solvents. Examples of noble metal nanoparticles that have been fabricated using the laser ablation synthesis in solution include silver, platinum, gold, copper nanoparticles, to name but a few. Since the laser ablation method produces stable noble metal nanoparticles in both aqueous medium and in organic solvents, this allows for the simple functionalization of nanoparticles

compared to the functionalization of nanoparticles that are produced by the chemical reduction method.[25] The laser ablation synthesis in solution possesses some complications that are associated with the control over nanoparticles size and distribution. Such complications can be mastered by chemical free laser irradiation of noble metal nanoparticles.[25]

1.4.4 Thermal decomposition method

Thermal decomposition is a novel technique for the preparation of stable nanoparticles with uniform size.[26,27] The monodisperse metal nanoparticles fabricated using the thermal decomposition method have been reported to subdue resistance and side effects of traditional cancer drugs.[26] Typical capping agents that have been used in thermal decomposition method include polymers and functional groups of amines, carboxylic acids, hydroxyl groups and thiols.[26] Carboxylic acids and alkyl amines as capping agents allow for the assembling of monodisperse nanoparticles when using the thermal decomposition method.[26,28] The conventional synthesis of nanomaterials is mainly centralized on thermal decomposition of precursors in high-boiling solvents at elevated temperatures, typically 250 – 300 °C. The separation of highly reactive and unstable nanocrystals can be difficult. The doped nanocrystals are a typical example that illustrate such challenges. In doped nanocrystals the dopants are located/positioned a few lattice parameters from the nanocrystal facet and this leads to the thermal release of the dopants. The challenges that have been presented reduce the scope of metastable nanocrystalline phases that can be fabricated via thermal decomposition.[29,30,31] The temperature and pressure at which the thermal decomposition reaction occurs is affected by the inherent features of the metal ion and the interaction between the metal ion and the stabilizing and capping ligands.[32]

1.4.5 Electrochemical reduction method

The electrochemical reduction is fascinating due to the fact that it facilitates the fabrication of high purity nanoparticles using a rapid and straightforward technique. The control and manipulation of nanoparticle size is accomplished by altering the current. The electrochemical reduction technique is "green" since it avoids utilizing toxic reducing agents.[33] The electrochemical reduction is widely used because of the simple operation, reproducibility, low cost and high flexibility.[34,35] In the electrochemical reduction technique organic monomers have been used as electrostatic stabilizers while polymeric compounds were used as steric stabilizers. The ionic organic compounds can be utilized concurrently as both stabilizers and support electrolytes and therefore avoiding the necessity of supplementary chemicals.[33] It has been reported that steric stabilizers allow for the fabrication of more stable nanoparticles than electrostatic stabilizers.[33] The electrochemical reduction of metal precursors on the cathode results in the deposition of the metal on the cathode surface. The electrochemical reduction method has been used in the preparation of copper nanoparticles. The electrochemical reduction of an aqueous solution of Cu^{2+} ions was performed in the absence of surfactants. The copper nanoparticles were procured with small traces of copper oxide nanoparticles also being produced as minor products due to the absence of the surfactants.[36] Silver nanoparticles were prepared by electrochemical reduction method in silver-exchanged zeolite modified electrodes (ZMEs). Nonetheless, it was challenging to attain monodisperse silver nanoparticles due to the incompact configuration of zeolite films in regular ZMEs.[37,38] The monodisperse silver nanoparticles were prepared by electrochemical reduction using faujasite zeolite film modified electrodes (CZFMEs-FAU).[38]

1.5 Metal and metal oxide nanoparticles

Metal nanoparticles have attracted a lot of scientific research for over a century because they show great capacity for the advancement of nanotechnology and nanoscience.[39] Metal nanoparticles can be fabricated and modified with different functionalities to allow them to be coupled with ligands, antibodies and drugs. The modification and conjugation of metal nanoparticles with ligands, antibodies and drugs has resulted in the use of these nanostructured materials in a variety of applications. Typical examples of such applications include biotechnology, magnetic separation, drug delivery, preconcentration of target analytes, diagnostic imaging, to name but a few.[39] Metallic elements constitute a broad spectrum of nanoparticles including s-block, p-block metals and the transition metals. Metallic nanoparticles can be made up of one or more metallic elements.[40] The properties of metal nanoparticles such as ionization energy, electron affinity, cohesive energy, absorption frequency, electrical conductivity and chemical reactivity demonstrate the size dependence.[40] Metal nanoparticles possess different properties in comparison to their bulk metals due to the high surface-to-volume ratio and a large number of accessible active sites per unit area.[41] One of the fascinating applications of metal nanoparticles is the use in catalysis. The manipulation and control of nanoparticle size and shape of metal nanoparticles has prompted the production of high-performance heterogeneous catalysts.[41] Metal nanoparticles can be assembled in gaseous phase, in aqueous medium, and anchored on a substrate, matrix and bacterial cells.[40] The high surface-to-volume ratio is the important attribute for catalytic applications. Ultrafine metal nanoparticles contribute a large number of catalytic active sites for catalysis to proceed. The multiple catalytic sites enhance reactivity, and atom efficiency and minimize the cost of the metal catalyst.[41] Due to the high surface energy, ultrafine metal nanoparticles (± 3 nm) are susceptible to aggregation and instability during catalysis and therefore resulting in depleted catalytic activity and recyclability. To circumvent the challenge of aggregation, the synthesis

technique which involves the reduction of metal precursors in aqueous medium in the presence of divergent capping agent has been developed. The examples of such capping agents include dendrimers, oleylamines and polyvinyl pyrrolidone.[41]

In the past few years an increased attention has been devoted to the study of metal oxide nanotechnologies due to their high chemical activity and specificity and this has resulted in the application of these systems in catalysis.[42] The transition metal oxide nanoparticles have also been extensively applied in energy storage and nanomaterial synthesis.[43] Transition metal oxide nanoparticles possess distinctive properties which cover complete features of solid state and materials science.[42,44] High selectivity is one prominent property of transition metal oxide nanoparticles which makes them suitable for catalytic applications.[42] The high selectivity allows for the differentiation inside chemical groups and geometrical orientation that would result in high yield of the desired product.[42] Metal oxide nanoparticles may be considered environmentally unfriendly due to the special dissolution properties and electronic charges.[45] Various transition metal oxide nanoparticles with high dispersity have been prepared successfully. Typical examples of such nanomaterials include MnO_x, CoO, Fe_3O_4 and NiO, to name but a few.[43]

1.5.1 Gold nanoparticles

Gold nanoparticles has been of particular interest due to its interesting properties. A lot of research has been investigated for nanotechnology and nanoscience due to its fascinating characteristics.[46] These interesting aspects, including their distinctive electronic and optical properties, chemical inertness, biocompatibility, peroxidase activity, self-assembly, near-field plasmon coupling, crystal growth, and electron-transfer, have made gold nanoparticles suitable for variety of applications.[46,47] In bulk form, gold is shiny-yellowish in colour and at nanoscale the colour of gold nanoparticle solution ranges from purple to wine-red. The formation of gold nanoparticles in solution is displayed by the changes in colour from bluish, purple to wine-red. Gold nanoparticles are one of the stable noble metal nanoparticles.[48] The interest in gold nanoparticles emerges from their sensitivity to environmental changes and the control of size and shape during synthesis.[49] Gold nanoparticles possess exceptional biostability, optical properties, and catalytic activity.[50] Due to their fascinating properties, gold nanoparticles can be used in a variety of applications, such as catalysis, biology, diagnostics, therapeutics, and sensing.[48,50]

There are diverse methods that can be used for the preparation of gold nanoparticles. Turkevich method is a well-known method that is widely used for the preparation of gold nanoparticles.[22,50] The Turkevich method is simple and it allows for the fabrication of spherical gold nanoparticles. It further allows for the easy control and manipulation of nanoparticle size, morphology and functionality.[50,51] Turkevich method involves the reduction of Au^{3+} to Au^{0} using sodium citrate in an aqueous solution. The sodium citrate is used as both the reducing and stabilizing agents, and for the control of particle size. Sodium citrate also prevents the aggregation of the nanoparticles by forming a thin layer on the surface of gold nanoparticles. Turkevich method yields gold nanoparticles with the size ranging from 10 - 20 nm.[48,51] Another method that is frequently used in the preparation of gold nanoparticles is a Brust and Schriffin

method. Brust and Schriffin method involves alkanethiol-stabilization of gold nanoparticles via a two-phase reduction of tetraoctylammonium bromide (TOABr) as a phase transfer reagent and sodium borohydride as a reducing agent.[51] The Brust and Schriffin method yields thermally and air stable nanoparticles with adjustable size and minimized dispersity.[48]

The optical properties of gold nanoparticles make them suitable for use in diverse applications. In order to attain the desired applications, the size and shape should be carefully controlled during the synthesis.[50] Different reaction conditions such as concentration, temperature and pH influence the morphology of the nanoparticles.[50] Gold nanoparticles have a high surface-to-volume ratio allowing for the functionalization of drugs and targeting agents.[51] Surface plasmon resonance (SPR) and fluorescence quenching are the predominant properties of gold nanoparticles. Gold nanoparticles display a distinct SPR band at 500 – 550 nm. The orientation and location of the SPR band is dependent on particle size and shape. The SPR band is due to the vibrations of conduction electrons that are excited by the incident photons.[51] The citrate capping agent on gold nanoparticle surface can be exchanged for thiols to yield monolayer protected gold nanoparticles. This is an equilibrium process in which the surface modifications on gold nanoparticles can be influenced by reaction kinetics such as time and percent volume of the functional ligand. The exchange of the capping agent on the nanoparticle surface can occur through diverse interactions such as specific binding affinity, electrostatic and hydrophobic interactions.[51,52] One example of such thiol moieties is glutathione, which is a thiol-containing tripeptide (Glu-Cyst-Gly). Glutathione binds onto gold nanoparticle surfaces via the thiol moiety to form Au-S bond.[53]

1.5.2 Palladium nanoparticles

The dominant utilization of palladium in the field of nanocatalysis is due to its variable reactivity.[54] The versatility of palladium is due to its potential to sustain a large diversity of different oxidation states.[54] Different reaction conditions such as pH, temperature and time control the morphology (size and shape) and stability of palladium nanoparticles. Palladium and platinum nanoparticles are extensively applied in drug delivery, catalysis and cancer therapy.[55] Palladium nanoparticles demonstrate highly specific and selective therapeutic applications. The specific and selective therapeutic properties of palladium nanoparticles are size and shape dependent.[55] Palladium nanoparticles have been synthesized using a green method when plant species are used. The prepared palladium nanoparticles have been used in heterogeneous and homogeneous catalysis.[55,56] Metal nanoparticles possess highly active surface atoms and may induce nanoparticle instability during the catalytic process.[56] Palladium nanoparticles have been used more in different applications, for instance chitosan-graphene doped palladium nanoparticles were used in the fabrication of biosensors for glucose detection.[55] While graphene supported palladium nanoparticles were applied in recyclable heterogeneous catalytic reduction of nitroarenes utilizing sodium borohydride.[55] Ethylene glycol has been extensively employed in the polyol synthesis of metal nanoparticles.[54,57] Palladium nanoparticles that are fabricated using ethylene glycol typically display structures with different shapes such as cubes, bars, cuboctahedra. The assembly of the single-crystal structures is ascribed to the rapid reduction in ethylene glycol at elevated temperatures.[54]

1.5.3 Copper oxide nanoparticles

The interest in copper oxide nanoparticles emerges from their feasible applications in various fields of science. The applications of copper oxide nanoparticles include gas sensing, catalysis, magnetic phase transitions, superconductors, to name but a few.[58] Copper oxide possesses exceptional electrical, physical, optical and magnetic properties.[58] Copper oxide nanoparticles can act as catalysts. Copper oxide is an ionic solid in bulk form, but it retains conductivity that is between that of an insulator and a metal at nanoscale.[59] The different methods of preparing copper oxide nanoparticles are sonochemical, sputtering laser, electrochemical reduction, and decomposition of precursors.[59] These methods suffer from the disadvantages of high cost, toxicity and use of hazardous chemicals. Thus, in this work sol-gel method was investigated for the preparation of copper oxide nanoparticles because it is simple, economical and it produces high yield.

1.6 Bimetallic nanoparticles

Bimetallic nanoparticles are fabricated using two different metal nanoparticles that are oriented in different mixing patterns. These systems have recently attracted a lot of attention compared to their monometallic analogues due to their distinctive optical, catalytic and electronic properties. The bimetallic nanoparticles display coalition of properties and show advanced properties due to the synergistic effect which emanates from the integration of two metal nanoparticles.[60] The particle morphology of a bimetallic system is dependent on the reaction conditions and the method of synthesis.[60] The approach of integrating gold with other transition metals enhances the catalytic properties of gold nanoparticles. The integration leads to the formation of bimetallic nanoparticles with elevated catalytic activity.[61] A typical example of a bimetallic system is Au-Cu bimetallic alloy nanoparticles.[61] Rout and co-workers reported that the interest in these bimetallic systems is due to high catalytic activity, and low cost of copper and high resistance to oxidation.[61] The aggregation is one of the limitations that are associated with bimetallic nanoparticles. The aggregation can be ascribed to the high surface energy which may lead to reduced lifetime and catalytic activity. To minimize aggregation, nanoparticles can be anchored on support materials such as polymers and metal oxides.[61] Alloying is a powerful technique that can be utilized to improve reactivity of metal nanocatalysts by manipulating morphological, chemical and electronic properties. The introduction of a secondary metal to prepare bimetallic nanoparticles induces some modifications in the electronic structure and provides an alternative active site for the reaction to proceed.[62] Mistry emphasized that the structure and stability of bimetallic nanoparticles is of utmost importance since the two metals are the determining factors of reactivity.[62] The structure of bimetallic nanoparticles is determined by the contribution of each metal to the resulting bimetallic system and therefore leading to extended applications. The combination of two metals in a bimetallic system results in the emergence of new properties leading to different mixing patterns/architectures depending

on the method of preparation.[63] Bimetallic nanoparticles can be fabricated into different structures. **Figure 1.1** shows different structures of bimetallic systems.

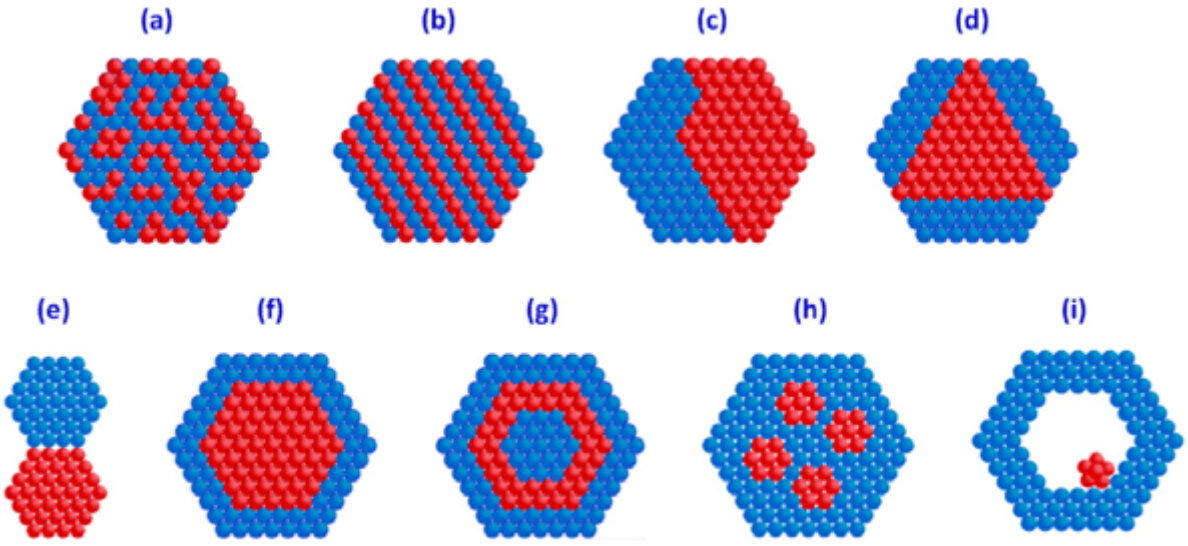

Figure 1.1: Structures of bimetallic nanoparticles: (a) mixed alloys, (b) random alloys, (c) subclusters with two interfaces, (d) subclusters with three interfaces, (e) subclusters with small number of A–B bonds, (f) core–shell nanoparticles, (g) multishell core–shell nanoparticles, (h) multiple small core material coated by single shell material, and (i) movable core within hollow shell material.[60]

1.7 Nanocomposites

In the past decade a considerable advancement in the manufacturing of noble metal and metal oxide nanocomposites has been observed. Noble metal and metal oxide nanocomposites have been explored extensively due to their photocatalytic, electronic, magnetic and photovoltaic properties.[64] The structural properties of the noble metal and metal oxide nanocomposites allowed for the utilization of these nanostructured materials in different applications such as heterogeneous catalysts in chemical processing, environmental remediation, chemical production, to name but a few.[65] The noble metal and metal oxide nanocomposites demonstrate excellent catalytic activity in contrast with their single analogues.[65,66] The thriving applications of these nanohybrid systems in different research areas are controlled by their structure, composition and particle size.[64] Since the catalytic activity of these nanostructured materials is size dependent, a facile and economical synthesis method is required to fabricate metal and metal oxide nanocomposites.[65] The ability to control the integration of noble metals and metal oxides into one unique nanostructure combines different properties and gives rise to new properties with synergistic catalytic properties compared to their individual nanoparticles.[64] Various synthesis techniques have emerged for the preparation of noble metal and metal oxide nanocomposites.

The frequently used methods for the preparation of these nanomaterials are impregnation, coprecipitation and deposition precipitation methods.[64,65,67,68] The deposition precipitation method is based on the modification and conversion of the metal hydroxide deposited on the prepared metal oxide nanoparticle facet.[65,67,68] The impregnation methods involve the calcination under the flow of hydrogen.[65] The general structure of the nanocomposites is one of the predominant aspects that govern the physical properties of nanohybrids.[64] The primary challenge with the fabrication of nanohybrid systems is the combination of two different materials with dissimilar composition to produce distinctive hybrid systems with different

functionalities.[64] **Figure 1.2** shows the diagrammatic illustration of different structures of noble metal (NM)–metal oxide (MO) nanocomposites.[64]

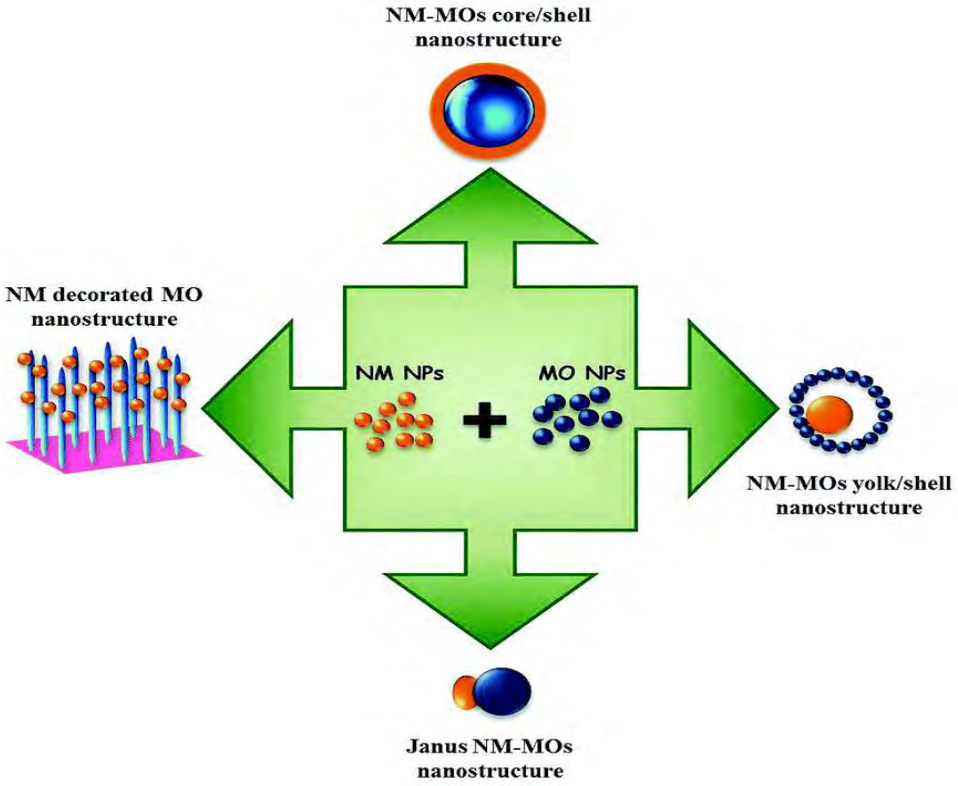

Figure 1.2: Diagrammatic illustration of different structures of noble metal (NM)–metal oxide (MO) nanocomposites.[64]

1.8 Characterization of nanoparticles

The strength of the successful preparation of nanomaterials is their characterization. Different spectroscopic and microscopic techniques are employed for the characterization of nanostructured materials. The characterization techniques used in this work include X-ray diffraction (XRD), Dynamic light scattering (DLS), Transmission electron microscopy (TEM) and Energy dispersive spectroscopy (EDS).

1.8.1 X-ray diffraction (XRD)

X-ray powder diffraction provides significant contribution in materials research and development since numerous materials and minerals are not readily obtainable in single-crystal form.[69] In XRD, an X-ray light interacts with the sample matter and then diffracted by the facet atoms in the sample. The diffraction of the X-rays is due to the coalition of two different occurrences, (i) scattering by each individual atom, and (ii) interference between the waves scattered by these atoms.[70] X-ray powder diffraction can be used for different functions including qualitative identification, quantitative analysis, unit cell matrics, crystal orientation, residual and applied stress and microstructural features.[69] In the qualitative identification, the phases that exist in the material sample are identified using the powder pattern as a fingerprint of the phase which is compared to already existing powder patterns in the database. The quantitative analysis of each phase that exists in a multiphase material can be conducted.[69] The size and shape of crystalline materials can be confirmed using Debye-Scherrer equation.

$$D = \frac{k\lambda}{\beta \cos\theta} \qquad (1.1)$$

D is the particle size, K is the constant (0.94), λ is the X-ray wavelength radiation (1.5406 Å), β is the full-width at half maximum of the peak (in radians) and 2Θ is the Bragg angle (degrees).[71]

X-ray powder diffraction can be used in solid analysis, phase diagram work, and determination of the true density of materials since the lattice parameters of a material are transformed with change in chemical composition. The distribution functions that illustrate the crystalline alignment in polycrystalline materials can be evaluated. The crystalline size and micro strain inside crystallites and density can be ascertained.[69]

1.8.2 Dynamic light scattering (DLS)

Dynamic Light Scattering (DLS) is a widely used and non-invasive analytical technique for the characterization of nano and micro size particles in solution This analytical technique is widely used due to sensitivity to small size and low scattering particles, simplicity and it is economical.[72] Dynamic light scattering analyses the particles in solution, and it allows for monitoring the effect of ionic strength, pH stability, thermal and chemical stress.[72] The technique also allows for the determination of particle size, aggregation temperature and the diffusion parameter.[72,73] DLS quantifies the time-dependent oscillations in the scattering intensity of the specimen.[73] The oscillations in the scattering intensity emanate from the particles that experience Brownian motion.[73,74] The oscillations in the intensity of the scattered light are surveyed using the autocorrelator. The autocorrelator is used to ascertain the autocorrelation function of the signal.[73] The diffusion coefficient D is obtained by estimating the velocity of the Brownian motion. The hydrodynamic diameter can be obtained by converting the diffusion coefficient D using the Stokes-Einstein equation.

$$D_H = \frac{kT}{3\pi\eta D} \qquad (1.2)$$

k is the Boltzmann constant, T is the temperature and η is the dispersant viscosity.[73,74] Using the DLS, the sample is introduced in the instrument using a disposable cuvette for size determination measurements. The scattered light is estimated using the Rayleigh scattering model whereby the scattered intensity is relative to the particle size. Due to high sensitivity,

the technique does not discriminate contaminants and aggregated samples and therefore leading to skewed distribution results.[72] The skewness of the results is typically observed during the particle size determination. Since the technique is sensitive to contaminants and aggregated samples, this can render the sample preparation long and challenging.[72] Frequently micro filters are used remove these aggregates and contaminations.

1.8.3 Transmission electron microscopy (TEM)

The transmission electron microscope (TEM) is the principal instrumentation for the thorough characterization of nano-sized materials. The imaging, modelling, and manipulation of matter can be achieved using the transmission electron microscope (TEM).[75] In electron microscopy, the standard procedure for imaging is controlled by the target lens defocus.[76] The materials at nanoscale are fabricated into specific dimensions for example 1D, 2D and 3D, the TEM is suitable for analysing each material presented on these specific dimensions. 1D is suitable for the analysis of nanomaterials for direct viewing, 2D is suitable for analysing interfaces, 3D analysis incorporates multilayer, semiconductor devices, nano porous structures and functional materials.[75] TEM operates by channelling of the beam of electrons across the sample and studying the interaction between the beam of electrons and the specimen. The size, shape and structure of the nanomaterials are some properties that can be derived from using TEM.[77]

1.8.4 Energy dispersive X-ray spectroscopy (EDS)

The energy dispersive X-ray spectroscopy (EDS) is widely employed in the qualitative and semi-quantitative investigation of materials. Normally the scanning electron microscopy (SEM) is coupled with the EDS technique to allow for characterization of materials with the SEM imaging observed.[78] The SEM-EDS technique uses secondary and backscattered electrons for morphological examination while the X-rays are used for quantitative identification of specimens. The detection limit of the EDS is dependent on the texture and roughness of the specimen. The EDS can detect elements in the concentration range 1 – 10 wt%.[78] The EDS technique is able to display elemental distribution maps.[78] In the EDS experiment, a beam of electrons typically at 10 – 20 keV, hit the surface of the sample and therefore resulting in the emission of X-rays with energy that is dependent on the material sample under investigation. The X-rays are initiated in a region approximately 2 μm in depth.[40]

1.9 Natural Enzymes

Enzymes are proteins that contain a number of amino acids arranged specifically for a biological application.[79] Natural enzymes contribute a significant contribution in biological reactions in living organisms.[80] The enzymes accelerate the rate of biochemical reactions by coupling with small molecules in the active site. The enzyme catalytic groups are oriented such that they interact effectively with the substrate.[79] The enzyme catalyzed reactions are typically governed by the enzyme geometry such that the products of a particular array are assembled.[79] They are highly specific to the substrate they catalyze. Enzymes have enhanced reaction rates. The enzyme catalyzed reactions are the fundamentals of the metabolism of all the organisms in existence. Enzyme catalyzed reactions provide great approaches for the industry to execute simple and effective, efficient, and inexpensive biocatalytic conversions.[81] The enzyme technology is perceived as the utilization of free enzymes in the manufacture of goods and services. Enzyme technology is a versatile discipline with a variety of applications in agriculture, chemical, cleaning, energy, food, materials and pharmaceutical industries. Enzyme-based operations are already important in the fabrication of chemicals and pharmaceuticals.[81] Reactions that involve the utilization of enzymes are typically conducted at mild reaction conditions. The enzymes are reported to be enantioselective and stereoselective and this property is significant in pharmaceutical applications.[82] The integration of the activity of different enzymes can result in the mimicking of the operations in living cells and therefore producing the suitable complex and/or composite for the desired applications.[82] The reactions that are catalyzed by enzymes can be coupled with chemical reactions in one-pot chemo-enzymatic synthesis.[82] Natural enzymes possess various limitations such as ease of denaturation, difficult preparation in highest purity, recycling and high cost.[80] These limitations have impeded the applications of natural enzymes in different industries. To overcome such limitations artificial enzymes have been developed as replacements for natural enzymes.

1.10 Horseradish Peroxidase (HRP)

Biological catalysts have been used extensively in enzyme catalyzed reactions because they possess high substrate specificity and efficiency at mild reaction conditions. Horseradish peroxidase is a typical example of an enzyme that is frequently utilized as the catalyst.[83] Horseradish peroxidase (HRP) is a heme-containing enzyme that has been extensively examined for more than 100 years.[84] Peroxidases are a class of enzymes that catalyze reactions in vivo whereby peroxides such as hydrogen peroxide and lipid peroxide are reduced while simultaneously a redox substrate is being oxidized.[85] Majority of peroxidases display high substrate specificity; an example of such peroxidases is Cytochrome c peroxidases. Horseradish peroxidase (HRP) is frequently utilized as a conventional peroxidase for the evaluation of peroxidation reactions.[85] HRP uses hydrogen peroxide to oxidize diverse organic and inorganic substrates.[84] Typical examples of such substrates are benzidine and aromatic amines. HRP is reported to be efficient for both one electron and two electron oxidation depending on the used substrate.[86] HRP is used for clinical diagnostic kits and immunoassays.[84] The HRP catalyzed reactions can be demonstrated by the equations (1.3 – 1.5). The production of radical species in HRP-catalyzed reactions provides an insight into some of the potential in vivo functions in the plant.[84] The most commonly used reducing substrates include aromatic phenols, phenolic acids, indoles, amines, and sulfonates.[84]

$$HRP + H_2O_2 \longrightarrow \text{Compound I} + H_2O \qquad (1.3)$$

$$\text{Compound I} + TMB \longrightarrow \text{Compound II} + TMB_{ox} \qquad (1.4)$$

$$\text{Compound II} + \text{TMBox} \longrightarrow HRP + TMB_{ox} \qquad (1.5)$$

1.11 Enzyme kinetic parameters

The understanding of enzyme kinetics contributes a significant part in fulfilling the progression from the lab scale enzyme investigations to the industrial applications. The efficient investigation on the reactivity of enzymes in different controlled reaction conditions displays the reaction mechanism, activation and deactivation of the enzyme. These investigations also reveal the reactivity of enzymes towards a particular substrate.[87] The kinetic data together with the 3D morphological properties and mechanism derived from the crystallographic data aid as an efficient method for understanding the operating concept of enzymes. This methodology assists in formulating therapeutic molecules.[87] Different environmental conditions such as temperature, pH, solution ionic strength, substrate concentration influence efficiency and activity of enzymes.[87] The kinetic data in combination with the graphical representation substantiate the data and contribute a significant role in understanding the enzyme mechanism. The kinetic studies on enzymes can be categorized into steady-state kinetics, transient-state kinetics and rapid-equilibrium kinetics. The steady-state kinetics is established on the principle that every individual enzymatic step remains in steady state though the external environment is altered consistently.[87] The steady-state kinetic model is the fundamental procedure for examining enzymatic reactions.[88]

The Michaelis-Menten model is the basic method for the analysis of the steady-state kinetics of enzymes. The Michaelis-Menten equation is typically used for the approximation of the kinetic parameters, V_{max} (maximum velocity) and K_m (Michaelis-Menten constant). The Michaelis-Menten equation is normally used for the single-enzyme and single-substrate systems. The equation illustrates the initial rate of the product formation for the enzyme catalyzed reactions.[89] The Michaelis-Menten model for the reaction relating to the reaction velocity and substrate concentration for a system whereby the substrate binds to an enzyme to form the enzyme-substrate complex is given by Eq. (1.6):

$$V = \frac{V_{max}\,[S]}{K_m\,[S]} \qquad (1.6)$$

V is the initial velocity and [S] is the substrate concentration. At low substrate concentration [S], the initial velocity V increases linearly with substrate concentration [S]. As the substrate concentration increases, depreciation from linearity occurs and the initial velocity slows down until it reaches saturation and the maximum velocity is obtained at the high substrate concentration.[89] **Table 1.1** shows the comparison of steady-state kinetic parameters for different nanomaterials as nanozymes. The maximum reaction velocity (V_{max}) and the Michaelis-Menten constant (K_m) are derived from the Lineweaver-Burk (double reciprocal) plots using equation (1.7):

$$\frac{1}{V_0} = \frac{K_m}{V_{max}\,[S]} + \frac{1}{V_{max}} \qquad (1.7)$$

Table 1.1: Comparison of steady-state kinetic parameters for different nanomaterials.

Catalyst	Substrate	K_m (mM)	V_{max} ($M.s^{-1}$)
HRP[90,91]	H_2O_2	0.263 - 3.70	3.78×10^{-8} - 8.71×10^{-8}
	TMB	0.434 - 0,228	3.07×10^{-8} - 10.0×10^{-8}
Fe_3O_4MNPs[91]	H_2O_2	154	9.78×10^{-8}
	TMB	0.098	3.44×10^{-8}
$Fe_{0.5}Co_{0.5}$NPs[92]	H_2O_2	0.06	1.32×10^{-7}
	TMB	1.79	4.56×10^{-7}
FeNPs[92]	H_2O_2	0.32	4.10×10^{-7}
	TMB	0.38	2.38×10^{-7}
CoNPs[92]	H_2O_2	1.14	1.72×10^{-8}
	TMB	5.09	9.98×10^{-8}
Co_3O_4NPs[93,94]	H_2O_2	140.07	12.1×10^{-8}
	TMB	0.037	6.27×10^{-8}
$ZnFe_2O_4$MNPs[93]	H_2O_2	1.66	7.74×10^{-8}
	TMB	0.85	13.31×10^{-8}
CeO_2/NT-TiO_2@0.1[95]	H_2O_2	0.04	2.27×10^{-8}
	TMB	0.097	5.54×10^{-8}
H_2TCPP-CeO_2NPs[96]	H_2O_2	0.254	1.31×10^{-8}
	TMB	0.0854	4.34×10^{-6}
CeO_2NPs[96]	H_2O_2	0.278	0.87×10^{-8}
	TMB	0.274	1.59×10^{-8}

NPs (nanoparticles), MNPs (magnetic nanoparticles), NT (nanotubes) and H_2TCPP (meso-tetra(4-carboxyphenyl)porphyrin).

1.12 Glucose detection

Diabetes is chronic disease and a universal health issue at the forefront of the major causes of mortality and disabilities in the world. Diabetes is a metabolic illness that prompts irregular blood sugar levels which triggers metabolic pathways related to inflammation and apoptosis events.[97] The detection and control of diabetes mellitus necessitates tight surveillance of blood glucose levels.[98] Glucose biosensors play a significant role in the diagnosis of diabetes and also in the food and biotechnological processes.[99] Conventionally, biosensors are described as analytical devices that are used for the detection of different analytes by integrating the biological component with a physicochemical detector such that a biological response is converted into an electrical signal.[99] Glucose biosensors have been widely used in industrial, environmental and biomedical applications. Glucose biosensors are typically used in clinical medicine for examining and detecting blood glucose levels in diabetic patients.[97] Electrochemical biosensors that incorporate the use the enzyme glucose oxidase (GOx) have been reported for the detection of glucose owing to their simplicity, selectivity and sensitivity, and direct point of care assays.[97] Nevertheless, the drawbacks associated with these biosensors remain due to the low efficiency of enzyme immobilisation onto the solid electrode. To circumvent these challenges divergent nanomaterials with distinct morphologies have been used.[97] Various nanomaterials such as nanoparticles, nanorods, nanowires, nanosheets and nanotubes have been utilized as glucose sensors due to their high surface-to-volume ratios. The high surface-to-volume ratio allows for high loading and it contributes the microenvironment to maintain stability and blocks leakage of the immobilised enzymes.[97] Current progress in nanomaterials research has led to the advanced enzymatic biosensors due to the prominent morphological and physicochemical properties.[99] Enzymatic biosensors are largely explored despite their poor stability which leads to shortened life-times and impedes some of their applications. To supplement the convenience of enzymatic glucose biosensors much attention

has been devoted to enhancing their stability and sensitivity using nanomaterials.[99] **Table 1.2** shows the comparison of the performance of different nanomaterials towards the detection of glucose.

Table 1.2: Comparison of the performance of different nanomaterials towards the detection of glucose.

Nanozyme	Linear range	Limit of detection
Bimetallic Bi/Pt[100]	1 - 100 µM	0.20 µM
Cu-Pd/rGO nanocomposites[101]	0.50 - 50 µM	0.29 µM
3D graphene/Fe_3O_4 − AuNPs[102]	0.020 – 0.19 µM	12 nM
Ficin/SiO_2@Fe_3O_4 hybrid[103]	2 − 10 µM	0.50 µM
CuO−Au alloy[104]	0 − 30 µM	0.68 µM
Fe_3O_4@SiO_2-NH_2-Au@$Pd_{0.30}$NPs[105]	0.010 - 60 µM	60 nM
MoS_2-$Pt_{74}Ag_{26}$ nanohybrids[106]	5 – 150 µM	1.2 µM
FeOOH/N-doped carbon nanosheets[107]	0.080 µM − 0.80 mM	0.2 µM
Gold nanowires[108]	0.10 – 20 mM	30 µM
CuONPs[109]	0.10 – 8.0 mM	5 µM

1.13 Summary of the thesis aims

(i) The synthesis and characterization of spherical CuO nanoparticles (CuONPs), copper oxide nanorods (CuONRs), CuONRs decorated with gold (CuONRs@$Au_{1.0}$NPs), CuONRs decorated with palladium (CuONRs@$Pd_{1.0}$NPs) and CuONRs decorated with gold and palladium (CuONRs@$Au_{0.5}$/$Pd_{0.5}$NPs).

(ii) The investigation of the peroxidase-like activity of spherical CuO nanoparticles (CuONPs), copper oxide nanorods (CuONRs), CuONRs decorated with gold (CuONRs@$Au_{1.0}$NPs), CuONRs decorated with palladium (CuONRs@$Pd_{1.0}$NPs) and CuONRs decorated with gold and palladium (CuONRs@$Au_{0.5}$/$Pd_{0.5}$NPs).

(iii) The investigation of reactive oxygen species (ROS) generation using DPBF (radical quencher) for spherical CuO nanoparticles (CuONPs), copper oxide nanorods (CuONRs), CuONRs decorated with gold (CuONRs@$Au_{1.0}$NPs), CuONRs decorated with palladium (CuONRs@$Pd_{1.0}$NPs) and CuONRs decorated with gold and palladium (CuONRs@$Au_{0.5}$/$Pd_{0.5}$NPs).

(iv) The detection of glucose using the prepared spherical CuO nanoparticles (CuONPs), copper oxide nanorods (CuONRs), CuONRs decorated with gold (CuONRs@$Au_{1.0}$NPs), CuONRs decorated with palladium (CuONRs@$Pd_{1.0}$NPs) and CuONRs decorated with gold and palladium (CuONRs@$Au_{0.5}$/$Pd_{0.5}$NPs).

References

1. G. M. Whitesides, Small 2005 (1) 172 - 179.

2. A.D. Maynard, Ann. Occup. Hyg., 2007 (51) 1 - 12.

3. N.A. Ochekpe, P.O. Olorunfemi, N.C. Ngwuluka, Trop J Pharm Res, 2009 (8), 265 - 274.

4. S. Neethirajan, D.S. Jayas, Food Bioprocess Technol, 2011 (4) 39 - 47.

5. F. Aslani, S. Bagheri, N. M. Julkapli, A.S. Juraimi, F.S.G. Hashemi, A. Baghdadi, Sci. World J., 2014 (641759) 1 - 28.

6. D.S. Bethune, C.H. Klang, M.S. De Vries, Nature, 1993 (363) 605 - 607.

7. S. lijima, Nature, 1991 (345) 56 - 58.

8. S. Horikoshi, N. Serpone, *Microwaves in Nanoparticle Synthesis: fundamentals and applications*, Germany, Wiley-VCH, 2013, pp 1 – 16.

9. T. Lobanova-Shunina, Yu Shunin, Comput. Model. New Technol., 2017 (21) 28 - 56.

10. V.R. Manikam, K.Y. Cheong, K.A. Razak, Mater. Sci. Eng. B, 2011 (176) 187 - 203.

11. D. Yao, T. Song, B. Zheng, S. Xiao, F. Huang, H. Liang, Nanotechnology, 2015 (26) 425601 (1 - 11).

12. D.K. Bhui, H. Bar, P. Sarkar, G.P. Sahoo, S.P. De, A. Misra, J. Mol. Liq., 2009 (145) 33 - 37.

13. X. Zhu, T. Gao (2019) "Spectrometry", *in*. G. Li (Ed), *Nano-inspired Biosensors for Protein Assay with Clinical Applications*, China, Elsevier, pp 253.

14. D.D Majumder, R. Banerjee, C.H. Ulrichs , I. Mewis, IETE Tech Rev, 2007 (24) 9 - 25.

15 V. Balzani, Small 2005 (1) 278 - 283.

16. P. Guo, J. J. Nanosci. Nanotechnol., 2005 (5) 1964 - 1982.

17. T. Liu, C. Burger, B. Chu, Prog. Polym. Sci., 2003 (28) 5 - 26.

18. A. Khan, A. Rashid, R. Younas, R. Chong, In Nano, Lett, 2016 (6) 21 - 36.

19. H.H. Nersisyam, J.H. Lee, H.T. Son, C.W. Won, D.Y. Maeng, Mater. Res. Bull., 2003 (38) 949 - 956.

20. T.M.D. Dang, T.T.T. Le, E. Fribourg-Blanc, M.C. Dang, Adv. Nat. Sci.: Nanosci. Nanotechnol., 2011 (2) 015009 (1 - 6)

21. T. Naoki, Y. Tetsu, New J. Chem., 1998 (22) 1179 - 1201.

22. J. Turkevich, P.C. Stevenson, J. Hillier, Discuss. Faraday Soc., 1951 (11) 55 - 75.

23. M. Brust, M. Walker, D. Bethel, D.J. Schriffin, R.J. Whyman, Chem. Soc., Chem Commun. 1994, 801 - 802.

24. B.G. Rao, D. Mukherjee, B.M. Reddy (2017) "Novel approaches for the preparation of nanoparticle", *in*. D. Ficai, A.H. Grumezescu (Eds), *Nanostructures for Novel Therapy: Synthesis, characterization and applications*, Romania, Elsevier, pp 1 -36.

25. V. Amendola, M. Meneghetti, Phys.Chem.Chem.Phys., 2009 (11) 3805 – 3821

26. A.T. Odularu, Bioinorg. Chem. and Appl., 2018 (9354708) 1 - 6.

27. O. Masala, R. Seshadri, Annu. Rev. Mater. Res., 2004 (34) 41–81.

28. C. N. R. Rao, P. J. Thomas, G. G. U. Kulkami, "*Nanocrystals: synthesis, properties and applications," in Springer Series in Materials Science*, 95, Berlin Germany, Springer, 2007, pp 1 - 182.

29. S.R. Alvarado, Y. Guo, T.P.A. Ruberu, A. Bakac, J. Vela, J. Phys. Chem. C, 2012 (116) 10382 -10389.

30. D.J. Norris, A.L. Efros, S.C. Erwin, Science, 2008 (319) 1776 - 1779.

31. J.D. Bryan, D.R. Gamelin, Prog. Inorg. Chem., 2005 (54) 47 - 126.

32. C. H. M. Kelly, M. Lein, Phys.Chem.Chem.Phys, 2016 (18) 32448 - 32457.

33. M.V. Roldán, N. Pellegri, O. de Sanctis, Journal of Nanoparticles, 2013 (524150) 1 - 7.

34. H.R. Ghorbani, Orient. J. Chem., 2014 (30) 803 – 806.

35. A. Maringa, T. Nyokong, Electroanalysis, 2014 (26) 1068 – 1077.

36. M. Raja, J. Subha, F.B. Ali, S.H. Ryu, Mater. Manuf. Process., 2008 (23) 782 – 785.

37. Y. Zhang, F. Chen, J. Zhuang, Y. Tang, D. Wang, Y. Wang, A. Dong, N. Ren, Chem. Commun., 2002, 2814 - 2815.

38. J. P. Rereira-Ramos, R. Messina, J. Perichon, J. Electroanal. Chem., 1983 (146) 157 - 169.

39. V.V. Mody, R. Siwale, A. Singh, H.R. Mody, J Pharm Bioall Sci, 2010 (4) 282 - 289.

40. R.L. Johnson, J.P. Wilcoxon, *Metal nanoparticles and nanoalloys*, Volume 3, Oxford, Amsterdam, Elsevier, 2012, pp 1 - 13.

41. Q.L. Zhu, Q. Xu, Chem 1, 2016, 220 - 245.

42. A. Akbari, M. Amini, A. Tarassoli , B. Eftekhari-Sis, N. Ghasemian, E. Jabbari, Nano-Structures & Nano-Objects 2018 (14) 19 - 48.

43. H. Zhang, X. Wang, C. Chen, C. An, Y. Xu, Y. Dong, Q. Zhang, Y. Wang, L. Jiaoa, H. Yuan, Inorg. Chem. Front., 2016 (3) 1048 - 1057.

44. M.M. Najafpour, M. Amini, M. Ashrafi, Int. J. Hydrogen Energy, 2017 (42) 8539 - 8544.

45. Z. Wang, Y. Lee, B. Wu, A. Horst, Y. Kang, Y.J. Tang, D. Chen, Chemosphere 2010 (80) 525 - 529.

46. S. Wang, W. Chen, A. Liu, L. Hong, H. Deng, X. Lin, Chem Phys Chem, 2012 (13) 1199 - 1204.

47. R. El-Sayed, F. Ye, H. Asem, R. Ashour, W. Zheng, M Muhammed, M. Hassan, Biochem. Biophys. Res. Commun., 2017 (491) 15 - 18.

48. M.C. Daniel, D. Astruc, Chem Rev, 2001 (104) 293 - 346.

49. J. Kimling, M. Maier, B. Okenve, V. Kotaidis, H. Ballot, A. Plech, J. Phys. Chem, 2006 (110) 15700 - 15707.

50. W. Haiss, N.T.K. Thahn, J. Aveyard, D.G. Fernig, Anal. Chem, 2007 (79) 4215 - 4221.

51. Y.C. Yeh, B. Creran, V.M. Rotello, Nanoscale, 2012 (4) 1871 - 1880.

52. A. C. Templeton, W. P. Wuelfing and R. W. Murray, Acc. Chem. Res., 2000 (33) 27 - 36.

53. V. Kumar, D. Bano, K. Singh, S. Mohan, V.K. Singh, S.H. Hasan, ACS Sustain. Chem. Eng., 2018 (6) 7662 - 7675.

54. I. Favier, D. Pla, M. Gomez, Chem. Rev. 2020 (120) 1146 - 1183.

55. K.S. Siddiqi, A. Husen, Nanoscale Res. Lett., 2016 (11) 482 (1 - 13).

56. R. Narayanan, M.A. El-Sayed, J. Phys. Chem. B, 2005 (109) 12663 - 12676.

57. H. Dong, Y.C. Chen, C. Feldmann, Green Chem, 2015 (17) 4107 - 4132.

58. J. Zhu, D. Li, H. Chen, X. Yang, L. Lu, X. Wang, Mater. Lett., 2004 (58) 3324 - 3327.

59. J.M. Kshirsagar, R. Shrivastava, P.S. Adwani, Therm. Sci., 2017 (21) 233 - 242.

60. A.Z. Medynska, M. Marchelek, M. Diak, E. Grabowska, Adv. Colloid Interface Sci., 2016 (229) 80 - 107.

61. L. Rout, A. Kumar, R.S. Dhaka, G.N. Reddy, S. Giri, P. Dash, Appl Catal., A, 2017 (538) 107 - 122.

62. H. Mistry, R. Reske, P. Strasser, B.R. Cuenya, Catal. Today, 2017 (288) 30 - 36.

63. M. Blosi, S. Ortelli, A.L. Costa, M. Dondi, A. Lolli, S. Andreoli, P. Benito, S. Albonetti, Materials, 2016 (9) 550 (1 - 25).

64. C. Ray, T. Pal, J. Mater. Chem. A, 2017 (5) 9465 - 9487.

65. J. Liu, W. Wang, T. Shen, Z. Zhao, H. Feng, F. Cui, RSC Adv., 2014 (4) 30624 - 30629.

66. C. Xu, J. Xie, D. Ho, C. Wang, N. Kohler, E. G. Walsh, J. R. Morgan, Y. E. Chin and S. Sun, Angew. Chem., Int. Ed., 2008 (47) 173 - 176.

67. T. Ishida, N. Kinoshita, H. Okatsu, T. Akita, T. Takei, M. Haruta, Angew. Chem., Int. Ed., 2008 (47) 9265 - 9268.

68. M. Shekhar, J. Wang, W. S. Lee, W. D. Williams, S. M. Kim, E. A. Stach, J. T. Miller, W. N. Delgass, F. H. Ribeiro, J. Am. Chem. Soc., 2012 (134) 4700 - 4708.

69. H. Gao, *Encyclopedia of Materials: Science and Technology*, Volume 9, Oxford, UK, Elsevier Science Ltd, 2001, pp 8861 - 8868.

70. A. Guiner, *X-ray Diffraction in Crystals, Imperfect Crystals and Amorphous Bodies*, New York, Courier Corporation, 2013, pp 1 - 5.

71. S. Calvin, S.X. Luo, C. Caragianis-Broadbridge, J.K. Mc Guinness, E. Anderson, A. Lehman, K.H. Wee, S.A. Morrison, L.K. Kurihara, Appl. Phys. Lett., 2005 (87) 233102 (1 - 3).

72. A.V. Malm, J.W. Corbett, Sci. Rep., 2019 (9) 13519 (1 - 11).

73. M. Kaszuba, D. McKnight, M.T. Connah, F. K. McNeil-Watson, U. Nobbmann, J Nanopart Res, 2008 (10) 823 - 829.

74. W. I. Goldburg, Am. J. Phys., 1999 (67) 1152 - 1160.

75. D.B. Williamson, C. B. Carter, *Transmission Electron Microscopy A Textbook for Materials Science*, USA, Springer, 2009, pp 1 - 6.

76. C.L. Jia, M. Lentzen, K. Urban, Microsc. Microanal., 2004 (10) 174 - 184.

77. Z.L. Wang, P. Poncharal, W.A. De Heer, Microsc. Microanal., 2000 (6), 224 - 230.

78. A.S.H, Makhlouf, M. Aliofkhazraei, *Handbook of Materials Failure Analysis with Cases Studies from the Oil and Gas Industries,* Oxford UK, Elsevier, 2016, pp 42 - 49.

79. R. Breslow, Science, 1982 (218) 532 - 537.

80. X. Wang, W. Guo, Y. Hu, J. Wu, H. Wei, *Nanozymes: Next Wave of Artificial Enzymes*, China, Springer, 2016, pp 1 - 2.

81. J.B. van Beilen, Z. Li, Curr. Opin. Biotechnol. 2002 (13) 338 - 344.

82. Z. Findrik, D. Visic-Racki, Chem. Biochem. Eng. Q., 2009 (23) 545 - 553.

83. R. Kumar, S. Xiavour, S. Latha, V. Kumar, J Chromatograph Separat Techniq 5, 2014 (211) 2157 - 7064.

84. N.C. Veitch, Phytochemistry 2004 (65) 249 - 259.

85. W. He, W. Wamer, Q. Xia, J. Yin, P.P. Fu, J. Environ. Sci. Health C, 2014 (32) 186 - 211.

86. P. D. Josephy, T. Eling, R.P. Mason, J. Biol. Chem., 1982 (257) 3669 - 4675.

87. G.D. Yadav, D.B. Magadum, (2017) "*Kinetic Modelling of Enzyme Catalyzed Biotransformation Involving Activations and Inhibitions*" *in*. M. Senturk (Ed), *Enzyme Inhibitors and Activators*, Croatia, pp 75 - 86.

88. E.G. Malygin, S. Hattman, J. Theor. Biol., 2006 (242) 627 - 633.

89. S. Schnell, FEBS Journal, 2014 (281) 464 - 472.

90. N.S. Ridhuan, K.A. Razak, Z. Lockman, Sci. Rep, 2018 (8) 13722 (1 - 12).

91. J. Wang, Electroanalysis, 2001 (13) 983 - 988.

92. B. Lim, Y.P. Kim, Adv Biochem Eng Biotechnol, 2014 (140) 203 - 219.

93. T. Yu-Rong, Z. Yu, L.I.U. Rui, S.U. Ying-Ying, L.U. Yi , Chin. J. Anal. Chem. 2013 (4) 330 - 336.

94. L. Gao, J. Zhuang, L. Nie, J. Zhang, Y. Zhang, N. Gu, T. Wang, J. Feng, D. Yang, S. Perrett, X. Yang, Nat. Nanotechnol., 2007 (2) 577 - 583.

95. Y. Chen, H. Cao, W. Shi, H. Liu, Y. Huang, Chem. Commun., 2013 (49) 5013 - 5015.

96. L. Su, J. Feng, X. Zhou, C. Ren, H. Li, X Chen, Anal. Chem. 2012 (84) 5753 - 5758.

97. J. Mu, Y. Wang, M. Zhao, L. Zhang, Chem. Commun. 2012 (48) 2540 - 2542.

98. H. Zhao, Y. Dong, P. Jiang, G. Wang, J. Zhang, ACS Appl. Mater. Interfaces 2015 (7) 6451 - 6461.

99. Q. Liu, Y. Yanga, X. Lv, Y. Dinga, Y. Zhanga, J. Jinga, C. Xu, Sens. Actuators B., 2017 (240) 726 - 734.

100. G.W. Wu, Y.M. Shen, X.Q. Shi, H.H. Deng, X.Q. Zheng, H.P. Peng, A.L. Liu, X.H. Xia, W Chen, Anal Chim Acta, 2017 (971) 88 - 96.

101. G. Darabdhara, P.K. Boruah, M.R. Das, Microchim Acta, 2019 (186) 11939 (1 - 10).

102. F. Yuan, H. Zhao, H. Zang, F. Ye, X. Quan, ACS Appl Mater & Interf , 2016 (8) 9855 - 9864.

103. Y. Pang, Z. Huang, Y. Yang, Y. Long, H. Zhen, Spectrochim Acta A, 2018 (189) 510 - 515.

104. S. Mvango, P. Mashazi, Mater. Sci. Eng., C, 2019 (96) 814 - 823.

105. O. Adeniyi, S. Sicwetsha, P. Mashazi, ACS Appl. Mater. Interfaces, 2020 (12) 1973 - 1987.

106. S. Cai, Q. Han, C. Qi, Z. Lian, X. Jia, R. Yang, C. Wang, Nanoscale, 2016 (8) 3685 - 3693.

107. H.V. Tran, T.V. Nguyen, N.D. Nguyen, B. Piro, C.D. Huynh, Microchim Acta, 2018 (185) 270 - 80.

108. S. Cherevko, C.H. Chung, Sens. Actuators B Chem., 2009 (142) 216 - 223.

109. W. Chen, J. Chen, Y.B. Feng, L. Hong, Q.Y. Chen, L.F. Wu, X.H. Lin, X.H. Xia, Analyst., 2012 (137) 1706 - 1712.

CHAPTER 2

SYNTHESIS, CHARACTERIZATION AND PEROXIDASE-LIKE ACTIVITY OF COPPER OXIDE ANISOTROPIC NANOPARTICLES

Synthesis, Characterization and Peroxidase-like Activity of Copper Oxide Nanoparticles

Simbongile Sicwetsha, Sindisiwe Mvango, Philani Mashazi

Department of Chemistry, Rhodes University, P.O. Box 94, Makhanda, 6140, South Africa

Abstract

The spherical CuO nanoparticles and CuO nanorods were prepared using the sol-gel method. The successful preparation of the spherical CuO nanoparticles and CuO nanorods was confirmed using UV-vis, DLS (zeta potential), XRD, TEM and EDS. The nanoparticles were found to possess intrinsic peroxidase-like activity. The peroxidase-like activity was investigated by the catalytic oxidation of a chromogenic substrate (TMB) in the presence of H_2O_2. The investigation of the steady-state kinetic parameters showed that the peroxidase-like activity of the nanomaterials followed the Michaelis-Menten kinetics behaviour. The production of reactive oxygen species (ROS) was investigated and detected using 1,3-diphenylisobenzofuran (DPBF). The spherical CuO nanoparticles and CuO nanorods were used in biosensing for the colorimetric detection of glucose. The limit of detection (LOD) and the limit of quantification (LOQ) for spherical CuO nanoparticles was 0.73 μM and 2.42 μM, respectively. The LOD and LOQ for CuO nanorods was 0.13 μM and 0.42 μM, respectively.

KEYWORDS: *Spherical CuO nanoparticles, CuO nanorods, peroxidase-like activity, glucose detection.*

2.1 Introduction

Metal oxide nanoparticles have attracted an increasing attention from researchers due to their interesting properties. The properties of metal oxide nanoparticles include large surface-to-volume ratio, increased reactivity, good electronic and optical properties.[1-3] Transition metal oxides are a significant category of semiconductors that find applications in catalysis, magnetic storage, electronics and solar energy transformation.[1,4,5] Copper oxide nanoparticles have been studied because they are stable, robust and have a longer shelf life.[6] Copper oxide is a p-type semiconductor with a narrow bandgap. The properties of copper oxide include high stability, photovoltaic properties, high thermal conductivity and antimicrobial activity.[7] The interesting properties of copper oxide have resulted in the applications of these interesting systems in active catalysis, gas sensing, high efficiency thermal conducting materials, magnetic recording media and solar cell applications.[7-12] A variety of nanomaterials have been reported to demonstrate peroxidase and catalase-like activities. Typical examples of such nanomaterials include γ-iron oxide nanoparticles and apo-ferritin-coated platinum nanoparticles.[13-15] Nanomaterial based artificial enzymes have also been used in colorimetric detection due to their tunable catalytic activities, easy storage and high stability in harsh environmental conditions.[16] Gold[17], silver[18] and platinum[19] nanoparticles have been used in biosensing for the colorimetric detection of glucose. In this study, we investigate the preparation and characterization of spherical CuO nanoparticles and CuO nanorods and further investigate their potential as peroxidase mimics, that is, imitating the catalytic activity of HRP.

2.2 Experimental

2.2.1 Reagents and (apparatus)

Copper acetate $Cu(COOCH_3)_2$, 3,3',5,5'-tetramethylbenzidine (TMB), glacial acetic acid (CH_3COOH), 1,3-diphenylisobenzofuran (DPBF), D-glucose powder, glucose oxidase (GOx, EC 1.1.3.4. from Aspergillus niger, Type VII) were purchased from Sigma-Aldrich. Potassium hydroxide pellets (KOH), sodium acetate anhydrous ($C_2H_3NaO_2$), and potassium dihydrogen orthophosphate (KH_2PO_4) were purchased from Merck. Sodium hydroxide pellets (NaOH), absolute ethanol (C_2H_5OH), methanol (CH_3OH), hydrogen peroxide (H_2O_2), 50%, C.P, hydrochloric acid (HCl), 32 %, C.P, and dimethyl sulfoxide (DMSO) were purchased from B&M Scientific. All the reagents were of analytical grade and were used as received from the suppliers. Ultrapure water with the resistivity of 18 MΩ.cm obtained from a Milli-Q water system (Millipore Corp, Bedford, MA, USA) was used for the preparation of standard solutions.

UV-visible measurements were conducted on a ThermoScientific, Multiskan Sky w Cuvette & Touch Screen, 100 – 240 V, Belgium . Zeta potential measurements were carried out on a Malvern Zetasizer Nano-ZS90 series equipped with a 633 nm He/Ne laser. A disposable folded capillary cell (DTS 1060) was used for data collection. TEM images were taken from a Zeiss Libra 120 TEM operating at 80 kV. The nanoparticles were dissolved in water and dropped onto a carbon-coated copper grid and allowed to dry at room temperature overnight before data collection. The EDS spectra were obtained from INCA PENTA FET coupled with VGA TESCAM at 20 kV acceleration voltage. X-ray powder diffraction (XRD) patterns were recorded on a Bruker D8 Discover equipped with a Lynx Eye detector, using Cu-Ka radiation (1.5405 Å, nickel filter). The data were collected within 2θ range of 10° to 100°. The samples were placed on a silicon wafer slide.

2.3 Preparation of nanomaterials

2.3.1 Preparation of spherical CuO nanoparticles

Spherical copper oxide nanoparticles were prepared following the sol-gel method that has been previously reported, with slight modifications.[20] Briefly, 75 mL of 20 mM copper acetate solution was blended with 250 µL glacial acetic acid in a round-bottom flask. The reaction was heated to reflux with continuous stirring. A 10 mL solution of sodium hydroxide (1.50 M) was added quickly. A black precipitate immediately formed. The reaction was allowed to react for 30 minutes. The precipitate was centrifuged, washed three times with ethanol and air dried in room temperature.

2.3.2 Preparation of copper oxide nanorods

Similar procedure as for spherical copper oxide nanoparticles was used for the preparation of copper oxide nanorods. Briefly, 75 mL of 80 mM copper acetate solution was blended with 1.0 mL glacial acetic acid in a round-bottom flask. The reaction was heated to reflux with continuous stirring. A 10 mL solution of sodium hydroxide (6 M) was added quickly. A black precipitate formed immediately. The reaction was allowed to react for 30 minutes. The precipitate was centrifuged, washed three times with ethanol and air dried in room temperature.

2.4 Peroxidase-like activity

The investigation of the peroxidase-like activity of spherical copper oxide nanoparticles and copper oxide nanorods was conducted at room temperature using 3,3',5,5'-tetramethylbenzidine (TMB) in the presence of hydrogen peroxide (H_2O_2). Briefly, hydrogen peroxide (50 µL, 100 mM), TMB (50 µL, 25 mM), and different nanoparticles (10 µL, 6.0 $\mu g.mL^{-1}$) were added to 0.20 M acetate buffer solution (at the pH where IEP is zero for different copper oxide nanoparticles) in a cuvette. After adding the nanoparticles to the acetate buffer

solution containing TMB and hydrogen peroxide, the evolution of a blue colour was observed and measured using UV-vis spectrophotometer in the wavelength range 300 – 800 nm.

2.5 Evaluating reactive oxygen species (ROS) generation using DPBF (radical quencher)

The production of reactive oxygen species (ROS) was investigated using 1,3-diphenylisobenzofuran (DPBF) as a radical scavenger. The generation of ROS was investigated using the solution containing DPBF (50 µL, 0.25 mM), and hydrogen peroxide (75 µL, 100 mM) in the presence of (50 µL, 6.0 $\mu g.mL^{-1}$) copper oxide nanoparticles. UV-vis spectroscopy was used to monitor the decreasing absorption band at 430 nm for DPBF. The absorbance measurements were taken at one-minute interval for 20 minutes.

2.6 Glucose detection using the prepared copper oxide nanoparticles

Glucose detection using the spherical copper oxide nanoparticles and copper oxide nanorods was conducted by the enzymatic reaction between D-glucose and glucose oxidase (GOx) to yield D-gluconolactone and hydrogen peroxide. Briefly, GOx (50 µL, 2.0 $\mu g.mL^{-1}$) was added to the solution of D-glucose (25 µL, varied concentration) in phosphate buffer (75 µL, pH 7) and incubated at 35 °C for 45 minutes. After 45 minutes, a 50 µL solution of 400 µL (6.0 $\mu g.mL^{-1}$) of copper oxide nanoparticles and TMB (100 µL, 2.0 mM) in acetate buffer (1.0 ml, 0.20 M) at optimum pH was added to the enzyme-glucose solution at 35 °C.

2.7 Results and Discussion

2.7.1 Synthesis and characterization of spherical CuO nanoparticles and CuO nanorods

The preparation of spherical CuO nanoparticles and CuO nanorods was achieved using the sol-gel method following the chemical reduction method.[20] This method includes the heating of the reaction to boiling and this is essential because it allows for the decomposition of copper hydroxide ($Cu(OH)_2$) to produce copper oxide (CuO).[21] The sol-gel method has the potential of producing nanoparticles with uniform size and shape[22] , hence the choice for the studied work. In addition, the sol-gel method was used because it is cheap and eco-friendly and it affords controlled consolidation, shape modulation, modelling of the nanostructures and low operation temperatures.[22,23] The preparation of copper oxide nanoparticles resulted in the formation of a black precipitate. This change in colour was a visual confirmation of the formation of nanoparticles and the decomposition of $Cu(OH)_2$ to form CuO nanoparticles as discussed.[21] The resulting black precipitate was studied using different characterization techniques.

UV-vis spectroscopy was used to confirm the formation and confirm the optical properties of spherical CuO nanoparticles and CuO nanorods. **Figure 2.1(a)** shows the UV-vis spectra of (i) spherical CuO nanoparticles (red) and (ii) CuO nanorods (green). The UV-vis spectrum of spherical CuO nanoparticles showed an absorption band around 300 nm. The absorption band is due to the surface plasmon resonance (SPR) band of the nanoparticles. CuO spherical nanoparticles with the SPR band at 280 nm have been previously reported by Chen and co-workers.[24] The UV-vis spectrum of CuO nanorods shows a broad and red shifted SPR band around 350 nm. The broadened and red-shifted SPR band can be attributed to the change in nanoparticle morphology (size and shape). Rod-like nanoparticles are characterized by their

transverse and longitudinal optical properties. This is however not visible at CuO nanorods and due to the nature of the material composition containing copper oxygen to form copper oxide crystal structure and not pure metallic crystal structure usually observed for noble metal nanoparticles. **Figure 2.1(b)** shows the plot of zeta potential (mV) versus pH for (i) spherical CuO nanoparticles (red) and (ii) CuO nanorods (green). The spherical CuO nanoparticles showed positive zeta potential values at pH below 3. At pH values above 3, that is between pH 4 - 10, negative zeta potential values were observed. The CuO nanorods showed positive zeta potential only at pH 2. Negative zeta potential were obtained when the pH was further adjusted from pH 3 - 10. The negative zeta potential are due to the negatively charged hydroxyl groups (-OH) on the surface of spherical CuO nanoparticles and CuO nanorods. The isoelectric point (IEP) was obtained at pH 3.5 for spherical CuO nanoprticles and pH 2.5 for CuO nanorods. CuO nanoparticles are acidic catalysts due to the IEP which is in acidic pH. The spherical CuO nanoparticles and CuO nanorods showed negative zeta potential at pH 7 (neutral pH). The spherical CuO nanoparticles and CuO nanorods were unstable in the studied pH range (pH 2 - 10). **Figure 2.1(c)** shows the X-ray diffraction patterns of (i) spherical CuO nanoparticles (red) and (ii) CuO nanorods (green). The spherical CuO nanoparticles and CuO nanorods showed identical diffraction patterns. The X-ray diffractograms for spherical CuO nanoparticles and CuO nanorods were observed at 32.6, 35.6, 38.8, 48.9, 53.3, 57.9, 61.5, 65.9, 67.5, 71.9, 74.5° corresponding to (110), (-111), (111), (-202), (020), (202), (-113), (022), (311), (004) Miller indices. The XRD patterns of spherical CuO nanoparticles and CuO nanorods were identical to the single phase CuO with a monoclinic structure with lattice constants, a = 4.67970, b = 3.43140, c = 5.13620, $\alpha = 90.00$, $\beta = 99.26$ and $\gamma = 90.00°$ from the standard card JCPDS 72-0629. The spherical CuO nanoparticles and CuO nanorods showed high phase purity since there were no additional peaks of impurities observed in the XRD patterns.

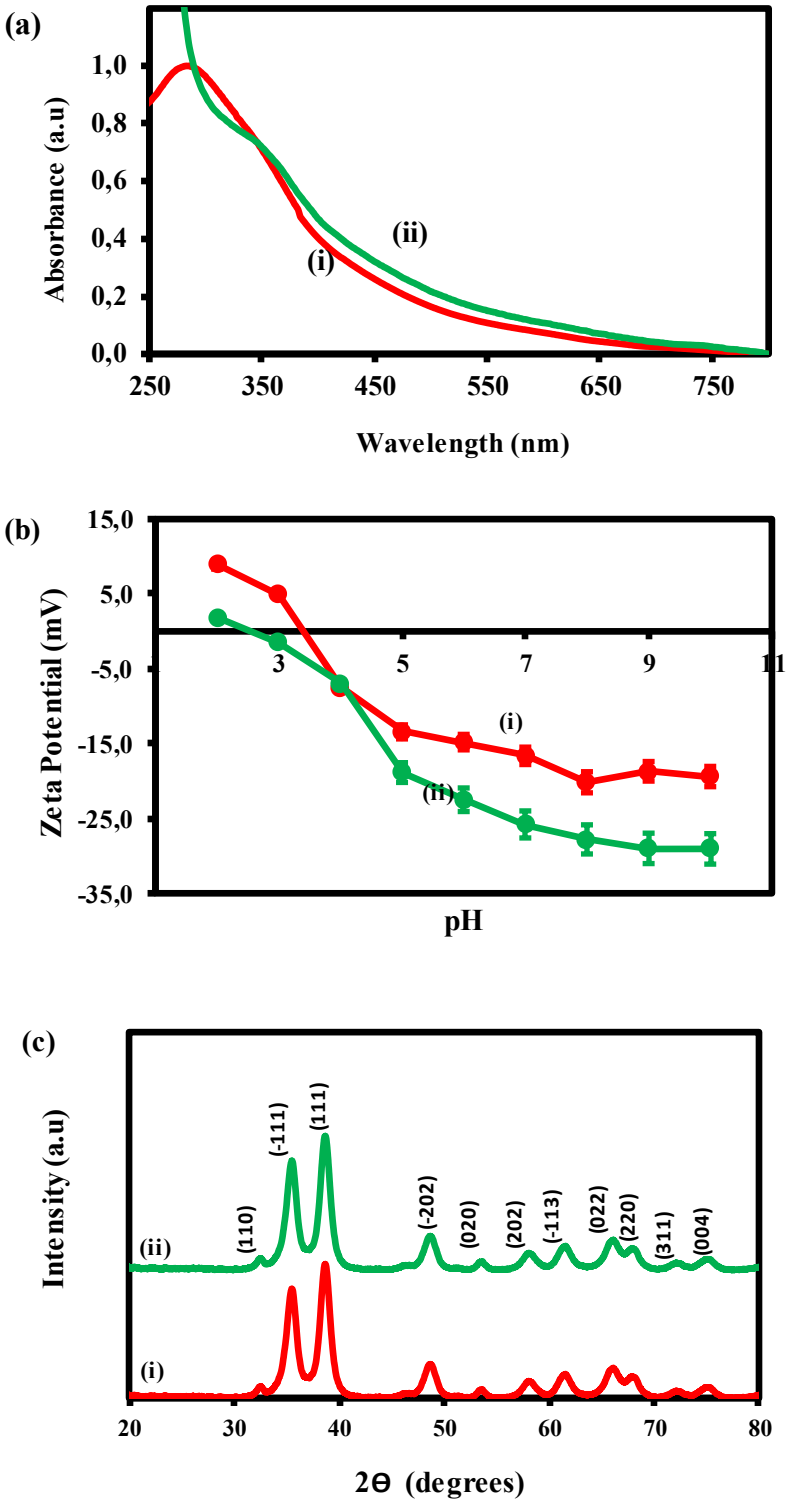

Figure 2.1: (a) UV-vis absorption spectra, (b) Zeta potential vs pH, and (c) X-ray diffraction patterns for (i) spherical CuO nanoparticles and (ii) CuO nanorods.

Transmission electron microscope (TEM) was used to analyze the detailed morphology of the prepared spherical CuO nanoparticles and CuO nanorods. **Figure 2.2** shows TEM micrographs with their corresponding size distribution histograms for (a) spherical CuO nanoparticles and (b) CuO nanorods. The TEM image of spherical CuO nanoparticles revealed that the product comprised spherical particles with the average particle size found to be 8.0 ± 2.0 nm. The TEM image of CuO nanorods showed rod-like shaped structures with the length of 40.0 ± 5.6 nm and the width of 11.0 ± 4.5 nm. The TEM images of both spherical CuO nanoparticles and CuO nanorods showed well-dispersed nanoparticles.

Figure 2.2 also shows the EDS spectra of (c) spherical CuO nanoparticles and (d) CuO nanorods. The EDS spectra of both spherical CuO nanoparticles and CuO nanorods showed the presence of Cu, O and C. The Cu and O were expected in the CuO nanoparticles. The small C peak was observed, and this was due to the acetate used in the preparation. The C was very small and almost negligible to the concentrations of Cu and O for both spherical and rod-like nanoparticles.

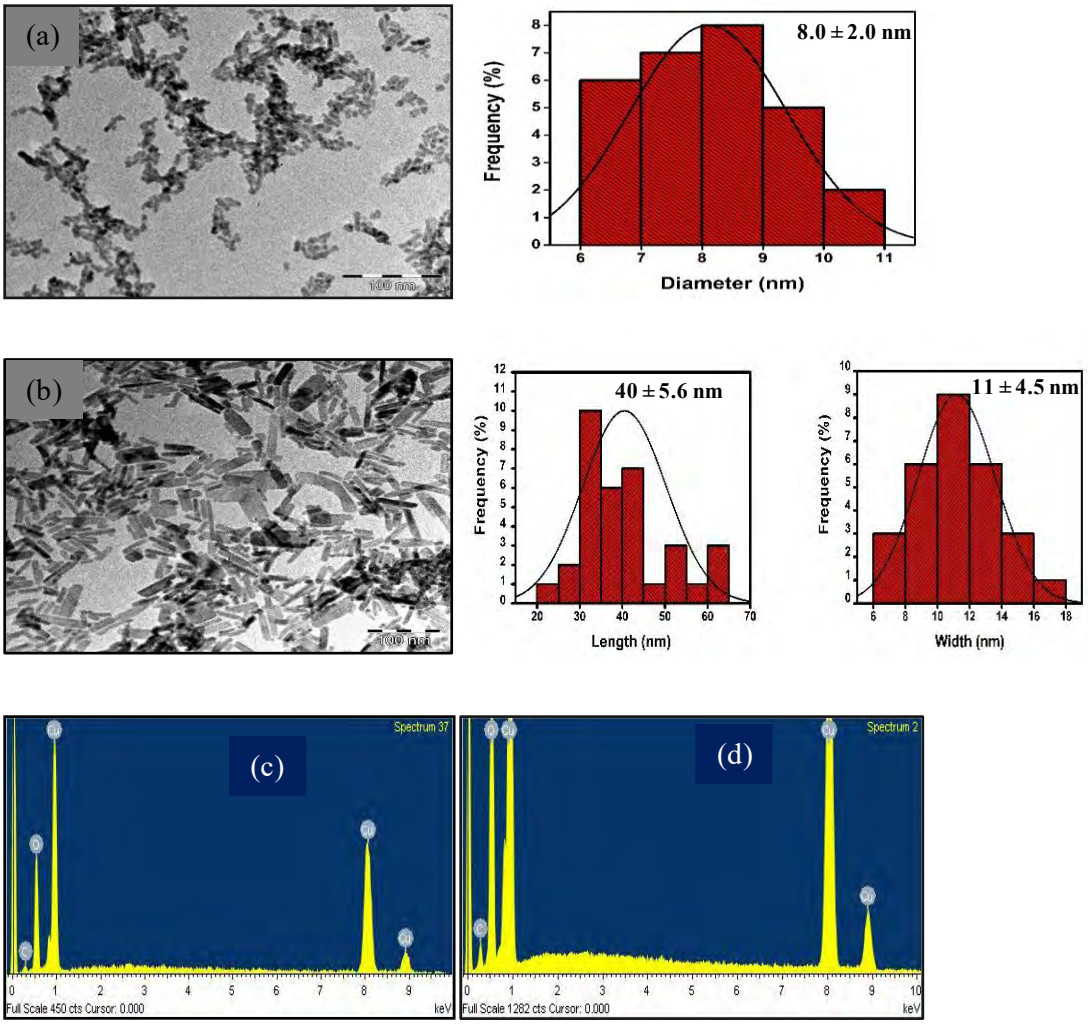

Figure 2.2: TEM micrographs with their corresponding size distribution histograms for (a) spherical CuO nanoparticles and (b) CuO nanorods. EDS spectra of (c) spherical CuO nanoparticles and (d) CuO nanorods.

2.7.2 Peroxidase-like activity of spherical CuO nanoparticles and CuO nanorods

Copper oxide nanoparticles have been studied to demonstrate peroxidase-like activity which makes them suitable for applications in colorimetric biosensing. To investigate the peroxidase-like activity of spherical CuO nanoparticles and CuO nanorods, the catalytic oxidation of a chromogenic substrate 3,3',5,5'-tetramethylbenzidine (TMB) in the presence of H_2O_2 was investigated. **Figure 2.3** shows the UV-vis absorption spectra of (i) nanoparticles + H_2O_2 alone (blue), (ii) nanoparticles + TMB alone (black), (iii) CuONRs + H_2O_2 + TMB (green), (iv) spherical CuONPs + H_2O_2 + TMB (red). (b) Images of (i) nanoparticles + H_2O_2 (100 mM), (ii) nanoparticles + TMB (25 mM), and (iii) nanoparticles + H_2O_2 (100 mM) + TMB (25 mM). In **Figure 2.3(a)**, the UV-vis spectra of CuO nanorods + H_2O_2 + TMB (green), and spherical CuO NPs + H_2O_2 + TMB (red) exhibited the three absorption bands at 370, 450 and 652 nm. The spherical CuO nanoparticles and CuO nanorods in the presence of both TMB and H_2O_2 showed the emergence of a blue coloured species due to the oxidation of 3,3',5,5'-tetramethylbenzidine (TMB) to form 3,3',5,5'-tetramethylbenzidine diimine (TMBDI). The colour formation was observed in solutions as shown in **Figure 2.3(b)**. The evolution of the blue coloured TMBDI and the emergence of the absorption bands at 370, 450 and 652 nm confirm that spherical CuO nanoparticles and CuONRs exhibit peroxidase-like activity.

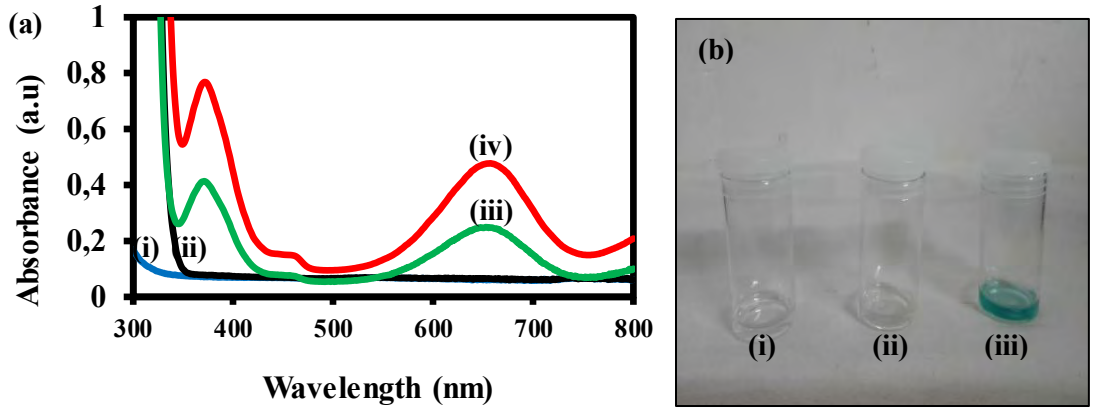

Figure 2.3: (a) UV-vis absorption spectra of (i) nanoparticles + H_2O_2 alone (blue), (ii) nanoparticles + TMB alone (black), (iii) CuONRs + H_2O_2 + TMB (green), (iv) spherical CuONPs + H_2O_2 + TMB (red). (b) Images of (i) nanoparticles + H_2O_2 (100 mM), (ii) nanoparticles + TMB (25 mM), and (iii) nanoparticles + H_2O_2 (100 mM) + TMB (25 mM). (nanoparticles refers to spherical CuONPs or CuONRs).

2.7.3 Conditions affecting the peroxidase-like of spherical CuONPs and CuONRs

The environmental conditions that have been described to influence the peroxidase-like activity of nanoparticles are pH, temperature and enzyme substrate concentration. The effect of different environmental conditions on peroxidase-like activity of CuO nanoparticles was investigated and the enzymatic absorption band at 652 nm was monitored. **Figure 2.4** shows the effect of (a) reaction time, (b) pH, (c) varying H_2O_2 concentration, and (d) temperature on peroxidase-like activity of spherical CuONPs (red) and CuONRs (green). In **Figure 2.4(a)**, the effect of reaction time was investigated by increasing the reaction time from 0 - 20 minutes. The peroxidase-like activity of spherical CuO nanoparticles and CuO nanorods increased linearly with an increase in the reaction time. In **Figure 2.4(b)**, the effect of pH was investigated by adjusting the pH from 3 - 9. The maximum peroxidase-like activity was observed at pH 5 for both spherical CuO nanoparticles and CuO nanorods. In **Figure 2.4(c)**, the effect of varying H_2O_2 concentration was investigated. The concentration of H_2O_2 was varied from 0 - 40 mM while the concentration of TMB was kept constant. The peroxidase-

like activity of spherical CuO nanoparticles and CuO nanorods increased with an increase in H_2O_2 concentration. In **Figure 2.4(d)**, the effect of increasing the temperature from 20 - 40 °C was studied. The spherical CuO nanoparticles and CuO nanorods displayed an increase in peroxidase-like activity as the temperature was increased from 20 - 40 °C. Therefore, for spherical CuO nanoparticles and CuO nanorods the optimum reaction conditions were 20 minutes, pH 5, 40 mM H_2O_2 concentration and 40 °C for a maximum UV-vis absorption of TMBDI.

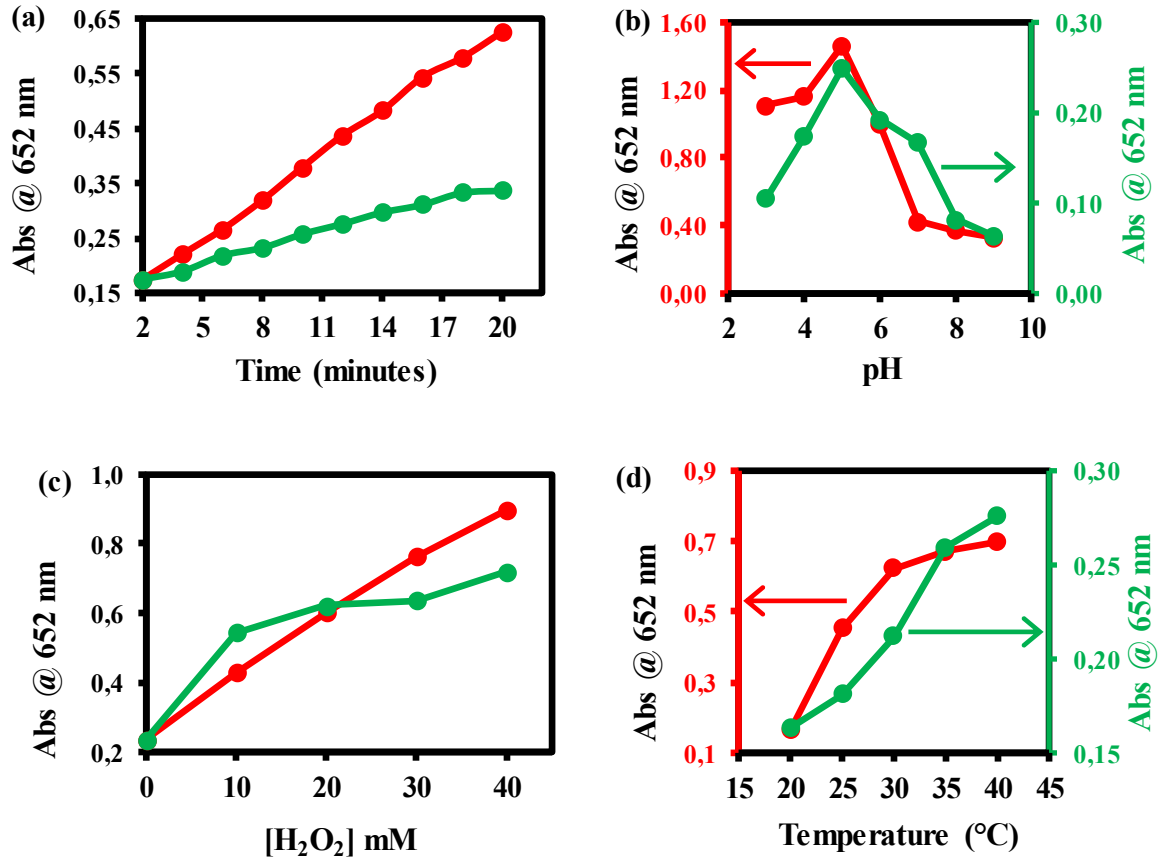

Figure 2.4: Effect of (a) reaction time, (b) pH, (c) changing H_2O_2 concentration, and (d) temperature on peroxidase-like activity of spherical CuO nanoparticles (red) and CuO nanorods (green).

2.7.4 Steady-state kinetics of spherical CuONPs and CuONRs

The steady-state kinetic parameters were determined to evaluate the mechanism of the peroxidase-like activity of spherical CuONPs and CuONRs. The Michaelis-Menten and Lineweaver-Burk (double reciprocal) models were used to investigate the steady-state kinetic parameters of spherical CuO nanoparticles and CuO nanorods. The steady-state kinetic parameters were obtained by changing one substrate concentration (H_2O_2 or TMB) while keeping the other substrate constant. The Michaelis-Menten constant (K_m) and the maximum velocity (V_{max}) were obtained by fitting the data obtained from the plot of initial velocity (V_o) versus substrate concentration [S] to the Lineweaver-Burk double reciprocal plot. **Figure 2.5** shows a plot of initial velocity (V_o) versus varied [H_2O_2] concentration at a fixed [TMB] concentration, and their corresponding Lineweaver-Burk double reciprocal plots for (a) spherical CuONPs and (b) CuONRs. As illustrated in **Figure 2.5**, the peroxidase-like activity of spherical CuONPs and CuONRs follows the Michaelis-Menten behaviour. Derived from the Lineweaver-Burk double reciprocal plots, the K_m value for spherical CuONPs was 1.12 mM. The K_m value for CuONRs was 40.04 mM. The K_m value for spherical CuO nanoparticles was lower than for HRP (3.70 mM).[25] These results indicate that the spherical CuONPs showed a stronger binding affinity than CuONRs towards H_2O_2 substrate. The maximum velocity (V_{max}) was 8.62 x 10^{-9} $M.s^{-1}$ and 1.06 x 10^{-9} $M.s^{-1}$ for spherical CuONPs and CuONRs respectively.

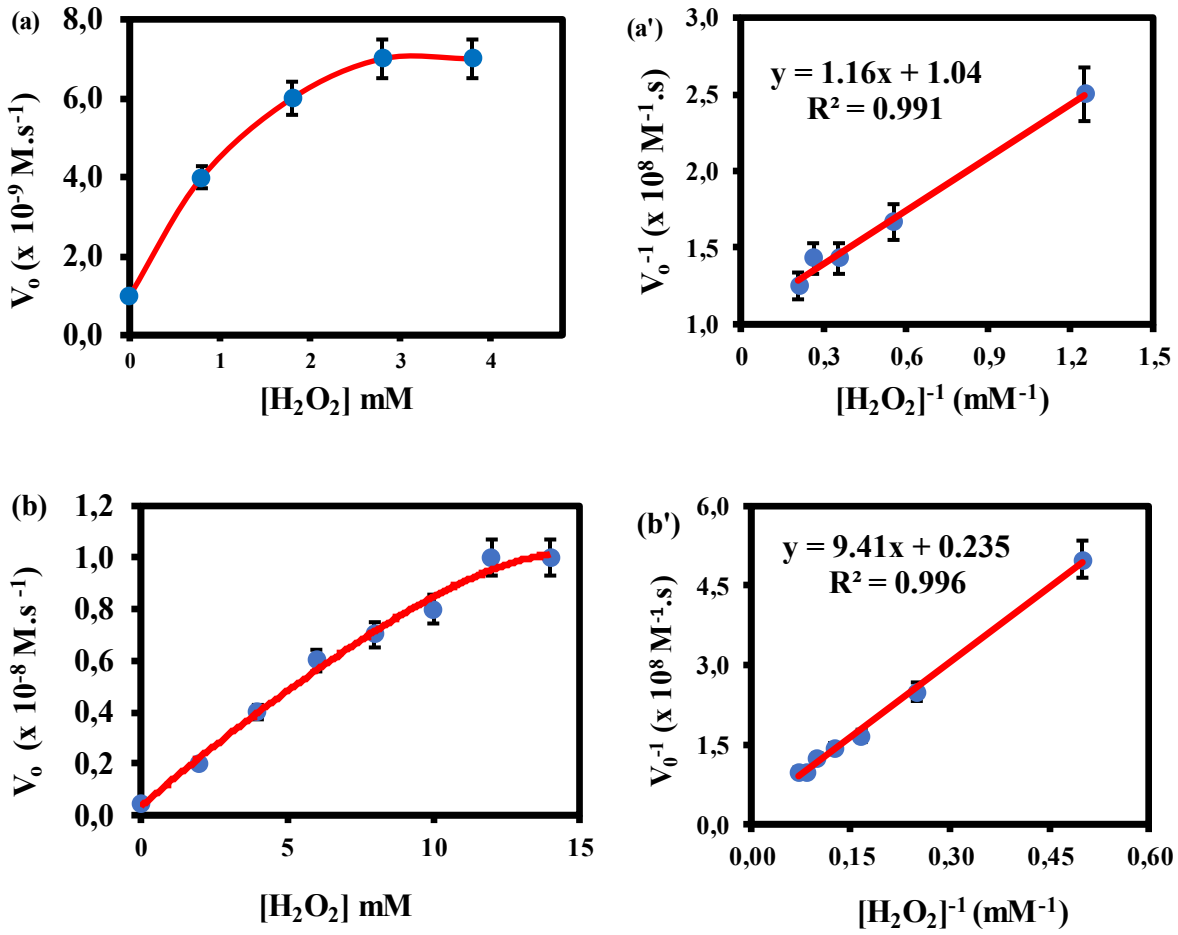

Figure 2.5: The steady-state kinetic plots of varied H_2O_2 concentration at a fixed TMB concentration and their corresponding double reciprocal plots for (a) spherical CuONPs and (b) CuONRs.

Figure 2.6 shows the steady-state kinetic parameters, plot of initial velocity (V_o) versus substrate concentration [TMB], and their corresponding double reciprocal plots for (a) spherical CuONPs and (b) CuONRs. The concentration of TMB was varied while the H_2O_2 concentration was kept constant for spherical CuONPs and CuONRs. As illustrated in **Figure 2.6**, the peroxidase-like activity of spherical CuONPs and CuONRs follows the Michaelis-Menten behaviour. At lower TMB concentrations (0 - 4.0 mM), the initial velocity (V_o) increased linearly with increasing concentration of TMB for both spherical CuONPs and CuONRs. The K_m and V_{max} were derived from the slope and intercepts of the Lineweaver-Burk (double reciprocal) plots. When TMB was used as a substrate, the K_m values were 1.14 mM and 2.91 mM for spherical CuONPs and CuONRs respectively. The K_m values of both spherical CuONPs and CuONRs were higher than for HRP (0.434 mM).[25] The spherical CuONPs showed a stronger binding affinity for both substrates H_2O_2 (K_m = 1.11 mM) and TMB (K_m = 1.14 mM). These results suggest that the spherical CuONPs has better catalytic activity (peroxidase-like activity) than the CuONRs. The maximum velocity (V_{max}) was 7.35 x 10^{-8} $M.s^{-1}$ and 5.52 x 10^{-9} $M.s^{-1}$ for spherical CuONPs and CuONRs respectively.

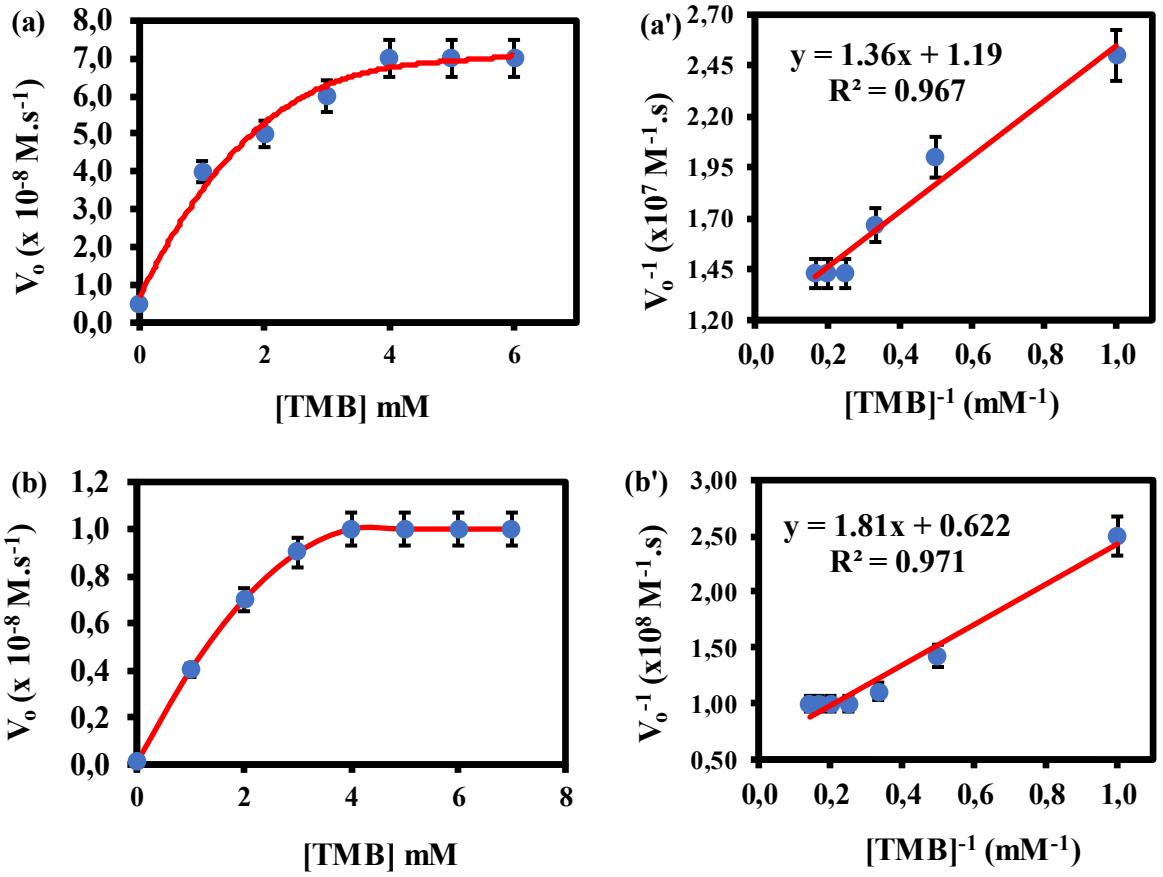

Figure 2.6: The steady-state kinetic plots of varied TMB concentration at a fixed H_2O_2 concentration and their corresponding double reciprocal plots for (a) spherical CuONPs and (b) CuONRs.

2.7.5 The production of reactive oxygen species monitored using DBPF

The production of reactive oxygen radical species (ROS) was investigated and detected using 1,3-diphenylisobenzofuran (DPBF). DPBF is a fluorescent molecular probe that is efficient for the detection of reactive oxygen species (ROS).[26] The fluorescence response of DPBF is not quenched by reacting with reactive oxygen radical species.[26,27] DPBF was used due to its selectivity and sensitivity towards reactive oxygen species (ROS).[26] The spherical CuONPs and CuONRs interact with H_2O_2 to produce reactive oxygen radical species ($OH^{\bullet}$, $HOO^{\bullet}$, $^{\bullet}O_2$). The degradation of DPBF was investigated using UV-vis spectroscopy and the DPBF absorption band at 430 nm was monitored. The rate of degradation of DPBF is proportional to the amount of ROS generated. **Figure 2.7** shows the rate of degradation plots for DPBF + H_2O_2 (green), DPBF + nanoparticles (red) and DPBF + H_2O_2 + nanoparticles (purple) for (a) spherical CuONPs and (b) CuONRs. There was no change in the DPBF absorption band at 430 nm for DPBF + H_2O_2. A decline in DPBF absorption band at 430 nm was observed for DPBF + nanoparticles alone. An increase in the rate of degradation of DPBF monitored by its absorption band at 430 nm was observed for spherical CuONPs and CuONRs in the presence H_2O_2. The rate of degradation of DPBF was obtained from the slope of the linear plot. The rate of degradation of DPBF was 4.91×10^{-2} a.u./min and 5.99×10^{-2} a.u./min for spherical CuONPs and CuONRs respectively. The rate of degradation of DPBF were higher for DPBF + H_2O_2 + nanoparticles than when compared to DPBF + nanoparticles which was 4.7×10^{-3} a.u./min for spherical CuONPs and 8.7×10^{-3} a.u./min for CuONRs. The degradation rate for DPBF in the presence of H_2O_2 alone was 5.0×10^{-4} a.u./min. The observed increase in degradation rate especially when nanoparticles were in the presence of H_2O_2 and DPBF were due to the generation of reactive oxygen radical species by the nanoparticles and oxidizing DPBF.

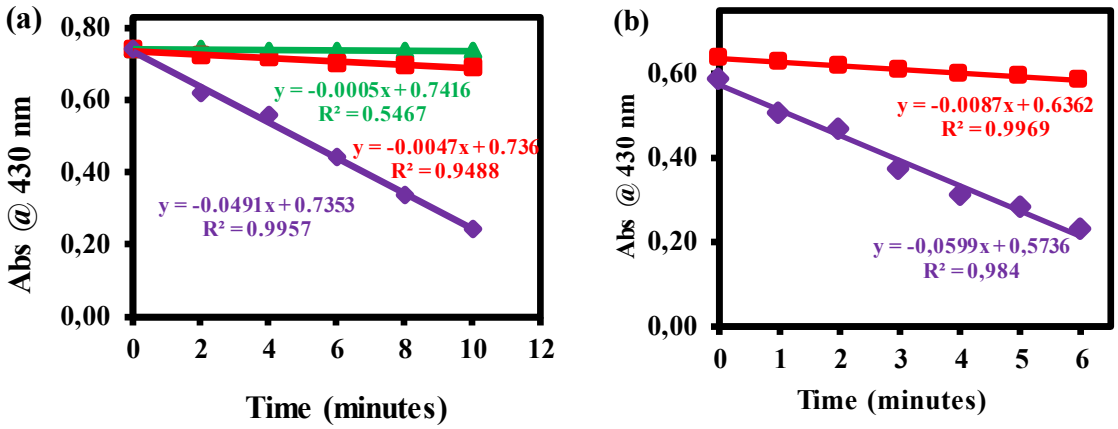

Figure 2.7: The rate of degradation plots for, DPBF + H_2O_2 alone (green), DPBF + nanoparticles alone (red), and DPBF + H_2O_2 + nanoparticles (purple) for (a) spherical CuONPs and (b) CuONRs.

2.7.6 Glucose detection using spherical CuONPs and CuONRs

Spherical CuONPs and CuONRs were investigated for their capability as peroxidase mimetics in the colorimetric detection of glucose. The glucose detection was conducted using TMB as a chromogenic substrate. Glucose oxidase (GO_x) is widely used in the biosensors design for detecting glucose because of its exceptional selectivity and sensitivity towards their substrate (glucose). The H_2O_2 is produced from the oxidation of GO_x and D-glucose. Nanoparticles with intrinsic peroxidase-like activity reduce H_2O_2 produced by glucose oxidase enzyme to reactive oxygen radical species. ROS oxidizes TMB to form TMBDI (the blue coloured product that can be quantitatively determined using spectrophotometry). The intensity of the TMBDI is related to the concentration of D-glucose, hence its determination. The TMBDI is distinguished by the SPR band at 652 nm in the UV-vis spectrum. **Figure 2.8** shows the UV-vis spectra and the corresponding plots of monitored absorbance at 652 nm versus varied concentration D-glucose for (a) spherical CuONPs and (b) CuONRs. The concentration of D-glucose was varied whilst those of GOx, nanoparticles and TMB were kept the same. For both spherical CuONPs and CuONRs, an increase in the TMBDI absorption at 652 nm was observed

as the concentration of glucose increased. The linear regression equation for spherical CuONPs was, Abs = 3.0 x 10^{-3} [D-glucose] + 0.1130, R^2 = 0.99. The linear regression equation for CuONRs was 3.50 x 10^{-3} [D-glucose] + 0.0740 with R^2 = 0.99. The limit of detection (LOD) and the limit of quantification (LOQ) for spherical CuO nanoparticles was calculated and found to be 0.73 µM and 2.42 µM respectively. The LOD and LOQ for CuONRs were 0.13 µM and 0.42 µM respectively. **Table 2.1** shows the comparison of the performance of different nanomaterials towards glucose detection.

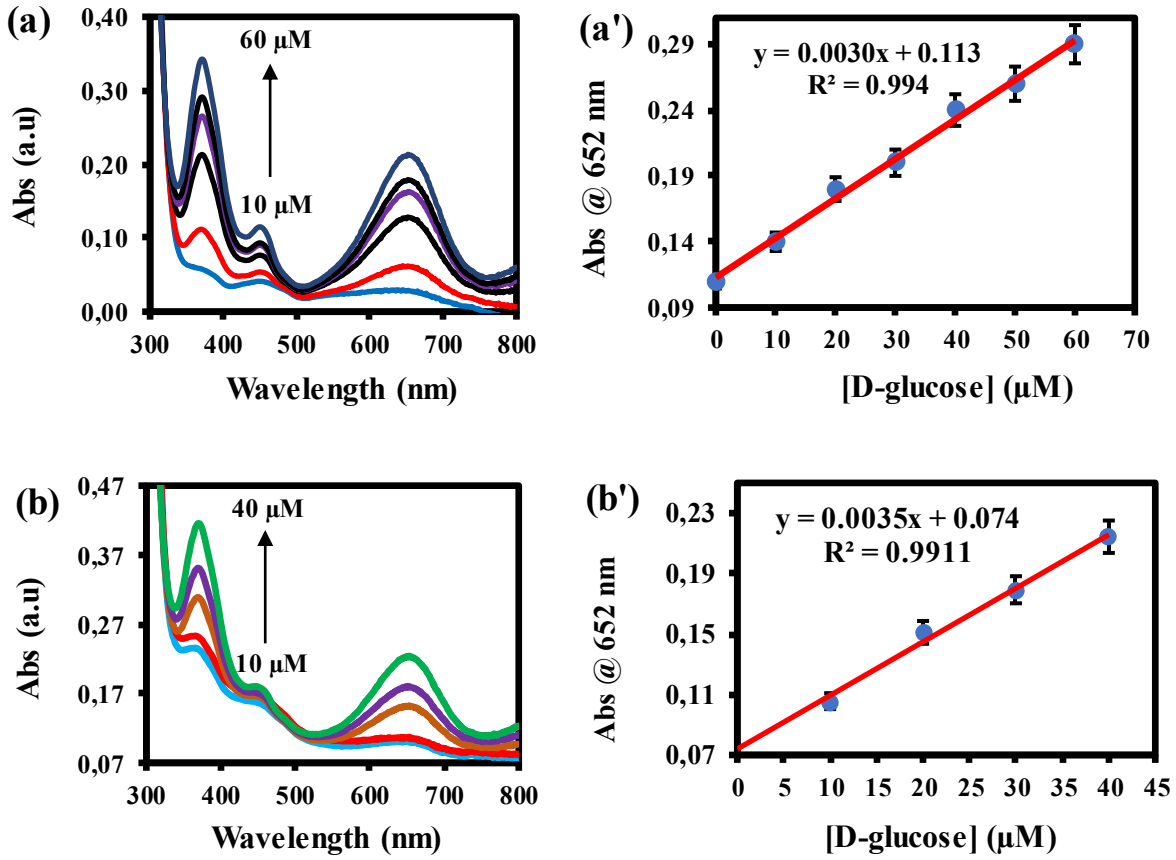

Figure 2.8: UV-vis spectra and the corresponding plots of absorbance @ 652 nm versus [D-glucose] concentration for (a) spherical CuONPs and (b) CuONRs.

Table 2.1: Comparison of the performance of different nanomaterials towards the detection of glucose.

Nanozyme	Linear range	LOD
spherical CuONPs[TW]	0 - 60 µM	0.73 µM
CuONRs[TW]	10 - 40 µM	0.13 µM
MoS_2–$Pt_{74}Ag_{26}$[28]	1 - 10 µM	0.80 µM
MoS_2 NSs[29]	5 - 150 µM	1.20 µM
CeO_2/nanotube TiO_2[30]	1 - 50 µM	6.10 µM
Fe_3O_4 NPs[31]	50 - 1000 µM	30.0 µM
Chitosan-Ag NPs[32]	5.0×10^{-6} - 2.0×10^{-4} M	100 nM
Fe_3O_4@MSN[33]	1.0×10^{-5} - 5.0×10^{-4} M	4.0 µM

TW – This work. NS – nanosheets. MSN - mesoporous silica nanoparticles.

2.8 Conclusion

The preparation of spherical CuONPs and CuONRs was achieved successfully. Their characterization using different spectroscopic and microscopic techniques confirmed the successful preparation. The spherical CuO nanoparticles and CuO nanorods were found to possess the intrinsic peroxidase-like activity which is similar to horseradish-peroxidase (HRP) enzyme. The optimum reaction conditions were 20 minutes, pH 5.0, 40 mM H_2O_2 concentration and 40 °C for a maximum UV-vis absorption of TMBDI, for both spherical CuONPs and CuONRs. The investigation of the steady-state kinetic parameters showed that the peroxidase-like activity of spherical CuONPs and CuONRs followed the Michaelis-Menten kinetics behaviour. The spherical CuONPs showed the K_m = 1.12 mM and 1.14 mM for H_2O_2 and TMB respectively. The CuONRs showed the K_m = 40.04 mM and 2.91 mM for H_2O_2 and TMB respectively. The production of reactive oxygen species (ROS) was investigated and detected using 1,3-diphenylisobenzofuran (DPBF). UV-vis spectroscopy and the DPBF

absorption band at 430 nm was monitored. The rate of degradation of DPBF is proportional to the concentration of H_2O_2. The rate of degradation of DPBF was 4.91 x 10^{-2} a.u./min and 5.99 x 10^{-2} a.u./min for spherical CuONPs and CuONRs respectively. The LOD and LOQ for spherical CuONPs were calculated and found to be 0.73 μM and 2.42 μM respectively. The LOD and LOQ for CuONRs were 0.13 μM and 0.42 μM respectively.

References

1. H. Wang, J. Xu, J. Zhu, H. Chen, J. Cryst. Growth., 2002 (244) 88 - 94.

2. A. Henglein, Chem. Rev. 1989 (89) 1861 - 1873.

3. A. Hagfeldt, M. Gratzel, Chem. Rev. 1995 (95) 49 - 68.

4. W.P. Dow, T.J. Huang, J. Catal., 1996 (160) 155 -170.

5. Y. Jiang, S. Decker, C. Mohs, K.J. Klabunde, J. Catal.,1998 (180) 24 - 34.

6. D. Das, B. C. Nath, P. Phukon, S. K. Dolui, Colloids Surf. B, 2013 (101) 430 - 433.

7. T.H. Tran, V.T. Nguyen, Int Sch Res Notices, 2014, 856592 (1 - 14).

8. Y. Yecheskel, I. Dror, and B. Berkowitz, Chemosphere, 2013 (93) 172 - 177.

9. A. Aslani and V. Oroojpour, Physica B: Condensed Matter, 2011 (406) 144 - 149.

10. Y. Li, J. Liang, Z. Tao, and J. Chen, Mater. Res. Bull., 2008 (43) 2380 - 2385.

11. X. Wang, X. Xu, J Thermophys Heat Trans, 1999 (13) 474 - 480.

12. S. Ishio, T. Narisawa, S. Takahashi, Y. Kamata, S. Shibata, T. Hasegawa, Z. Yan, X. Liu, H. Yamane, Y. Kondo, J. Ariake, J. Magn. Magn. Mater, 2012 (324) 295 - 302.

13. Y. Yang, Y. Wang, W. Tseng, ACS Appl. Mater. Interfaces 2017 (9) 10069 - 10077.

14. Z. Chen, J. Yin, Y. Zhou, Y. Zhang, L. Song, M. Song, S. Hu, N. Gu, Cytotoxicity. ACS Nano 2012 (6) 4001 - 4012.

15. J. Fan, J. Yin, B. Ning, X. Wu, Y. Hu, M. Ferrari, G.J. Anderson, J. Wei, Y. Zhao, G. Nie, Biomaterials, 2011 (32) 1611 - 1618.

16. Y. Ding, B. Yang, H. Liu, Z. Liu, X. Zhang, X. Zheng, Q. Liu, Sens. Actuators B Chem., 2018 (259) 775 - 783.

17. Y. Jv, B. Li, R. Cao, Chem. Commun.,2010 (46) 8017 - 8019.

18. H. Jiang, Z. Chen, H. Cao, Y. Huang, Analyst, 2012 (137) 5560 - 5564

19. K. Cai, Z. Lv, K. Chen, L. Huang, J. Wang, F. Shao, Y. Wang, H. Han, Chem. Commun., 2013 (49) 6024 - 6026.

20. W. Chen, J. Chen, Y.B. Feng, L. Hong, Q. Chen, L. Wu, X. Lin, X. Xia, Analyst, 2012 (137) 1706 - 1712.

21. J.M. Kshirsagar, R. Shrivastava, P.S. Adwani, Therm. Sci., 2017 (21) 233 - 242.

22. S. Taghavi Fardood, A. Ramazani, S.W. Joo, J. Struct. Chem., 2018 (59) 482 - 486.

23. R. Etefagh, E. Azhir, N. Shahtahmasebi. Sci. Iran., 2013 (20) 1055 - 1058.

24. J. Zhu, D. Li, H. Chen, X. Yang, L. Lu, X. Yang, Mater. Lett., 2004 (58) 3324 - 3327.

25. L. Gao, J. Zhuang, L. Nie, J. Zhang, Y. Zhang, N. Gu, T. Wang, J. Feng, D. Yang, S. Perrett, X. Yan, Nat. Nanotechnol., 2007 (2) 577 - 583.

26. Y. Zhang, J. Parrondo, S. Sankarasubramanian, V. Ramani, ChemSusChem, 2017 (10) 3056 - 3062.

27. T. T. Ohyashiki, Biochim. Biophys. Acta Biomembr. 1999 (1421) 131 - 139.

28. S. Cai, Q. Han, C. Qi , Z. Lian , X. Jia , R. Yang, C. Wang, Nanoscale, 2016 (8) 3685 - 3693.

29. T. Lin, L. Zhong, L. Guo, F. Fu and G. Chen, Nanoscale, 2014 (6) 11856 - 11862.

30. H. Zhao, Y. Dong, P. Jiang, G. Wang, J. Zhang, ACS Appl. Mater. Inter., 2015 (7) 6451 - 6461.

31. Q. An, C. Sun, D. Li, K. Xu, J. Guo, C. Wang, ACS Appl. Mater. Inter., 2013 (5) 13248 - 13257.

32. H. Jiang, Z. Chen, H. Cao, Y. Huang, Analyst, 2012 (137) 5560 - 5564.

33. Y. Wang, B. Zhou, S. Wu, K. Wang, X. He, Talanta, 2015 (134) 712 - 717.

CHAPTER 3

COPPER OXIDE NANORODS DECORATED WITH GOLD AND PALLADIUM NANOPARTICLES WITH PEROXIDASE-LIKE ACTIVITY AND COLORIMETRIC DETECTION OF GLUCOSE

Copper oxide nanorods decorated with gold and palladium nanoparticles with peroxidase-like activity and colorimetric detection of glucose

Simbongile Sicwetsha, Omotayo Adeniyi, Philani Mashazi

Department of Chemistry, Rhodes University, P.O. Box 94, Makhanda, 6140, South Africa

Abstract

The preparation of copper oxide nanorods (CuONRs) decorated with gold and palladium nanoparticles were successfully synthesized. The successful preparation of these nanomaterials was confirmed using various spectroscopic and microscopic techniques. The peroxidase-like activity of the prepared CuONRs decorated with gold and palladium nanoparticles were investigated by the catalytic oxidation of a chromogenic substrate (TMB) in the presence of hydrogen peroxide. Like Horseradish peroxidase (HRP) and other nano-mimics, the catalytic activity of CuONRs decorated with gold and palladium nanoparticles was dependent on pH, temperature and enzyme substrate concentration. The nanomaterials interact with hydrogen peroxide to produce hydroxyl radicals (OH·). Therefore, the production of reactive oxygen species (ROS) was investigated and detected using 1,3-diphenylisobenzofuran (DPBF) as a radical scavenger. CuONRs decorated with gold and palladium nanoparticles were further used in the fabrication of enzyme (glucose oxidase, GO_x) based biosensor for the detection of glucose.

KEYWORDS: *Copper oxide nanorods, gold and palladium nanoparticles, peroxidase-like activity, glucose detection.*

3.1 Introduction

Nanomaterials have received extensive attention due to their intriguing properties and various applications in the field of nanoscience and nanotechnology. The applications of nanomaterials include nanocatalysis, magnetite-supported catalysis, nanoelectronics, integrated catalysis, to name but a few.[1] The integration of inexpensive transition metals and noble metals with enhanced stability produces highly stable nanostructures to establish their synergistic effect.[2] The morphology, architecture and internal structure of the nanocomposites can be engineered by altering the molar ratios and the incorporation of metal precursors and templates.[3-5] The applications of nanohybrid structures have been reported to be dictated by their composition, structure, particle size and other auxiliary variables.[6-8] Liu and co-workers reported that noble metal nanoparticles integrated with metal oxide nanoparticles (NM-MOs) hybrid structures can be categorized into : (i) noble metal-decorated metal oxide nanoparticles, (ii) noble metal-decorated metal oxide nanoarrays, (iii) noble metal/metal oxide core/shell nanostructures, (iv) noble metal/metal oxide yolk/shell nanostructures and (v) Janus noble metal-metal oxide nanostructures.[6] The noble metal-metal oxide nanocomposites exhibit better catalytic performance in contrast to their monometallic analogues.[9,10] The improved catalytic performance can be ascribed to the synergistic effect induced by the alterations in the electronic structure between the support material (metal oxide) and interfacial noble metals.[9,11] Metal and metal oxide nanoparticles are extensively manufactured because they possess some interesting properties such as high catalytic activity, good recyclability and good product purifications.[12] Due to these interesting properties metal and metal oxide nanoparticles can be used in a variety of applications such as optical, electronic, magnetic, biological and mechanical materials.[12] The properties of metal and metal oxide nanoparticles are widely controlled by the preparation method used during their synthesis. The ability to integrate and modify nanostructured materials with different ligands and materials is dependent on various factors such as

composition, morphology, geometry, surface stoichiometry and crystallographic structure.[13] Nanoparticle size has been reported to play a significant role in the applications of nanostructured materials as it is capable of transforming their properties.[13] The successive evolution of nanotechnology has afforded us an insight into heterogeneous catalysts, which has led to the probability of fabricating nanomaterial based artificial enzymes.[14,15] Natural enzymes possess exceptional catalytic efficiency, substrate specificity and high selectivity and this has resulted in their applications in biosensor applications.[16] However natural enzymes possess some limitations which impede their industrial applications, these include, low stability in harsh conditions, relative high cost for preparation, purification and storage, difficulty of recycling, pH-sensitive activity and short-term storage.[14,16] Artificial enzymes show superiority to natural enzymes due to low cost, long-term storage and high stability.[16] Therefore, artificial enzymes have been developed to counteract the challenges possessed by natural enzymes. Iron oxide nanoparticles were the first inorganic nanomaterials that were found to display inherent peroxidase-like activity.[17,18] The diversity of metal oxide and noble metal nanoparticles such V_2O_5 and platinum nanoparticles were also found to demonstrate the peroxidase-like activity similar to Horseradish-peroxidase (HRP).[19,20] In this work we have devoted our attention to the preparation of metal oxide nanoparticles decorated with noble metals to enhance catalytic activity. The prepared nanomaterials were evaluated for their potential to mimic the catalytic activity of HRP. The nanomaterials studied include, CuO nanorods (CuONRs), CuONRs@$Au_{1.0}$NPs, CuONRs@$Pd_{1.0}$NPs and CuONRs@$Au_{0.5}$/$Pd_{0.5}$NPs.

3.2 Experimental

3.2.1 Reagents and Apparatus

Copper acetate $Cu(COOCH_3)_2$, Hydrogen tetrachloroaurate trihydrate ($HAuCl_4.3H_2O$, 99%), dihydrogen tetrachloropalladate (H_2PdCl_4), sodium citrate tribasic ($Na_3C_6H_5O_7$), sodium borohydride ($NaBH_4$), 3,3',5,5'-tetramethylbenzidine (TMB), glacial acetic acid (CH_3COOH), 1,3-diphenylisobenzofuran (DPBF), D-glucose powder, glucose oxidase (GOx, EC 1.1.3.4. from Aspergillus niger, Type VII) were purchased from Sigma-Aldrich. Potassium hydroxide pellets (KOH), sodium acetate anhydrous ($C_2H_3NaO_2$), and potassium dihydrogen orthophosphate (KH_2PO_4) were purchased from Merck. Sodium hydroxide pellets (NaOH), absolute ethanol (C_2H_5OH), methanol (CH_3OH), hydrogen peroxide (H_2O_2), 50%, C.P, hydrochloric acid (HCl), 32 %, C.P, and dimethyl sulfoxide (DMSO) were purchased from B&M Scientific. All the reagents were of analytical grade and were used as received from the suppliers. Ultrapure water with the resistivity of 18 MΩ.cm obtained from a Milli-Q water system (Millipore Corp, Bedford, MA, USA) was used for the preparation of standard solutions.

UV-visible measurements were conducted on a ThermoScientific, Multiskan Sky w Cuvette & Touch Screen, 100 – 240 V, Belgium . Zeta potential measurements were carried out on a Malvern Zetasizer Nano-ZS90 series equipped with a 633 nm He/Ne laser. A disposable folded capillary cell (DTS 1060) was used for data collection. TEM images were taken from a Zeiss Libra 120 TEM operating at 80 kV. The nanoparticles were dissolved in water and dropped onto a carbon-coated copper grid and allowed to dry at room temperature overnight before data collection. The EDS spectra were obtained from INCA PENTA FET coupled with VGA TESCAM at 20 kV acceleration voltage. X-ray powder diffraction (XRD) patterns were recorded on a Bruker D8 Discover equipped with a Lynx Eye detector, using Cu-Ka radiation

(1.5405 Å, nickel filter). The data were collected within 2θ range of 10° to 100°. The samples were placed on a silicon wafer slide.

3.3 Preparation of nanomaterials

3.3.1 Preparation of copper oxide nanorods (CuONRs)

Copper oxide nanorods were prepared following the sol-gel method (as outlined in Chapter 2), with slight modifications.[21] Briefly, 75 ml of 80 mM copper acetate solution was blended with 1 ml glacial acetic acid in a round-bottom flask. The reaction was heated to reflux with continuous stirring. A 10 ml solution of sodium hydroxide (6 M) was added quickly. A black precipitate formed immediately. The reaction was allowed to react for 30 minutes. The precipitate was centrifuged, washed three times with ethanol and air dried in room temperature.

3.3.2 Preparation of CuONRs decorated with gold (CuONRs@$Au_{1.0}$NPs)

The preparation of CuONRs@$Au_{1.0}$NPs was achieved using a method that has been previously reported.[17] Briefly, 20 mg of copper oxide nanorods (CuONRs) was dissolved in 60 ml of Millipore water and sonicated for 30 minutes. Then 10 ml of $HAuCl_4.3H_2O$ aqueous solution (0.60 mM) was added. Sodium citrate (3 mg in 1.5 ml) was added to the mixture kept at room temperature. Sodium borohydride (3 mg in 1.5 ml) was added after 15 minutes at once. The colour changed immediately from dark brown to black. The reaction was stirred vigorously for 2 hours. The precipitate was centrifuged, washed three times with ethanol and air dried at room temperature.

3.3.3 Preparation of CuONRs decorated with palladium (CuONRs@$Pd_{1.0}$NPs)

Similar procedure as for CuONRs@$Au_{1.0}$NPs was used for the preparation of CuONRs@$Pd_{1.0}$NPs but instead of $HAuCl_4.3H_2O$, H_2PdCl_4 (10 ml, 0.60 mM) was added. Sodium citrate (3.0 mg in 1.50 ml) was added to the mixture kept at room temperature. Sodium borohydride (3.0 mg in 1.50 ml) was added after 15 minutes all at once. The colour changed immediately from dark brown to black. The reaction was stirred vigorously for 2 hours. The precipitate was centrifuged, washed three times with ethanol and air dried at room temperature.

3.3.4 Preparation of CuONRs decorated with gold and palladium bimetallic nanoparticles (CuONRs@$Au_{0.5}/Pd_{0.5}$NPs)

Similar procedure above was used for the preparation of CuONRs@$Au_{0.5}/Pd_{0.5}$NPs. Briefly, 20 mg of copper oxide nanorods (CuONRs) were dispersed in 60 ml of Millipore water and sonicated for 30 minutes. $HAuCl_4.3H_2O$ (5 ml, 0.60 mM) and H_2PdCl_4 (5 ml, 0.60 mM) aqueous solutions were added simultaneously at room temperature. Sodium citrate (3 mg in 1.5 ml) was added to the mixture. After 15 minutes sodium borohydride (3 mg in 1.5 ml) was added at once. The colour changed immediately from dark brown to black. The reaction was stirred vigorously for 2 hours. The precipitate was centrifuged, washed three times with ethanol and air dried at room temperature.

3.4 Peroxidase-like activity

The investigation of the peroxidase-like activity of CuONRs and the Au and Pd decorated nanoparticles was conducted at room temperature using 3,3',5,5'-tetramethylbenzidine (TMB) in the presence of hydrogen peroxide (H_2O_2). Briefly, hydrogen peroxide (50 µL, 100 mM), TMB (50 µL, 25 mM), and different nanoparticles (10 µL, 6.28 mM) were added to 0.2 M acetate buffer solution (at the pH where IEP is zero for different decorated nanorods) in a

cuvette. After adding the nanoparticles to the acetate buffer solution containing TMB and hydrogen peroxide, the evolution of a blue colour was observed.

3.5 Evaluating reactive oxygen species (ROS) generation using DPBF (radical quencher)

The production of reactive oxygen species (ROS) was investigated using 1,3-diphenylisobenzofuran (DPBF) as a radical scavenger. The generation of ROS was studied using DPBF (50 µL, 0.25 mM), and hydrogen peroxide (75 µL, 100 mM) in the presence of (50 µL, 6.0 mM) CuONRs and their gold and palladium decorated nanorods. UV-vis spectroscopy was used to monitor the absorption band at 430 nm. The absorbance measurements were taken at one-minute interval for 20 minutes.

3.6 Glucose detection using the prepared CuONRs decorated with gold and palladium nanoparticles

Glucose detection using the CuONRs and their gold and palladium decorated nanorods was conducted by the enzymatic reaction between D-glucose and glucose oxidase (GOx) to yield D-gluconolactone and hydrogen peroxide. Briefly, GOx (50 µL, 1.0 $mg.mL^{-1}$) was added to the solution of D-glucose (25 µL, varied concentration) in phosphate buffer (75 µL, pH 7) and incubated at 35 °C for 45 minutes. After 45 minutes, a 50 µL solution of 400 µL of CuONRs and their gold and palladium decorated nanorods, and TMB (100 µL, 2.0 mM) in acetate buffer (1.0 ml, 0.20 M) at optimum pH was added to the glucose solution at 35 °C.

3.7 Results and Discussion

3.7.1 Synthesis and Characterization of CuONRs decorated with gold and palladium nanoparticles

The preparation of CuONRs@$Au_{0.5}$/$Pd_{0.5}$NPs was achieved using a two-step procedure. Initially, CuO nanoparticles were prepared using the chemical reduction method.[17] The conventional sol-gel method was optimised to yield CuO nanorods (CuONRs). The morphology and the architecture of the CuONRs provides a suitable surface to be utilized as a support platform for anchoring gold and palladium nanoparticles. The CuONRs@$Au_{0.5}$/$Pd_{0.5}$NPs were prepared by the deposition of gold and palladium on the surface of CuONRs. The deposition of gold and palladium on the surface of the preformed CuONRs was achieved by the simultaneous co-reduction of $HAuCl_4.3H_2O$ and H_2PdCl_4 aqueous solutions. Sodium borohydride was used as a reducing agent for both $HAuCl_4.3H_2O$ and H_2PdCl_4 precursors. Sodium borohydride induced the simultaneous reduction of Au^{3+} to Au^0 and Pd^{2+} to Pd^0. The reaction was carried out in an ice-water bath. The low temperatures were used to facilitate the formation of smaller size gold and palladium nanoparticles on the surface of CuO nanorods support material. The CuONRs@$Au_{1.0}$NPs and CuONRs@$Pd_{1.0}$NPs were prepared following the same method as CuONRs@$Au_{0.5}$/$Pd_{0.5}$NPs. The integration of CuONRs (support material) decorated with gold and palladium nanoparticles to form a nanoalloy structure is expected to yield a system with enhanced catalytic performance. The improved catalytic performance of such systems emanates from the synergistic effect and the large surface area provided by the support material. The bimetallic nanoalloy systems have been reported to possess bifunctional performance.[3] Marelli et.al mentioned that in order to understand the inception of the synergistic effect between metallic systems, the morphology and structure needs to be analysed thoroughly.[22]

X-ray diffraction (XRD) was used to analyse the successful formation of CuONRs and CuONRs decorated with gold and palladium nanoparticles. **Figure 3.1(a)** shows the X-ray diffraction patterns of (i) CuONRs (black), (ii) CuONRs@$Au_{1.0}$NPs (red), (iii) CuONRs@$Pd_{1.0}$NPs (green), and (iv) CuONRs@$Au_{0.5}$/$Pd_{0.5}$NPs (purple). The X-ray diffractograms for CuO NRs were observed at 32.6, 35.6, 38.8, 48.9, 53.3, 57.9, 61.5, 65.9, 67.5, 71.9, 74.5° corresponding to (110), (-111), (111), (-202), (020), (202), (-113), (022), (311), (004) Miller indices. The X-ray diffractograms showed single phase copper oxide nanoparticles with a monoclinic structure with lattice constants, a = 4.67970, b = 3.43140, c = 5.13620, α = 90.00, β = 99.26 and γ = 90.00. There were no additional diffractograms that emanate from other elements, this indicates high purity of the prepared CuONRs. The CuONRs@$Au_{1.0}$ nanoparticles showed the diffraction patterns that are due to the presence of AuNPs at 38.4, 44.4, 64.5, 77.7° corresponding to (111), (200), (220), (311) Miller indices, of a face-centred cubic crystal structure of gold. The CuONRs@$Pd_{1.0}$NPs showed the diffraction patterns that are due to the presence of PdNPs at 40.1, 46.3, 68.5, 82.1, 86.0° corresponding to (111), (200), (220), (311), (222) Miller indices. The CuONRs@$Au_{0.5}$/$Pd_{0.5}$NPs showed the mixture of diffraction patterns and Miller indices that were observed for individual CuONRs, CuONRs@$Au_{1.0}$NPs and CuONRs@$Pd_{1.0}$NPs. After the deposition of Au and PdNPs on the surface of CuONRs, the diffractograms of CuONRs at 35.6 and 38.8 were splitted and the intensity decreased. The XRD showed very small diffractograms that emanate from Au and Pd nanoparticles, this may be ascribed to the small size and the small ratio of Au and Pd on the nanocomposite.[3] **Figure 3.1(b)** shows the plot of zeta potential (mV) versus pH for CuONRs (black), CuONRs@$Au_{1.0}$NPs (red), CuONRs@$Pd_{1.0}$NPs (green) and CuONRs@$Au_{0.5}$/$Pd_{0.5}$ NPs (purple). The CuONRs, CuONRs@$Au_{1.0}$NPs, CuONRs@$Pd_{1.0}$NPs and CuO@$Au_{0.5}$/$Pd_{0.5}$NPs showed almost identical zeta potential results at different pH. The positive zeta potential were obtained at pH 2. When the pH was adjusted from pH 3 – 10, the

negative zeta potential were observed for all the prepared nanoparticles. Sodium hydroxide was used as a reducing agent during the synthesis of CuONRs. Thus, the nagative zeta potential on CuONRs can be ascribed to the negatively charged hydroxyl groups (-OH) on the surface of the nanorods. The negative zeta potential for CuONRs@$Au_{1.0}$NPs, CuONRs@$Pd_{1.0}$NPs and CuONRs@$Au_{0.5}$/$Pd_{0.5}$NPs can be ascribed to the citrate ion because sodium citrate was used as stabilizing agent to minimize aggregation of Au and Pd nanoparticles on the surface of CuONRs. The negative zeta potential may also be due to the fact that CuONRs are not completely enveloped by Au and Pd nanoparticles. Thus, the surface charge of the hydroxyl groups on CuONRs may still be accessible for binding. The CuONRs exhibited the isoelectric point at pH 2.5. The isoelectric point (IEP) was slightly shifted for CuONRs@$Au_{1.0}$NPs (pH 3.2), CuONRs@$Pd_{1.0}$NPs (pH 3.3) and CuONRs@$Au_{0.5}$/$Pd_{0.5}$NPs (pH 2.7). The nanoparticles experience zero net charge at the isoelectric point and the aggregation of the nanoparticles is likely to occur. Alterations in the zeta potential measurements have an effect on stability of the nanoparticles.[23] The CuONRs, CuONRs@$Au_{1.0}$NPs, CuONRs@$Pd_{1.0}$NPs and CuONRs@$Au_{0.5}$/$Pd_{0.}$5NPs were unstable in the studied pH range. The stability of the nanoparticles is observed at ±30 mV. Furthermore, negative zeta potential were observed at pH 7, for CuONRs (-25.8 mV), CuONRs@$Au_{1.0}$NPs (-25.2 mV), CuONRs@$Pd_{1.0}$NPs (-22.9 mV) and CuONRs@$Au_{0.5}$/$Pd_{0.5}$NPs (-20.0 mV). The negative zeta potential show that the CuONRs decorated with gold and palladium nanoparticles have negatively charged at neutral pH (pH 7.0).

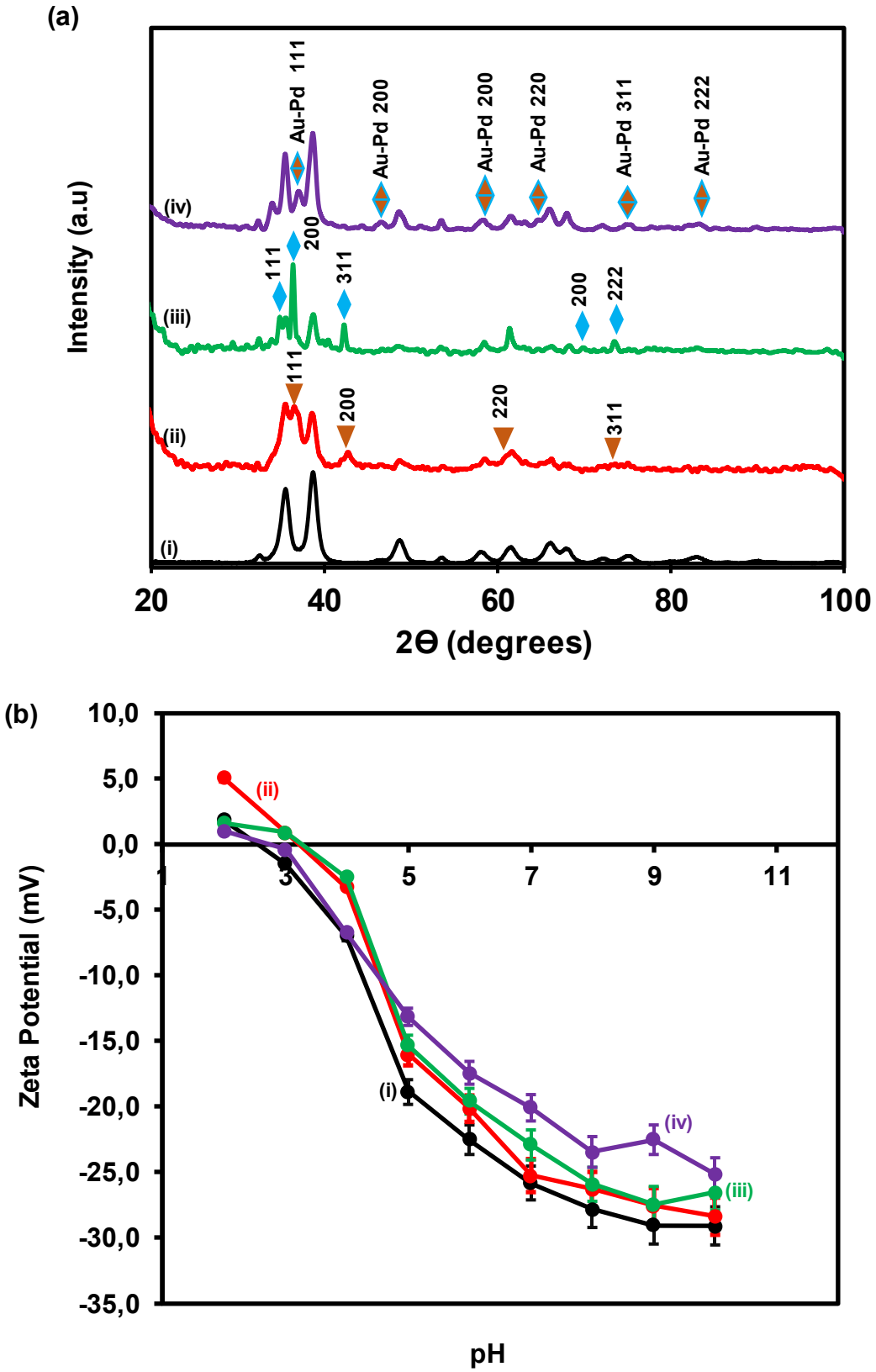

Figure 3.1: (a) X-ray diffraction patterns and (b) Zeta potential vs pH of (i) CuONRs, (ii) CuONRs@$Au_{1.0}$NPs , (iii) CuONRs@$Pd_{1.0}$NPs, and (iv) CuONRs@$Au_{0.5}$/ $Pd_{0.5}$NPs.

The prepared nanorods and their decoration with gold and palladium nanoparticles was confirmed using transmission electron microscope (TEM). **Figure 3.2** shows TEM micrographs with their corresponding size distribution histograms for (a) CuONRs, (b) CuONRs@$Au_{1.0}$NPs, (c) CuONRs@$Pd_{1.0}$NPs, and (d) CuONRs@$Au_{0.5}/Pd_{0.5}$NPs. The TEM image of CuO showed rod-like shaped structures with the length of 40. ± 5.6 nm and the width of 11. ± 4.5 nm. The TEM image in **Figure 3.2(a)** also showed some aggregation. Chen et.al also observed some aggregation of CuO nanoparticles.[21] The TEM image of CuONRs@$Au_{1.0}$NPs retained the rod-like structure of CuONRs with spherical gold nanoparticles deposited on the surface of CuONRs. The average particle size of Au nanoparticles on the surface of CuONRs was 2.9 ± 1.2 nm. The TEM image of CuONRs@$Pd_{1.0}$ nanoparticles showed that spherical palladium nanoparticles were deposited on the surface of CuONRs. The average size of palladium nanoparticles was 2.8 ± 1.5 nm. The TEM image of CuONRs@$Au_{0.5}/Pd_{0.5}$ nanoparticles also showed spherical gold and palladium nanoparticles anchored on the surface of CuONRs. The average size of Au and Pd bimetallic nanoparticles on the surface of CuONRs was 2.4 ± 1.6 nm.

Energy dispersive spectroscopy (EDS) was used to investigate the elemental composition of the prepared CuONRs with their decoration with gold and palladium nanoparticles. **Figure 3.3** shows EDS spectra of (a) CuONRs, (b) CuONRs@$Au_{1.0}$NPs, (c) CuONRs@$Pd_{1.0}$NPs, and (d) CuONRs@$Au_{0.5}/Pd_{0.5}$NPs. The EDS spectrum of CuONRs showed the presence of Cu, O and C. The presence of C emanates from the carbon tape that was used to mount the sample on the grid. The EDS spectra of CuONRs@$Au_{1.0}$NPs, CuONRs@$Pd_{1.0}$NPs and CuONRs@$Au_{0.5}/Pd_{0.5}$ NPs showed additional peaks that are due to Au and Pd nanoparticles. The high peak intensity of Cu and O indicates that the percent composition of the nanorods was dominated by CuO nanorods.

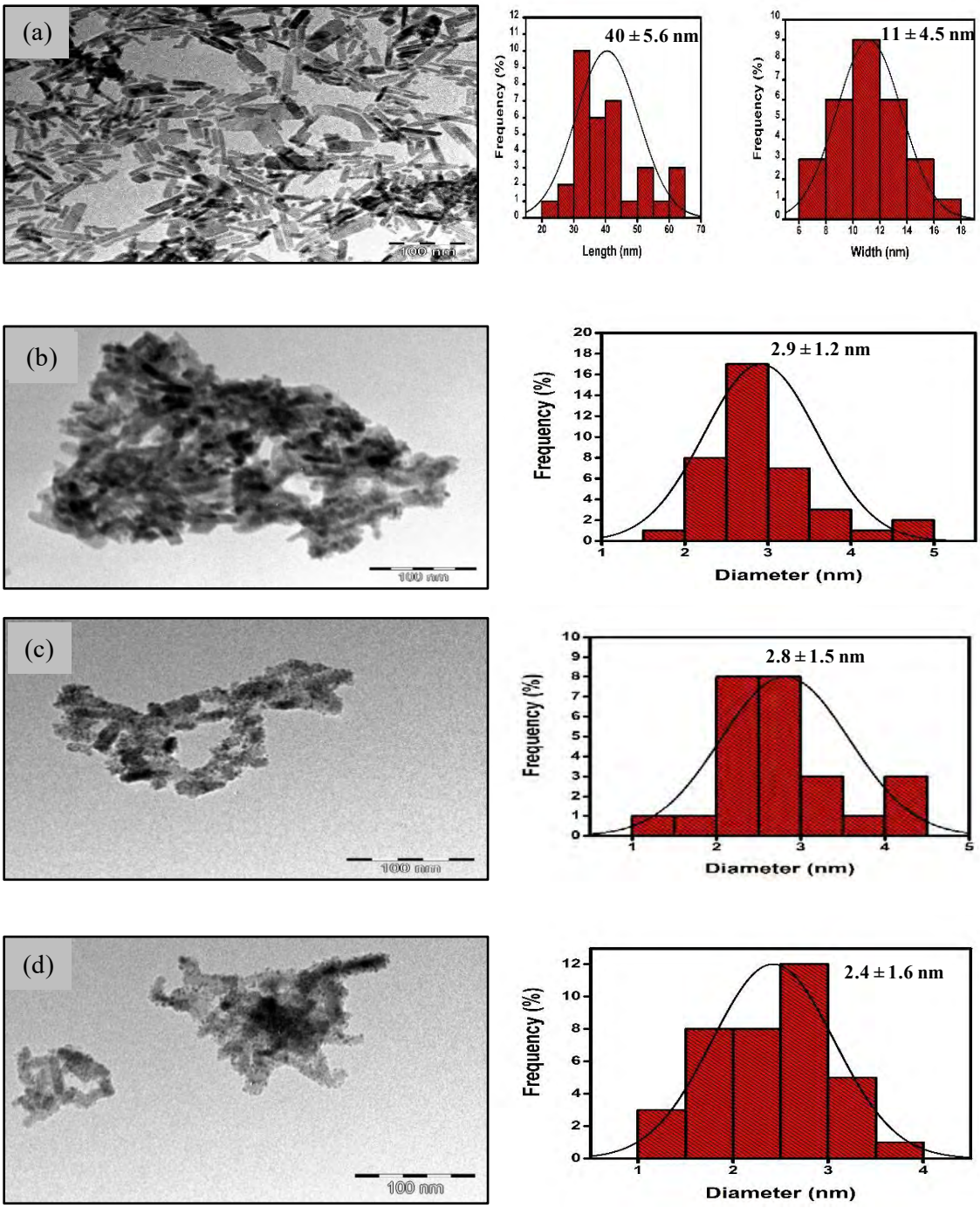

Figure 3.2: TEM micrographs with their corresponding size distribution histograms for (a) CuONRs, (b) CuONRs@$Au_{1.0}$NPs, (c) CuONRs@$Pd_{1.0}$NPs, and (d) CuONRs@$Au_{0.5}/Pd_{0.5}$ NPs.

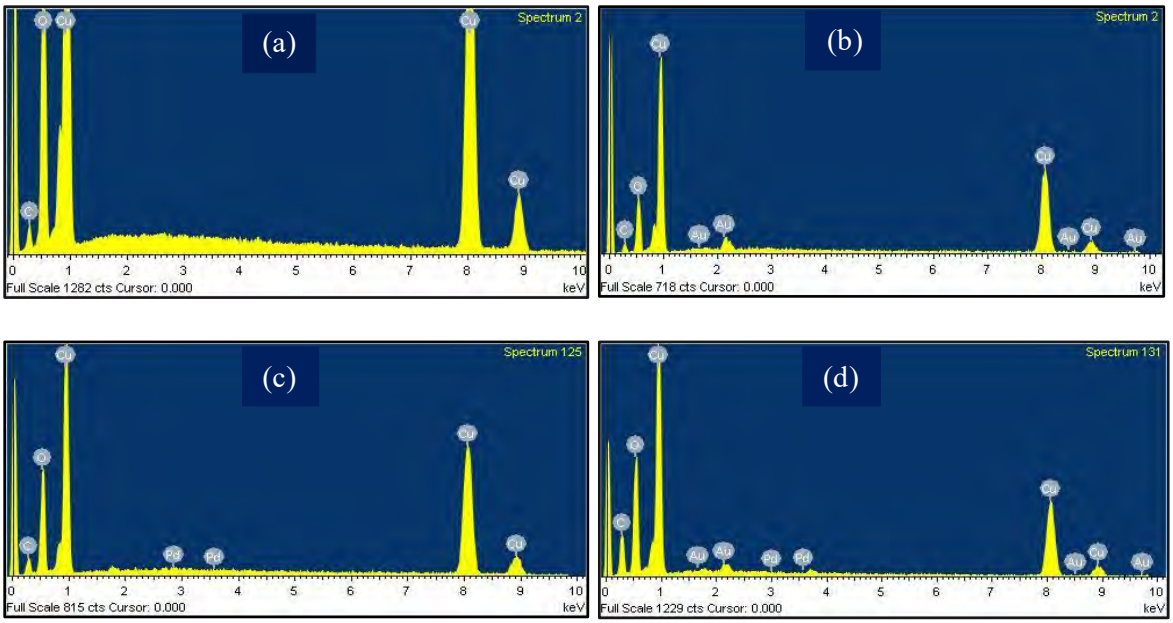

Figure 3.3: EDS spectra of (a) CuONRs, (b) CuONRs@$Au_{1.0}$NPs, CuONRs@$Pd_{1.0}$NPs, and (d) CuONRs@$Au_{0.5}$/$Pd_{0.5}$NPs.

3.7.2 Peroxidase-like activity of CuONRs decorated with gold and palladium nanoparticles

The CuONRs decorated with gold and palladium bimetallic nanoparticles were investigated for their potential as Horseradish Peroxidase (HRP) nano-mimics. The peroxidase-like activity of CuONRs and bimetallic nanoparticles was investigated by their catalytic oxidation of a chromogenic substrate 3,3',5,5'-tetramethylbenzidine (TMB) in the presence of H_2O_2. TMB is a colourless chromogenic substrate which upon oxidation is transformed to a blue coloured tetramethylbenzidine diimine (TMBDI) charge transfer complex with a maximum absorption band at 652 nm wavelength. The peroxidase-like activity was evaluated using UV-vis spectroscopy to monitor the reaction. **Figure 3.4** shows the UV-vis absorption spectra of (i) NRs + H_2O_2 (blue), (ii) NRs + TMB (yellow), (iii) CuONRs + H_2O_2 + TMB (black), (iv) CuONRs@$Au_{1.0}$NPs + H_2O_2 + TMB (red), (v) CuONRs@$Pd_{1.0}$NPs + H_2O_2 + TMB (green), (vi) CuONRs@$Au_{0.5}$/$Pd_{0.5}$NPs + H_2O_2 + TMB (purple) in 0.20 M acetate buffer solution (at the pH where IEP is zero for different nanoparticles). (b) Images of (i) NRs + H_2O_2, Ns + TMB, and (iii) NRs + H_2O_2 + TMB. In **Figure 3.4(a)**, the UV-vis absorption spectra of, CuONRs + H_2O_2 + TMB (black), CuONRs@$Au_{1.0}$NPs + H_2O_2 + TMB (red), CuONRs@$Pd_{1.0}$NPs + H_2O_2 + TMB (green), CuONRs@$Au_{0.5}$/$Pd_{0.5}$NPs + H_2O_2 + TMB (purple) showed the emergence of the three absorption bands at 370, 450 and 652 nm. When the peroxidase-like activity occurred the colour changed to blue as illustrated in **Figure 3.4(b)**. The prepared nanomaterials in the presence of H_2O_2 and TMB showed the evolution of a blue coloured species. The results are identical to that of HRP reaction in the presence of both H_2O_2 and TMB. The emergence of the absorption bands at 370, 450 and 652 nm, and the evolution a blue coloured (TMBDI) shows that the prepared nanorods exhibit the peroxidase-like activity.

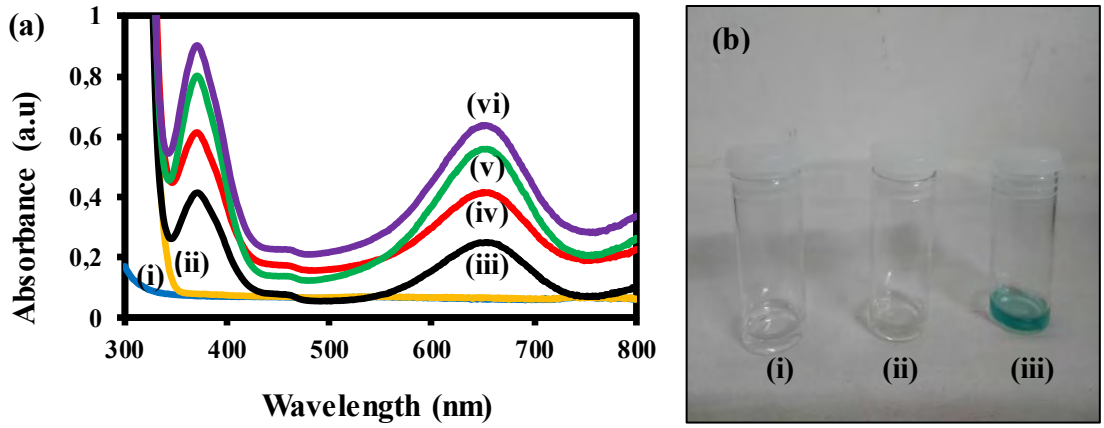

Figure 3.4: (a) UV-vis absorption spectra of (i) NRs + H_2O_2 alone (blue), (ii) NRs + TMB alone (yellow), (iii) CuONRs + H_2O_2 + TMB (black), (iv) CuONRs@$Au_{1.0}$NPs + H_2O_2 + TMB (red), (v) CuONRs@$Pd_{1.0}$NPs + H_2O_2 + TMB (green), (vi) CuONRs@$Au_{0.5}$/$Pd_{0.5}$NPs + H_2O_2 + TMB (purple) in 0.20 M acetate buffer solution. (b) Images of (i) NRs + H_2O_2 (100 mM), (ii) NRs + TMB (25 mM), and (iii) NRs + H_2O_2 (100 mM) + TMB (25 mM).

3.7.3 Conditions affecting the peroxidase-like of CuONRs decorated with gold and palladium (bi)metallic nanoparticles

The peroxidase-like activity of the prepared CuONRs and their (bi)metallic nanoparticles is dependent on diverse environmental conditions such as pH, substrate concentration and temperature. **Figure 3.5** shows the effect of (a) reaction time, (b) pH, (c) varying H_2O_2 concentration, and (d) temperature on peroxidase-like activity of CuONRs (black), CuONRs@$Au_{1.0}$NPs (red), CuONRs@$Pd_{1.0}$NPs (green), and CuONRs@$Au_{0.5}$/$Pd_{0.5}$NPs (purple). In **Figure 3.5(a)**, the effect of reaction time was investigated by increasing the reaction time from 0 – 18 minutes. The peroxidase-like activity of CuONRs and their (bi)metallic nanoparticles increased linearly as the reaction time increased. The CuONRs@$Au_{0.5}$/$Pd_{0.5}$NPs showed the highest rate of increase in absorbance (at 652 nm) with

increasing reaction time. In **Figure 3.5(b)**, the effect of pH was investigated by changing the pH from 3 – 9. The maximum peroxidase-like activity was obtained at pH 5.0 for CuONRs, pH 4.0 for CuONRs@$Au_{1.0}$NPs, pH 6.0 for CuONRs@$Pd_{1.0}$NPs and pH 4.0 for CuONRs@$Au_{0.5}$/$Pd_{0.5}$NPs. In alkaline conditions a decrease in peroxidase-like activity was observed due to the instability (decomposition) of H_2O_2 in alkaline conditions. In **Figure 3.5(c)**, the effect of varying H_2O_2 concentration while keeping TMB concentration constant was investigated. The H_2O_2 concentration was varied from 0 - 40 mM while the concentration of TMB was kept constant at 25 mM. When the H_2O_2 concentration was increased from 0 - 40 mM, an increase in peroxidase-like activity of CuONRs, CuONRs@$Au_{1.0}$NPs, CuONRs@$Pd_{1.0}$NPs and CuONRs@$Au_{0.5}$/$Pd_{0.5}$NPs was observed. A linear relationship between the absorbance at 652 nm and H_2O_2 concentration was established for CuONRs, CuONRs@$Au_{1.0}$NPs, CuONRs@$Pd_{1.0}$NPs and CuONRs@$Au_{0.5}$/$Pd_{0.5}$NPs. In **Figure 3.5(d)**, the effect of increasing the temperature from 20 – 40°C was investigated. The CuONRs, CuONRs@$Au_{1.0}$NPsand CuONRs@$Au_{0.5}$/$Pd_{0.5}$NPs showed an increase in peroxidase-like activity when the temperature was increased from 20 – 40°C. When the temperature was increased from 20 – 35°C, the CuONRs@$Pd_{1.0}$NPs showed an increase in peroxidase-like activity and decreased drastically at 40°C. The optimum temperature for CuONRs and CuONRs@$Au_{1.0}$NPs was 40°C, 35°C for CuONRs@$Pd_{1.0}$NPs and 30°C for CuONRs@$Au_{0.5}$/$Pd_{0.5}$NPs.

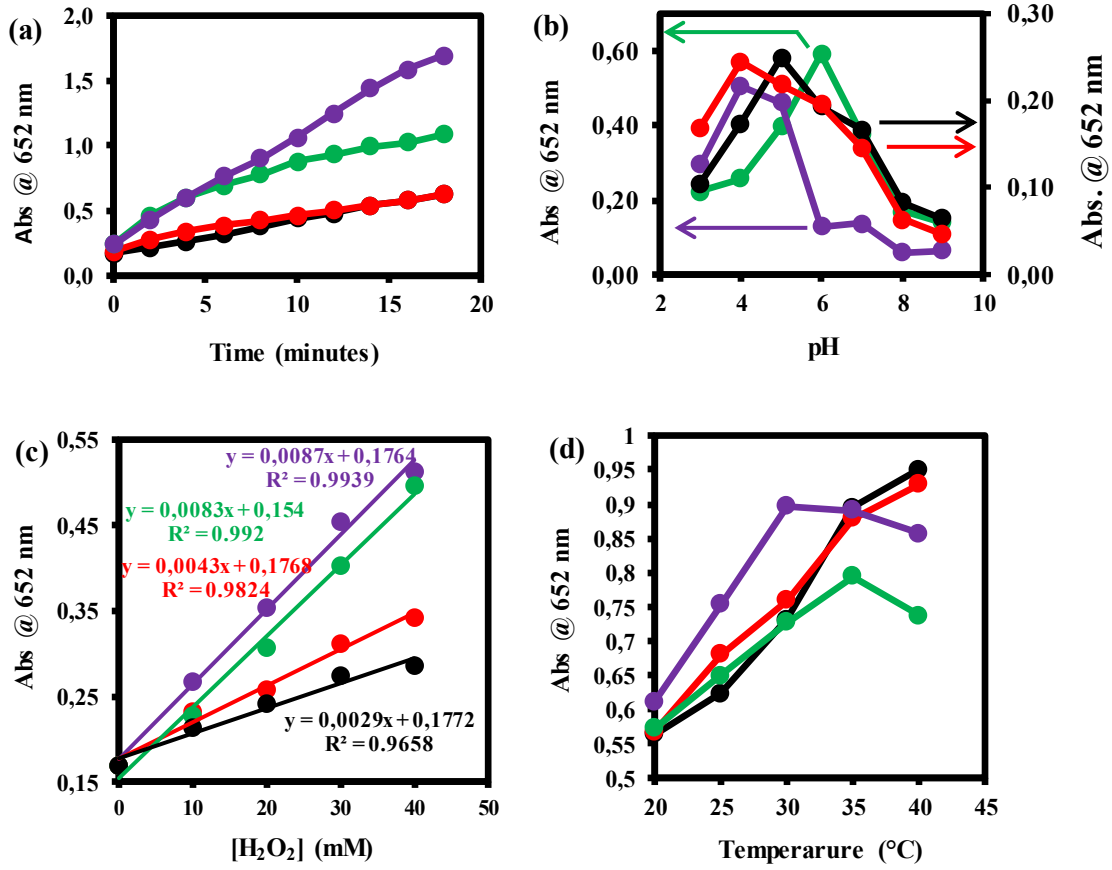

Figure 3.5: Effect of (a) reaction time, (b) pH, (c) changing H_2O_2 concentration, and (d) temperature on peroxidase-like activity of CuONRs (black), CuONRs@$Au_{1.0}$NPs (red), CuONRs@$Pd_{1.0}$NPs (green), and CuONRs@$Au_{0.5}/Pd_{0.5}$NPs (purple).

3.7.4 Steady-state kinetics of CuONRs decorated with gold and palladium (bi)metallic nanoparticles

The steady-state kinetic parameters of CuONRs decorated with gold and palladium nanoparticles were investigated using the Michaelis-Menten and Lineweaver-Burk (double reciprocal) models. The kinetic parameters were derived by varying one substrate concentration while keeping the other substrate constant. H_2O_2 and TMB were used as substrates for the evaluation of the peroxidase-like activity of CuONRs decorated with gold

and palladium nanoparticles using the steady-state kinetics model. The Michaelis-Menten parameters (Michaelis-Menten constant, K_m and maximum velocity, V_{max}) were obtained by fitting the data obtained from the plot of initial velocity (V_o) versus substrate concentration [S] to the Lineweaver-Burk double reciprocal plot. **Figure 3.6** shows a plot of initial velocity (V_o) versus varied [H_2O_2] concentration at a fixed [TMB] concentration, and their corresponding double reciprocal plots for (a) CuONRs@$Au_{1.0}$NPs, (b) CuONRs@$Pd_{1.0}$NPs, and (c) CuONRs@$Au_{0.5}$/$Pd_{0.5}$NPs. The linear relationship between initial velocity (V_o) and substrate (H_2O_2) concentration was established at lower concentrations of the substrate. The plateau was reached at higher concentrations of H_2O_2. K_m and V_{max} were calculated using the Lineweaver-Burk (double reciprocal plots) by using the intercepts and slope of the graph. The K_m and V_{max} values obtained are summarised in **Table 3.1** for H_2O_2 and TMB as substrates. The K_m value indicates the binding affinity of the nanoparticles towards the substrate.[24,25] A lower K_m value shows a stronger binding affinity while a higher K_m value signifies a weak binding affinity towards a particular substrate. The CuONRs@$Pd_{1.0}$NPs showed a lowest K_m value (0.13 mM) whilst CuONRs@$Au_{1.0}$NPs showed the highest K_m value of 3.05 mM when H_2O_2 was used as a substrate. The results indicate that the CuONRs@$Pd_{1.0}$NPs had a stronger binding affinity for the substrate (H_2O_2). The CuONRs@$Au_{0.5}$/$Pd_{0.5}$NPs also showed a strong binding affinity (K_m = 2.66 mM) for H_2O_2 as a substrate. The CuONRs@$Au_{1.0}$NPs (Km = 3.05 mM) showed a weaker binding affinity compared to CuONRs@$Pd_{1.0}$NPs and CuONRs@$Au_{0.5}$/$Pd_{0.5}$NPs.

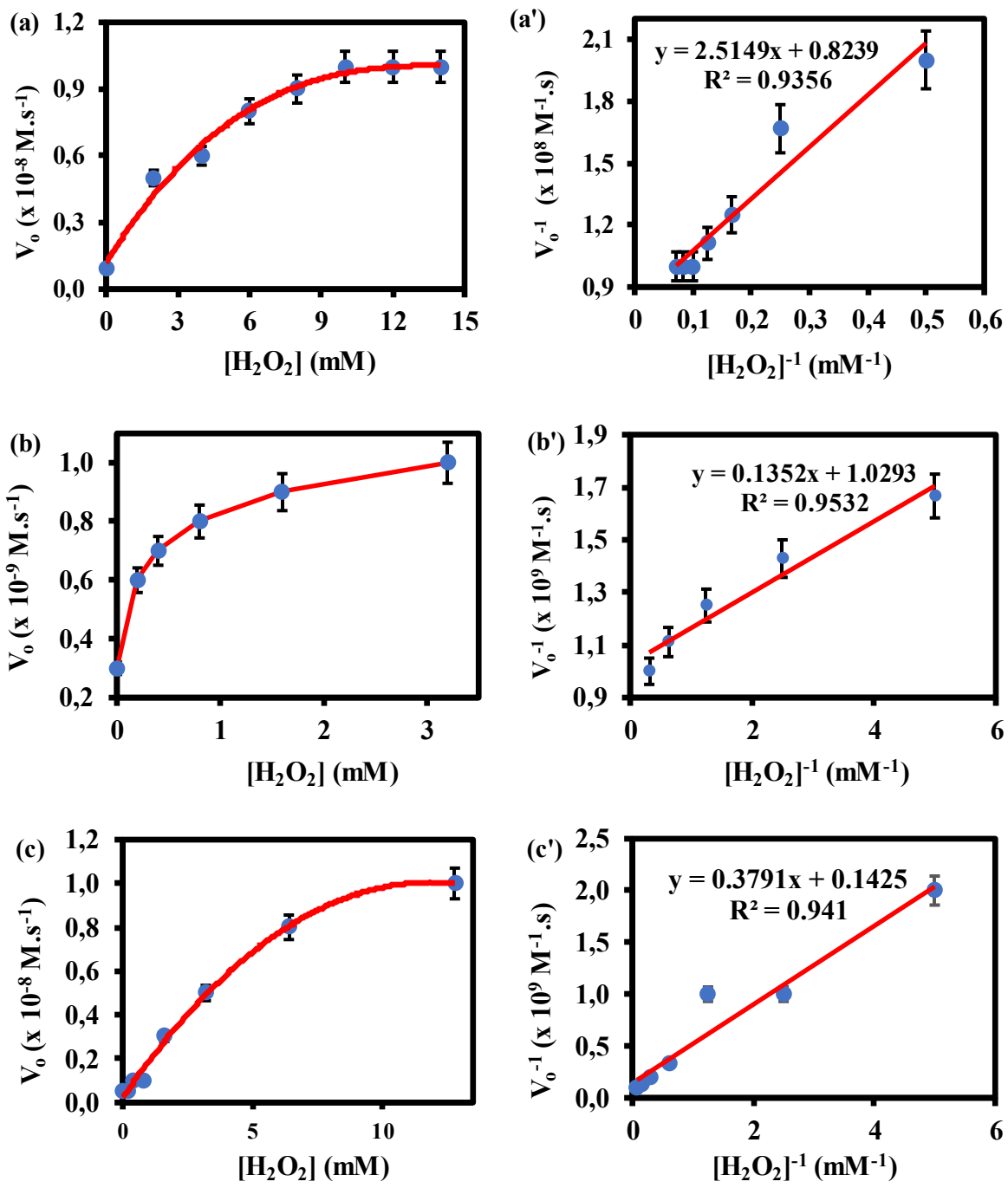

Figure 3.6: The steady-state kinetic plots of varied H_2O_2 concentration at a fixed TMB concentration and their corresponding double reciprocal plots for (a) CuONRs@$Au_{1.0}$NPs, (b) CuONRs@$Pd_{1.0}$NPs and (c) CuONRs@$Au_{0.5}$/$Pd_{0.5}$NPs.

Figure 3.7 shows the steady-state kinetic parameters, plot of initial velocity (V_o) versus substrate concentration [TMB], and their corresponding double reciprocal plots for (a) CuONRs@$Au_{1.0}$NPs (b) CuONRs@$Pd_{1.0}$NPs and (c) CuONRs@$Au_{0.5}/Pd_{0.5}$NPs. The concentration of TMB was varied while keeping the H_2O_2 concentration constant for different nanomaterials. The TMB substrate concentration was varied from 0 – 7.0 mM. At lower TMB concentrations (< 4.0 mM), the initial velocity (V_o) increased linearly with increasing concentration of TMB for CuONRs@$Au_{1.0}$NPs, CuONRs@$Pd_{1.0}$NPs and CuONRs@$Au_{0.5}/Pd_{0.5}$NPs and reaching the plateau at 4.0 – 7.0 mM. The obtained results are representative of the Michaelis-Menten mechanism. The K_m and V_{max} values were calculated and summarised in **Table 3.1** for H_2O_2 and TMB as substrates. The CuONRs@$Pd_{1.0}$NPs showed a strong binding affinity for both H_2O_2 (K_m = 0.13 mM) and TMB (K_m = 2.59 mM) respectively. The CuONRs@$Au_{0.5}/Pd_{0.5}$NPs showed a strong binding affinity with H_2O_2 (K_m = 2.66) and a weak binding affinity with TMB (K_m = 19.70 mM). The CuONRs@$Au_{0.5}/Pd_{0.5}$NPs showed the maximum velocity (V_{max}) with H_2O_2 ($V_{max} = 2.64 \times 10^{-9}$) and TMB ($V_{max} = 1.07 \times 10^{-8}$). The values of CuONRs@$Pd_{1.0}$NPs and CuONRs@$Au_{0.5}/Pd_{0.5}$NPs lies within the reported range for HRP (K_m = 0.214 – 3.72 mM) for H_2O_2 as a substrate. When TMB was used as a substrate the K_m values for CuONRs@$Au_{1.0}$NPs, CuONRs@$Pd_{1.0}$NPs and CuONRs@$Au_{0.5}/Pd_{0.5}$NPs were higher than HRP. The reported values for HRP when TMB was used as a substrate are (K_m = 0.275 – 0.434 mM).[26,18] CuONRs@$Pd_{1.0}$NPs are showing better signal compared to CuONRs@$Au_{1.0}$NPs and CuONRs@$Au_{0.5}/Pd_{0.5}$NPs especially in terms of K_m values.

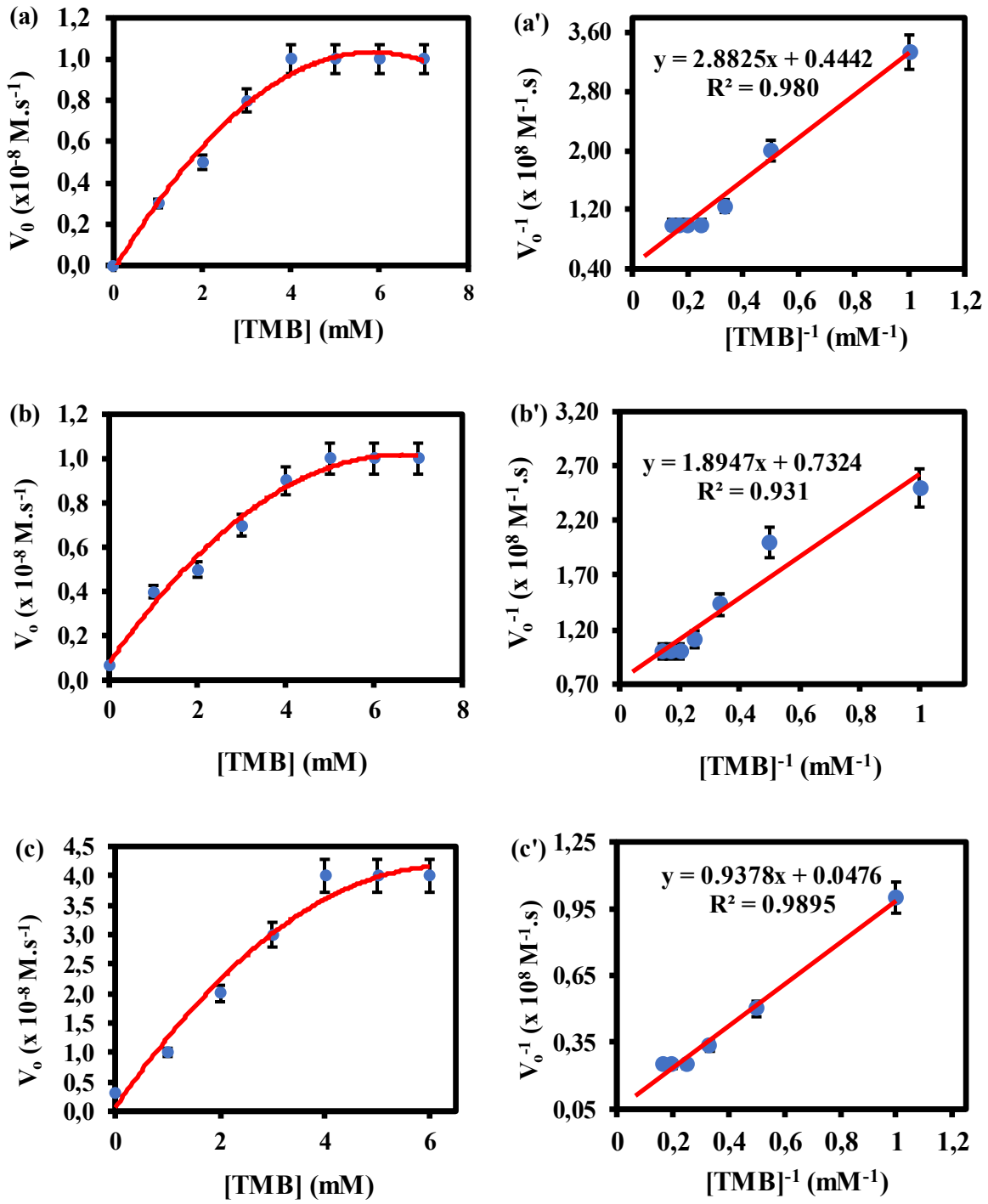

Figure 3.7: The steady-state kinetic plots of varied TMB concentration at a fixed H_2O_2 concentration and their corresponding double reciprocal plots for (a) CuONRs@$Au_{1.0}$NPs, (b) CuONRs@$Pd_{1.0}$NPs, and (c) CuONRs@$Au_{0.5}$/$Pd_{0.5}$NPs.

Table 3.1: The comparison of the steady-state kinetic parameters (K_m and V_{max}) of CuONRs@$Au_{0.5}$/$Pd_{0.5}$NPs with HRP and other nanoparticles.

Catalyst	Substrate	K_m (mM)	V_{max} ($M.s^{-1}$)
CuONRs[TW]	**[H_2O_2]**	**40.04**	**1.06 x 10^{-9}**
	[TMB]	**2.91**	**5.52 x 10^{-9}**
CuONRs@$Au_{1.0}$NPs[TW]	**[H_2O_2]**	**3.05**	**3.98 x 10^{-9}**
	[TMB]	**6.49**	**3.47 x 10^{-9}**
CuONRs@$Pd_{1.0}$NPs[TW]	**[H_2O_2]**	**0.13**	**7.39 x 10^{-9}**
	[TMB]	**2.59**	**5.28 x 10^{-9}**
CuONRs@$Au_{0.5}$/$Pd_{0.5}$NPs[TW]	**[H_2O_2]**	**2.66**	**2.64 x 10^{-9}**
	[TMB]	**19.40**	**1.07 x 10^{-8}**
HRP[18,26]	**[H_2O_2]**	**0.214 – 3.72**	**1.24 x 10^{-8} - 8.71 x 10^{-8}**
	[TMB]	**0.275 – 0.434**	**2.46 x 10^{-8} - 10.0 x 10^{-8}**
CuO-Au nanoalloy[27]	**[H_2O_2]**	**4.08**	**1.11 x 10^{-10}**
	[TMB]	**3.54**	**1.05 x 10^{-10}**
Fe_3O_4@SiO_2-NH_2-Au-$Pd_{0.30}$ NPs[28]	**[H_2O_2]**	**0.35**	**6.78 x 10^{-8}**
	[TMB]	**0.09**	**8.65 x 10^{-8}**

TW – This work

3.7.5 The quenching of reactive oxygen species using DBPF

The peroxidase-like activity of CuONRs@$Au_{1.0}$NPs, CuONRs@$Pd_{1.0}$NPs and CuONRs@$Au_{0.5}/Pd_{0.5}$NPs are due to the reduction of H_2O_2 to produce reactive oxygen species (ROS). The produced reactive oxygen species oxidize the chromogenic substrate (TMB) to form the oxidized product (TMBDI). The generation of reactive oxygen species (ROS) was evaluated using 1,3-diphenylisobenzofuran (DPBF) as a radical scavenger. DPBF is a fluorescent dye that reacts in a specific manner with H_2O_2 and reactive oxygen species that are generated upon catalytic reduction of H_2O_2.[29] The CuO nanorods decorated with gold and palladium nanoparticles produced radicals (OH·, HOO·, $\cdot O_2$) upon interacting with H_2O_2. The produced radicals are scavenged by DPBF and a decrease in its absorption confirms the production of radicals. The degradation of DPBF was monitored using UV-vis spectroscopy. The rate of degradation of DPBF was monitored with time at 1 – 2 minutes intervals for different nanoparticles. **Figure 3.8** shows the rate of degradation plots for DPBF + H_2O_2 (green), DPBF + NPs (red) and DPBF + H_2O_2 + NPs (purple) for (a) CuONRs@$Au_{1.0}$NPs, (b) CuONRs@$Pd_{1.0}$NPs and (c) CuONRs@$Au_{0.5}/Pd_{0.5}$NPs. There was no change in the absorption intensity for DPBF + H_2O_2. A slight decrease in DPBF absorption was observed in the presence of CuONRs decorated with gold and palladium nanoparticles. When the nanoparticles were incubated with H_2O_2 + DPBF, a fast decrease in DPBF absorption band at 430 nm was observed. The rate of degradation of DPBF was obtained from a slope of the linear plot of absorbance (a.u) vs time. The rates of degradation of DPBF for CuONRs, CuONRs@$Au_{1.0}$NPs, CuONRs@$Pd_{1.0}$NPs and CuONRs@$Au_{0.5}/Pd_{0.5}$NPs are summarized in **Table 3.2**. The DPBF in the presence of H_2O_2 showed the slowest rate of degradation (5.0×10^{-4} a.u./min). The rate of degradation of DPBF was faster in the presence H_2O_2 and CuO nanorods decorated with gold and palladium nanoparticles. The CuONRs@$Au_{0.5}/Pd_{0.5}$NPs showed the highest rate of degradation of DPBF (2.3×10^{-2} a.u./min). The CuONRs@$Au_{0.5}/Pd_{0.5}$NPs produce more

radical oxygen species (ROS) at a higher rate than CuONRs@$Au_{1.0}$NPs and CuONRs@$Pd_{1.0}$NPs.

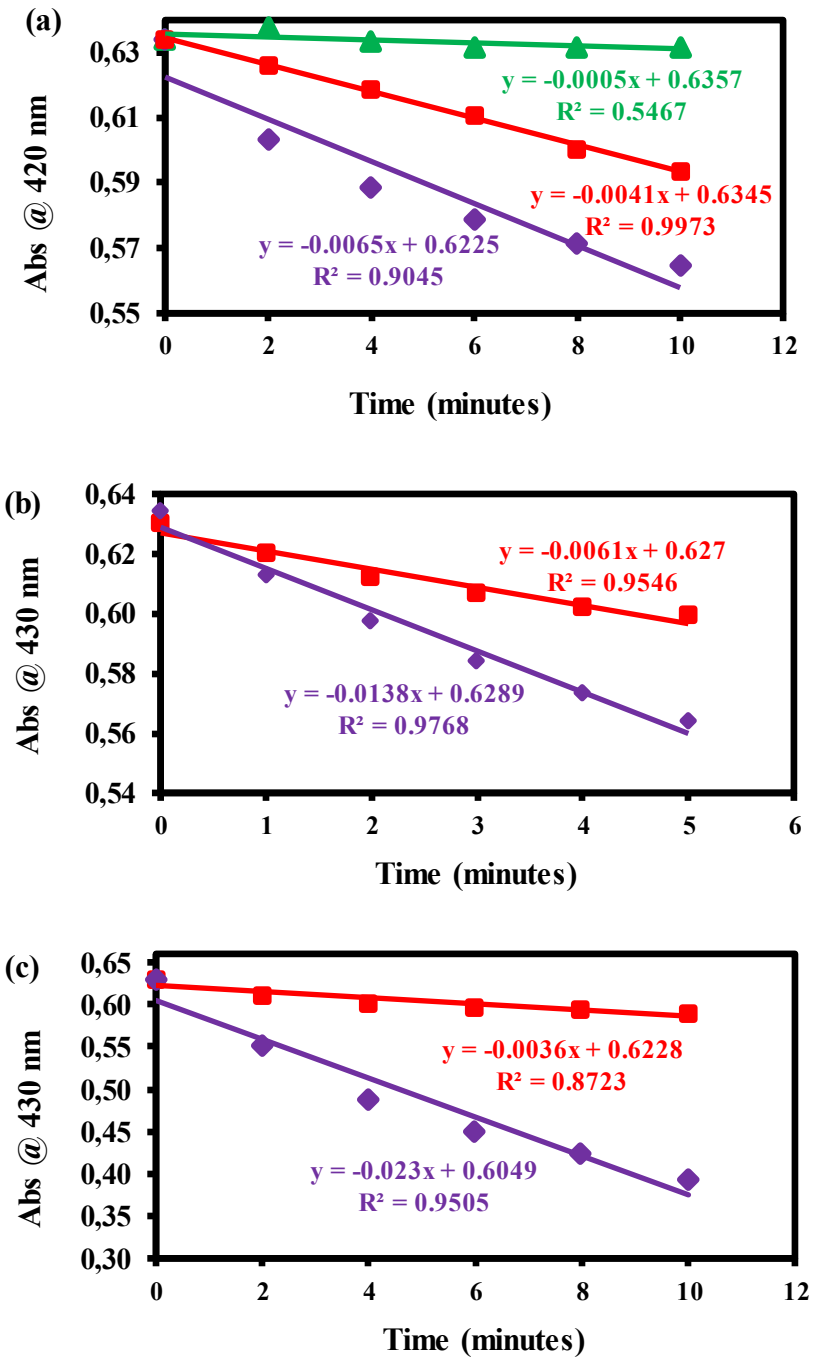

Figure 3.8: The rate of degradation plots for, DPBF + H_2O_2 alone (green), DPBF + NPs alone (red), and DPBF + H_2O_2 + NPs (purple) for (a) CuONRs@$Au_{1.0}$NPs, (b) CuONRs@$Pd_{1.0}$NPs, and (c) CuONRs@$Au_{0.5}$/$Pd_{0.5}$NPs.

Table 3.2: Comparison of the rate of degradation of DPBF for the prepared CuONRs@$Au_{0.5}$/$Pd_{0.5}$ NPs.

Nanomaterials	Rate of degradation (min^{-1})		
	DPBF + H_2O_2	DPBF + NRs	DPBF + H_2O_2 + NRs
CuONRs	**5.0 x 10^{-4}**	**8.70 x 10^{-3}**	**5.99 x 10^{-2}**
CuONRs@$Au_{1.0}$NPs		**4.10 x 10^{-3}**	**6.50 x 10^{-3}**
CuONRs@$Pd_{1.0}$NPs		**6.10 x 10^{-3}**	**1.38 x 10^{-2}**
CuONRs@$Au_{0.5}$/$Pd_{0.5}$ NPs		**3.60 x 10^{-3}**	**2.30 x 10^{-2}**

The rate of H_2O_2 production is equivalent to the rate of degradation of DPBF and it was found to decrease following the trend : 2.30 x 10^{-2} > 1.38 x 10^{-2} > 6.50 x 10^{-3} for CuONRs@$Au_{0.5}$/$Pd_{0.5}$NPs > CuONRs@$Pd_{1.0}$NPs > CuONRs@$Au_{1.0}$NPs.

3.7.6 Glucose detection using CuONRs decorated with gold and palladium (bi)metallic nanoparticles

The prepared nanomaterials were applied in the colorimetric detection of glucose as their peroxidase-like activity is dependent on the interaction with H_2O_2. H_2O_2 is by-product of various enzymes with enzyme co-factor that can be reduced. The example of such enzymes are cholesterol esterase for the conversion of cholesterol and glucose oxidase (GOx)[30] for the conversion of glucose. Glucose oxidase is used in the fabrication of biosensors for the detection of glucose enzymes as biocatalysts offer excellent selectivity and sensitivity towards their substrate. For GO_x, H_2O_2 is produced as a by-product from the catalytic oxidation of D-glucose by glucose oxidase to yield gluconic acid. The produced H_2O_2 generates reactive oxygen species (ROS). In the presence of TMB as a chromogenic substrate, the generated reactive oxygen species interact with the nanoparticles to induce the catalytic oxidation of TMB to form a blue a coloured oxidized product (TMBDI). The TMBDI is characterized by the absorption band at 652 nm in the UV-vis spectrum. The detection of glucose was performed using UV-vis spectroscopy, by investigating the peroxidase-like activity of the prepared nanomaterials. The detailed method for the detection of glucose using CuONRs decorated with gold and palladium nanoparticles is outlined in the experimental section. **Figure 3.9** shows the UV-vis spectra and the corresponding plots of monitored absorbance at 652 nm versus varied D-glucose concentration for (a) CuONRs@$Au_{1.0}$NPs, (b) CuONRs@$Pd_{1.0}$NPs, and (c) CuONRs@$Au_{0.5}$/$Pd_{0.5}$ NPs. The concentration of D-glucose was varied from 0 – 60 µM while the concentration of GO_x, nanoparticles, TMB and reaction time were kept constant. When the concentration of D-glucose was raised from 10 – 40 µM, the absorbance at 652 nm increased linearly for CuONRs@$Au_{1.0}$NPs. The CuONRs@$Pd_{1.0}$NPs and CuONRs@$Au_{0.5}$/$Pd_{0.5}$NPs showed a linear increase in absorbance at 652 nm throughout the studied concentration range (0 – 60 µM) of D-glucose. The intensity of the absorption band at 652 nm is proportional to

the concentration of D-glucose. Therefore, the amount/concentration of the produced H_2O_2 is directly proportional to the concentration of D-glucose. The results indicate that the presence GOx in solution induced the catalytic oxidation of D-glucose to form gluconolactone. The enzyme was reduced to form $GO_x(FADH_2)$. Upon oxidation the $GO_x(FADH_2)$ was reduced to form $GO_x(FAD)$ and H_2O_2 was produced. The produced H_2O_2 interacts with the nanoparticles to catalytically oxidize TMB to TMBDI. The linear regression equations for CuONRs@$Au_{1.0}$NPs: Abs = 0.0037 [D-glucose] + 0.0716, R^2 = 0.99, for CuONRs@$Pd_{1.0}$NPs : Abs = 0.0024 [D-glucose] + 0.1035, R^2 = 0.97 and for CuONRs@$Au_{0.5}$/$Pd_{0.5}$NPs: Abs = 0.0030 [D-glucose] + 0.1124, R^2 = 0.99. CuONRs@$Pd_{1.0}$NPs and CuONRs@$Au_{0.5}$/$Pd_{0.5}$NPs showed excellent analytical parameters. This could be attributed to the electronegativity differences between gold and palladium. The limit of detection (LOD) and the limit of quantification (LOQ) for CuONRs@$Au_{1.0}$NPs were 7.19 µM and 21.78 µM, for CuONRs@$Pd_{1.0}$NPs : 19.65 µM and 59.54 µM, and for CuONRs@$Au_{0.5}$/$Pd_{0.5}$NPs: 10.46 µM and 31.71 µM, respectively.

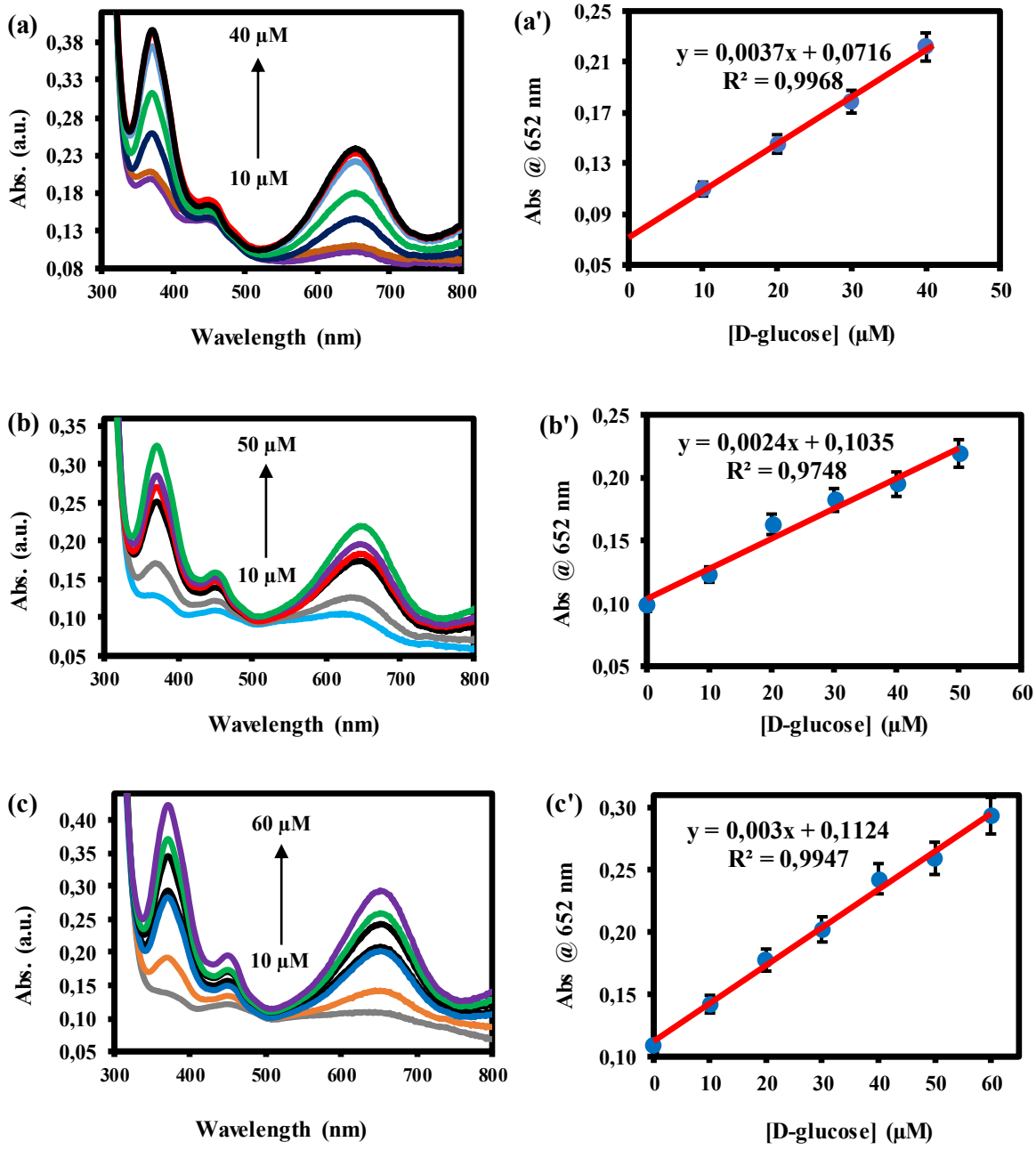

Figure 3.9: UV-vis spectra and the corresponding plots of absorbance @ 652 nm versus [D-glucose] concentration for (a) CuONRs@$Au_{1.0}$NPs, (b) CuONRs@$Pd_{1.0}$NPs, and (c) CuONRs@$Au_{0.5}/Pd_{0.5}$NPs.

3.8 Conclusion

The preparation of CuO nanorods decorated with gold and palladium nanoparticles was successfully accomplished and the decoration with gold and palladium was confirmed by TEM and EDS. The prepared nanomaterials were investigated their potential as Horseradish-peroxidase mimics. The nanomaterial peroxidase-like activity was affected by different reaction conditions such as pH, reaction time, temperature and varied substrate concentration. The investigation of the steady-state kinetic parameters showed that the prepared nanomaterials followed Michaelis-Menten kinetics behaviour. The CuONRs@$Au_{1.0}$NPs showed the K_m = 3.05 mM and 6.49 mM for H_2O_2 and TMB respectively. The CuONRs@$Pd_{1.0}$NPs showed the K_m = 0.13 mM and 2.59 mM for H_2O_2 and TMB respectively. The CuONRs@$Au_{0.5}$/$Pd_{0.5}$NPs showed the K_m = 2.66 mM and 19.70 mM for H_2O_2 and TMB respectively. The CuONRs@$Pd_{1.0}$NPs showed the highest binding affinity when H_2O_2 was used as a substrate. The CuONRs@$Pd_{1.0}$NPs also showed the highest binding affinity when TMB was used as substrate while CuONRs@$Au_{0.5}$/$Pd_{0.5}$NPs showed the weakest binding affinity. The K_m values showed that CuONRs@$Au_{0.5}$/$Pd_{0.5}$NPs had a higher affinity for H_2O_2. The maximum velocity (V_{max}) for CuONRs@$Au_{0.5}$/$Pd_{0.5}$NPs were found to be 2.64 x 10^{-9} and 1.07 x 10^{-8} ($M.s^{-1}$) for H_2O_2 and TMB respectively.

The production of ROS was determined and detected using DPBF as a radical scavenger. The nanomaterials interact with hydrogen peroxide to produce reactive oxygen species (ROS). The consumption of the produced ROS was confirmed by the decrease in the DPBF absorption band at 430 nm using UV-vis spectroscopy. The CuONRs@$Au_{0.5}$/$Pd_{0.5}$ NPs showed the highest rate of degradation of DPBF (2.3 x 10^{-2} a.u./min).

The prepared nanomaterials were further applied in the colorimetric detection of glucose. The CuONRs@$Au_{0.5}$/$Pd_{0.5}$NPs showed good linearity in the studied concentration range (0 – 60 μM) with the linear regression equation: Abs = 0.0030 [glucose] + 0.1124, R^2 = 0.99. The limit of detection (LOD) and the limit of quantification (LOQ) for CuONRs@$Au_{1.0}$NPs were estimated to be 7.19 μM and 21.78 μM, for CuONRs@$Pd_{1.0}$NPs : 19.65 μM and 59.54 μM, and for CuONRs@$Au_{0.5}$/$Pd_{0.5}$NPs: 10.46 μM and 31.71 μM, respectively.

References

1. M.B. Gawande, A. Goswami, T. Asefa, H. Guo, A.V. Biradar, D.L. Peng, R. Zboril, R.S. Varma, Chem. Soc. Rev., 2015 (44) 7540 - 7590.
2. S.Y. Tee, E. Ye, P.H. Pan, C.J.J. Lee, H.K. Hui, S.Y. Zhang, L. D. Koh, Z. Dong, M.Y. Han, Nanoscale, 2015 (7) 11190 - 11198.
3. W. Yao, F.L. Li, H.X. Li, J.P. Lang, J. Mater. Chem. A, 2015 (3) 4578 - 4585.
4. Y.G. Sun, Y.N. Xia, J. Am. Chem. Soc., 2004 (126) 3892 - 3901.
5. C.M. Cobbley, D.J. Campbell, Y.N. Xia, Adv. Mater, 2008 (20) 748 - 752.
6. X. Liu, J. Locozzia, Y. Wang, X. Cui, Y. Chen, S. Zhao, Z. Li, Z. Lin, Energy Environ. Sci., 2017 (10) 402 - 434
7. K.C. Leung, S. Xuan, X. Zhu, D. Wang, C.P. Chak, S.F. Lee, W.K. Ho, B.C. Chung, Chem. Soc. Rev., 2012 (41) 1911 - 1928.
8. N.E. Motl, A.F. Smith, C.J. DeSantis, S.E. Skrabalak, Chem. Soc. Rev., 2014 (43) 3823 - 3834.
9. J. Liu, W. Wang, T. Shen, Z. Zhao, H. Feng, F. Cui, RSC Adv., 2014 (4) 30624 - 30629.
10. W. He, H. Kim, W.G. Wamer, D. Melka, J.H. Callahan, J.J. Yin, J. Am. Chem. Soc., 2013 (136) 750 - 757.

11. C. Xu, J. Xie, D. Ho, C. Wang, N. Kohler, E.G. Walsh, J.R. Morgan, Y.E. Chin, S. Sun, Angew. Chem., Int. Ed., 2008 (47) 173 - 176.

12. S. Wang, Z. Wang, Z, Zha, Dalton Trans., 2009, 9363 - 9373.

13. M.S Chavalli, M.P. Nikolova, SN Applied Sciences, 2019 (1) 607 (1 - 30).

14. L. Long, J. Liu, K. Lu, T. Zhang, Y. Xie, Y. Ji, X. Wu, J Nanobiotechnol, 2018 (16) 46 (1 - 10).

15. L. Gao, X. Yan, Sci China Life Sci, 2016 (59) 400 - 402.

16. Y.C. Yang, Y.T. Wang, W.L. Tseng, ACS Appl. Mater. Interfaces, 2017 (9) 10069 - 10077.

17. X. Wang, Q. Han, S. Cai, T. Wang, C. Qi, R. Yang, C. Wang, Analyst, 2017 (142) 2500 - 2506.

18. L. Gao, J. Zhuang, L. Nie, J. Zhang, Y. Zhang, N. Gu, T. Wang, J. Feng, D. Yang, S. Perrett, X. Yang, nature nanotechnology, 2007 (2) 577 - 583.

19. R. Andre, F. Natalio, M. Humanes, J. Leppin, K. Heinze, R. Wever, H.C. Schroder, W.E.G. Muller, W. Tremel, Adv. Funct. Mater., 2011 (2) 1501 - 1509.

20. G.W. Wu, S.B. He, H.P. Peng, H.H Deng, A.L. Liu, X.H. Lin, X.H. Xia, W. Chen, Anal Chem, 2014 (86) 10955 - 10960.

21. W. Chen, J. Chen, Y.B. Feng, L. Hong, Q. Chen, L. Wu, X. Lin, X. Xia, Analyst, 2012 (137) 1706 - 1712.

22. M. Marelli, A. Jouve, A. Villa, R. Psaro, A. Barlena, L. Prati, C. Evangelisti, J. Phys. Chem, 2009 (123) 2864 - 2871.

23. J.M. Berg, A. Romoser, N. Benerjee, R. Zedba, C.M. Sayes, Nanotoxicology, 2009 (3) 276 - 283.

24. D. Zhou, K. Zeng, M. Yang, Microchim Acta, 2019 (186) 1 - 7.

25. M.C. Kim, D. Lee, S.H. Jeong, S.Y. Lee, E. Kang, ACS Appl Mater Interfaces, 2016 (8) 34317 - 34326.

26. Y. Song, K. Qu, C. Zhao, J. Ren, X. Qu, Adv. Mater, 2010 (22) 2206 - 2210.

27. S. Mvango, P. Mashazi, Mater Sci. Eng C, 2019 (96) 814 - 823.

28. O. Adeniyi, S. Sicwetsha, P. Mashazi, ACS Appl. Mater. Inter, 2020 (12) 1973 - 1987.

29. K. Zamojc, M. Zdrowowicz, P.B.R Velasquez, K. Krzyminski, B. Zaborowski, P. Niedzialkowski, D. Jacewicz, L. Chmurzynski, Free Radic. Res., 2017 (51) 38 - 46.

30. T. Li, K. Zhu, S. He, X. Xia, S. Liu, Z. Wang, X. Jiang, Analyst, 2011 (136) 2893 - 2896.

CHAPTER 4

GENERAL CONCLUSIONS

General Conclusions

The preparation of spherical CuONPs, CuONRs, CuONRs@$Au_{1.0}$NPs, CuONRs@$Pd_{1.0}$NPs and CuONRs@$Au_{0.5}/Pd_{0.5}$NPs were successfully achieved. Their characterization using UV-vis spectroscopy, DLS (zeta potential), XRD, TEM and EDS confirmed their successful preparation. The decoration of gold and palladium nanoparticles on the surface of CuONRs was confirmed by TEM and EDS. The average particle size for spherical CuONPs was 8.0 ± 2.0 nm. The TEM image of CuONRs showed the length of 40. ± 5.6 nm and the width of 11. ± 4.5 nm. The average particle size of Au nanoparticles on the surface of CuONRs was 2.9 ± 1.2 nm. The average particle size of palladium nanoparticles on the surface of CuONRs was 2.8 ±1.5 nm. The average particle size of Au and Pd bimetallic nanoparticles on the surface of CuONRs was 2.4 ± 1.6 nm.

The prepared spherical CuONPs, CuONRs, CuONRs@$Au_{1.0}$NPs, CuONRs@$Pd_{1.0}$NPs and CuONRs@$Au_{0.5}/Pd_{0.5}$NPs were investigated their potential as Horseradish-peroxidase mimics. To investigate the peroxidase-like activity of the nanomaterials, the catalytic oxidation of a chromogenic substrate 3,3',5,5'-tetramethylbenzidine (TMB) in the presence of H_2O_2 was investigated. The nanomaterials were found to possess the intrinsic peroxidase-like activity which is identical to Horseradish-peroxidase (HRP). The presence of the peroxidase-like activity was confirmed by the emergence of a blue coloured species (TMBDI) with the maximum absorption band at 652 nm. The peroxidase-like activity was affected by different reaction conditions such as pH, reaction time, temperature, and varied substrate concentration.

The investigation of the steady-state kinetic parameters showed that the peroxidase-like activity of the prepared nanomaterials followed the Michaelis-Menten kinetics behaviour. The spherical CuONPs showed the K_m = 1.12 mM and 1.14 mM for H_2O_2 and TMB respectively. The CuONRs showed the K_m = 40.04 mM and 2.91 mM for H_2O_2 and TMB respectively. The

CuONRs@$Au_{1.0}$NPs showed the K_m = 3.05 mM and 6.49 mM for H_2O_2 and TMB respectively. The CuONRs@$Pd_{1.0}$NPs showed the K_m = 0.13 mM and 2.59 mM for H_2O_2 and TMB respectively. The CuONRs@$Au_{0.5}$/$Pd_{0.5}$NPs showed the K_m = 2.66 mM and K_m = 19.70 mM for H_2O_2 and TMB respectively.

The production of ROS was determined and detected using DPBF as a radical scavenger. UV-vis spectroscopy was used to monitor the reaction and the DPBF absorption band at 430 nm was monitored. The rate of degradation of DPBF for spherical CuONPs was 4.91 x 10^{-2} a.u./min, for CuONRs was 5.99 x 10^{-2} a.u./min, for CuONRs@$Au_{1.0}$NPs was 6.50 x 10^{-3} a.u./min, for CuONRs@$Pd_{1.0}$NPs was 1.38 x 10^{-2} a.u./min and for CuONRs@$Au_{0.5}$/$Pd_{0.5}$NPs was 2.30 x 10^{-2} a.u./min.

The prepared nanomaterials were applied in the colorimetric detection of glucose as their peroxidase-like activity is dependent on the interaction with H_2O_2. The glucose detection was investigated using TMB as a chromogenic substrate. The glucose detection was studied using UV-vis spectroscopy, by investigating the peroxidase-like activity of spherical CuONPs, CuONRs, CuONRs@$Au_{1.0}$NPs, CuONRs@$Pd_{1.0}$NPs and CuONRs@$Au_{0.5}$/$Pd_{0.5}$NPs. The LOD and LOQ for spherical CuONPs was 0.73 µM and 2.42 µM, for CuONRs was 0.13 µM and 0.42 µM, CuONRs@$Au_{1.0}$NPs was 7.19 µM and 21.78 µM, for CuONRs@$Pd_{1.0}$ NPs was 19.65 µM and 59.54 µM, and for CuONRs@$Au_{0.5}$/$Pd_{0.5}$NPs was 10.46 µM and 31.71 µM.

Recommendations and future work

The production of reactive oxygen species (ROS) is the key step in the colorimetric detection of glucose. Thus, the production of reactive oxygen radical species (ROS) can also be quantified using electron paramagnetic resonance (EPR) spectroscopy. The nanomaterials studied in this work can be further used for immobilization of biological molecules. Gold nanoparticles decorated on the surface of CuONRs would be effective for the immobilization of biological molecules because gold nanoparticles provide a stable surface and biological molecules retain their activity after immobilization. The ELISA IgG detection using the nanomaterial bioconjugate can be achieved.